Design, Fabrication and Control of the Micromechanical Flying Insect

by

Srinath Avadhanula

B.Tech. (Indian Institute of Technology, Bombay) 1999
M.S. (University of California, Berkeley) 2002

A dissertation submitted in partial satisfaction of the
requirements for the degree of
Doctor of Philosophy

in

Mechanical Engineering

in the

GRADUATE DIVISION
of the
UNIVERSITY OF CALIFORNIA, BERKELEY

Committee in charge:
Professor Ronald S. Fearing, Chair
Professor Andrew Packard
Professor Roberto Horowitz
Professor Claire Tomlin

Spring 2006

The dissertation of Srinath Avadhanula is approved:

Co-Chair Date

Co-Chair Date

Date

Date

University of California, Berkeley

Spring 2006

Design, Fabrication and Control of the Micromechanical Flying Insect

Abstract

Design, Fabrication and Control of the Micromechanical Flying Insect

by

Srinath Avadhanula
Doctor of Philosophy in Mechanical Engineering

University of California, Berkeley

Professor Ronald S. Fearing, Co-Chair

Professor Andrew Packard, Co-Chair

The Micromechanical Flying Insect (MFI) project aims at achieving some of the extraordinary flight performance of insects by creating a centimeter-sized flying robot capable of sustained autonomous flight. The core mechanical component used in the MFI is analogous to the insect thorax. It consists of a series of transmission elements for converting piezoelectric actuator motion into complex wing flapping and rotation capable of reproducing some aspects of insect wing motion. This work explores in detail the design, fabrication and control of the thorax. In particular, we show that by carefully "tuning" the design of the MFI thorax, while accounting for the aerodynamics, it is possible to utilize a simple control strategy while still generating flight forces on a test stand, sufficient for take-off.

Professor Ronald S. Fearing
Dissertation Committee Co-Chair

Professor Andrew Packard
Dissertation Committee Co-Chair

To my family,

Contents

List of Figures

List of Tables

Acknowledgments

I want to thank a whole lot of people who are as yet undecided.

Chapter 1

Introduction

Insect flight has long been an endless source of fascination (and a little mystery). The spectacle of a wasp hovering steadily in mid-air and then moving an arm's length *sideways* in the blink of an eye is sufficient to inspire awe, curiosity and a desire to explain and duplicate, in any scientist or engineer. The applications of a robot which can duplicate (even in part) the exceptional flight performance of insects are immense.

From the perspective of an army general, an insect-like robot would provide an unparalleled way of gathering intelligence. The small size and extreme maneuverability of such a robot would enable it to remain almost invisible while being able to penetrate highly inaccessible places. See [Yan 02] for an exploration of other factors which make an insect-like robot invaluable in an intelligence gathering scenario. A small insect-like robot would also be invaluable in a search and rescue scenario because flight would enable a robot to bypass the highly unstructured environment which would make larger (or ground based) robots useless. Finally, small, highly mobile robots provide a good means of sensor dispersal of small sensor nodes enabling distributed sensing.

The Micromechanical Flying Insect (MFI) project at the University of California, Berkeley aims at creating just such a robot. The project was started in Berkeley in May 1998, with the aim as stated on the project website[1]: “to develop a 25 mm (wingtip-to-wingtip) device capable of sustained autonomous flight”.

The MFI project uses a biomimetic approach in trying to build an insect-like robot. This implies taking inspiration from similar natural systems and methods found in nature. At the scale of the MFI, we need to look no further than the abundance of insects all around us. There is obviously a vast variety of insects which we can take inspiration from. For the size scale of the MFI, we chose to base our design on the blowfly (*Calliphora erythrocephala*), which has a wing span of about 25mm and a weight of around 100mg.

Flying insects, although small and almost omnipresent, are extremely complex machines. To quote Dudley [Dudley 00], “Flight is energetically very costly, and the metabolism of winged insects represents an extreme of physiological design among all animals”. Next, although some aspects of the insect morphology have been increasingly well-studied, for example, the insect musculature [Dudley 00], the cuticular structure of the insect thorax [Chen 02], and the wing morphology [Ellington 84d], to the best of this author’s knowledge, the precise mechanical micro-structure of the insect kinematics is still not precisely known.

The MFI project, therefore, utilizes a *functional* biomimetic approach towards the design of the robot. We do not try to precisely imitate the morphology of the insect musculature, but instead try to imitate it at an aerodynamic level. As the following

---

[1] http://robotics.eecs.berkeley.edu/˜ronf/MFI/

section will elaborate, the MFI project started when biologists empirically studied the intricacies of insect aerodynamics and derived a minimal set of requirements which were deemed necessary for successful hovering flight. It is at this level that we can be said to "imitate" insects.

1.1 Aerodynamic Theory

The first step in explaining insect flight is to record the actual kinematics of insect flapping. This has been done successfully for various insects [Ellington 84b, Dickinson 99, Altshuler 05]. However, recording the instantaneous flight forces in real time was never quite as successful because of their small size and high frequencies [Birch 03]. There have been attempts at measuring the total body forces in insects [Clopeau 79, Dickinson 96], however these are hard to interpret because the inertial forces produced by the body significantly contaminate the much smaller aerodynamic forces.

Predicting the correct aerodynamic forces corresponding to a given kinematics of the wing is a much harder problem and still remains an active area of research. The primary difficulty arises because steady state aerodynamics fails spectacularly in predicting the lift forces which insects generate. As described in [Altshuler 05], in 1934, August Magnan and André Sainte-Lague concluded from a simple aerodynamic analysis [Magnan 34] that bee flight was "impossible". Although the assumptions in this paper were later shown to be false, it is true that steady state aerodynamic theory cannot predict sufficient lift forces to fully explain insect flight. The failure of steady state aerodynamic theory arises because of the extremely high flapping and rotations present in insect flight. As described in [Ellington 84c], "the large amplitude flapping and rotation in the absence of a mean flight velocity makes even the most severe examples of the catastrophic flutter of man-made wings seem like gentle calisthenics".

In 1984, [Ellington 84c], Ellington proposed a set of unsteady aerodynamic mechanisms, which could better explain insect flight forces. The primary mechanism which was proposed was termed "delayed stall". In the case of a traditional airfoil theory, when the angle of attack is increased beyond a small angle, termed the critical angle of attack, the leading edge vortex sheds and the lift generated by the airfoil falls dramatically. This well known phenomenon is termed *stall*. However, Ellington noticed that when an insect wing is rotated rapidly through an angle, the vortex is formed very gradually and is not shed for a majority of the stroke. It is theorized that a span wise flow along the insect wing stabilizes the leading edge vortex (LEV) [Ellington 96, Birch 01, Birch 04]. The LEV generates an area of low pressure over the insect wing and significantly adds to the lift generated by the insect wing.

For a while, delayed stall was considered sufficient to explain the forces which insects experienced during flight. However, Dickinson later showed [Dickinson 99] that although delayed stall is sufficient to explain some of the aspects of insect flight, it was not sufficient by itself to explain the maneuverability and the ability of some insects to lift twice their body weight while flying. Using a dynamically scaled model of a fruit fly wing (called Robofly), he empirically observed two important unsteady state effects which were previously not considered.

The first, termed as *rotational lift*, is additional lift caused by the rotation of the wing. This is akin to the lift generated by a spinning tennis ball while in flight (the *Magnus* effect), although it is subtly different as will be explained in Section 3.2. The next unsteady state mechanism observed is termed *wake capture*. This arises from an interaction of the wake generated by the insect and the motion of the wing itself. After the wing rotates at the end of each stroke, it hits the wake it has generated in the previous half-stroke leading to dramatic increases in the observed aerodynamic forces. The unsteady aerodynamic mechanisms will be described in much better detail in later sections.

Since we will be using the model derived in [Dickinson 99] extensively in a later part of this work, it is pertinent to expand briefly on the experimental setup and scaling methods employed in Robofly. Robofly is based on the theory of *similitude*. A central theorem in this area is the Buckingham-Pi theorem [Buckingham 14], which states that in a system whose behavior depends on N physical parameters, all of which can be expressed in terms of K fundamental units, the system can equally well be described in terms of $N - K$ dimensionless numbers. In case of an insect wing flapping in a fluid, we can see that the important physical parameters are L, the "size" of the wing (this can be any characteristic dimension), ρ, the density of the fluid, ν, the viscosity of the fluid and V, the velocity of the wing. An application of the Buckingham-Pi theorem readily yields the familiar Reynolds number as the relevant dimensionless parameter. This parameter is defined as:

$$Re = \frac{\rho V L}{\nu} \tag{1.1}$$

It can be thought to represent the ratio of the inertial forces (due to the fluid motion) acting on the wing to the viscous forces (due to fluid shearing). The theory of *similitude* says that as long as there is kinematic similitude (i.e., the geometry is similar) and dynamic similitude (i.e., the relevant dimensionless parameters are the same) between two systems, then the basic behavior of the systems is identical up to a scaling factor. In the case of a flapping wing, this means that the flow around two wings will be the similar if the Reynolds numbers corresponding to the two wings are the same. As described in [Fry 05], the scaling between the forces measured on Robofly and the actual forces on the insect wing is given by:

$$F_{\text{Fly}} = F_{\text{Robot}} \times \frac{\rho_{\text{Air}}}{\rho_{\text{Oil}}} \times \left(\frac{n_{\text{Fly}}}{n_{\text{Robot}}}\right)^2 \times \left(\frac{R_{\text{Fly}}}{R_{\text{Robot}}}\right)^2 \times \frac{S_{\text{Fly}}}{S_{\text{Robot}}} \times \frac{\hat{r}_2^2(S)_{\text{Fly}}}{\hat{r}_2^2(S)_{\text{Robot}}}, \tag{1.2}$$

where ρ is the fluid density, n is the frequency of flapping, R is the wing length, S is the wing area and $\hat{r}_2(S)$ is the normalized second moment of area as defined in [Ellington 84a].

In the case of Robofly, the Reynolds number was matched to that of a fruit-fly, which is around 160. For a typical MFI wing, we have $L = 6.5$mm (this corresponds to a 10mm wing with an equivalent radius of 0.65 times the wing span as in [Wang 04]), $V = 8$ m/s and $\rho = 1$ kg/m^3 and $\nu = 1.56 \times 10^{-5}$ Pa-s. This gives a Reynolds number of around 1600, which alerts us to the fact that the scaling law does not quite hold between Robofly and MFI. Another possible source of discrepancy is due to the fact that Robofly, being modeled after the fruitfly, has distinctly different wing trajectories than those utilized on the latest MFI structures. For example, the fruitfly (hence Robofly) exhibits large flapping angles (up to 160°) at relatively low frequencies (150Hz). On the other hand, the latest MFI structures have quite low flapping amplitudes ($< 90°$) at very high frequencies (between 275Hz and 325Hz). This implies that the kinematic similitude between the MFI and Robofly is also lacking. Recent research on honey-bee flight which more closely approximates the MFI [Altshuler 05] has shown that indeed the aerodynamic mechanisms change significantly between fruitflies and honeybees.

Apart from getting an understanding of the underlying aerodynamic mechanisms for lift generation, Robofly was also used to guide the design of the kinematics of the MFI. It was shown in [Dickinson 99] that although insect wing trajectories have 3 degrees of freedom: flapping, rotation and deviation from the stroke plane, the first two are most important for successful lift generation. Subsequently, the MFI kinematics is designed to convert two independent actuator motions into a wing flapping and rotation, such that the flapping and rotation can be independently controlled.

1.2 An Overview of the MFI

The MFI can be divided into a number of distinct functional components. Fig. 1.1 shows an artist's rendering of a futuristic MFI showing these various components as they would look completely assembled:

Battery and Power Electronics : The lightest state of the art, commercially available off the shelf (COTS) batteries are currently still too heavy to be used as is, on the MFI. The power density of the 0.81g Kokam battery[2] is around 450 W/kg. An insect-like flying robot will need at least around 30W/kg power density delivered to the environment. Assuming an overall efficiency of around 10%, we can see that the afore-mentioned battery is adequate from the power

---

[2] available from http://roomflight.com

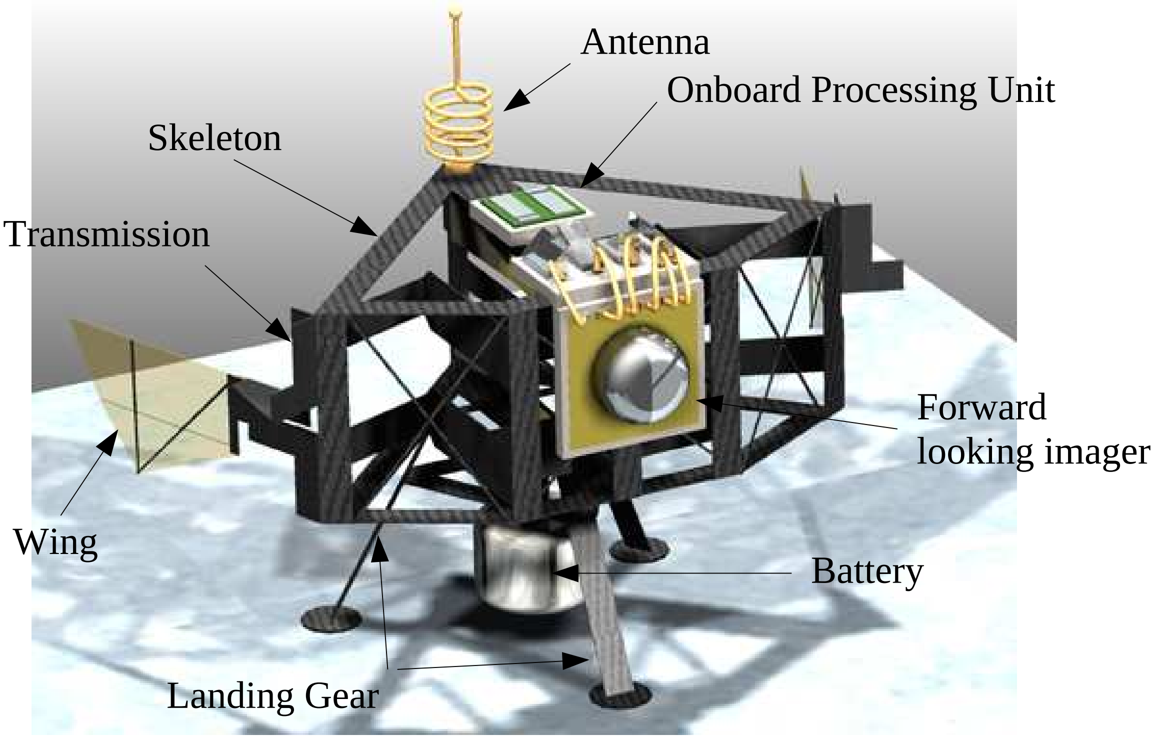

Figure 1.1: Futuristic view of MFI (courtesy Quan Gan)

density perspective although it is still 20 times too heavy to be useful for the MFI. See [Steltz 06] for more details on the current state of the art in battery technology. It is believed that a strategy of using solar cells to charge lithium ion batteries will ultimately be needed to supply the needed power with the required power density and weight requirements. Since the actuator technology currently used in the MFI requires high voltages (on the order of a few hundred volts) not normally produced by batteries, the MFI will also require circuitry to perform charge recovery [Campolo 03] during the process of boosting the voltage [Steltz 06].

Actuators : The MFI uses piezo electric bending actuators to convert electrical energy into mechanical motion. These actuators are described at great length in [Wood 04]. Briefly, these actuators consist of electro active piezo materials bonded to an elastic layer. By applying a voltage across the PZT plates, the induced strain in the PZT is converted into a bending motion. The design of the PZT actuators is carefully optimized to increase the power density and life-time of the actuators. The PZT bimorph actuators used in the MFI have a power density exceeding the best electromagnetic motors at the scale [Wood 04].

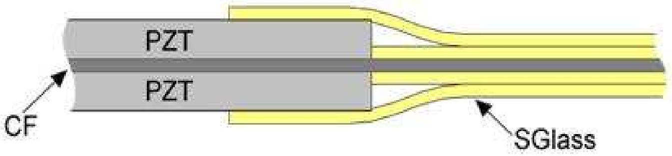

(a) Actuator Layup

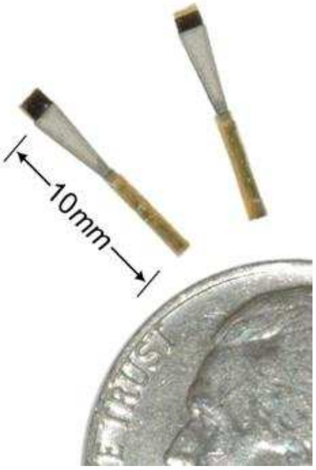

(b) Top view of latest bimorph actuator

Figure 1.2: Photo of piezo-electric bimorph actuator

For the rest of this work, we will assume that the actuators are ideal force sources with an internal spring, damper and inertia. The bimorphs described in [Wood 04] can generate very high forces on the order of 130 mN, with an accompanying displacement of around about 400 μm. The self-resonance of these actuators is very high, around 3000Hz, so that we can assume that in the frequency range of interest (up to 500Hz), the actuators behave quasi-statically.

We should note however, that this is a significant simplification of the actual behavior of the actuator. In practice, PZT actuators exhibit non-linear behavior such as creep, hysteresis, softening and velocity dependent damping (i.e., the quality factor decreases with increasing amplitude). Characterizing the behavior of PZTs is still an ongoing research topic.

Mechanical Transmission : The mechanical transmission system is the focus for the rest of this thesis. Since the actuators used in the MFI are very high stiffness, low displacement actuators, a mechanical transmission system is needed to convert this motion into the high amplitude, relatively low torque motion required at the wing hinge. Briefly, it consists of three separate components:

1. A slider crank mechanism for converting the linear motion of the actuator into a pure rotation and to provide initial amplification. The present day MFI slider crank provides a nominal transmission ratio of about 35° of angular motion for about a millimeter of actuator motion.
2. A fourbar mechanism for providing additional mechanical motion amplification. The present MFI fourbar provides a rotational amplification of 6

(input angle to output angle).

3. Each wing of the MFI is driven by two independent actuators. The motion from the two actuators is amplified by two independent slider crank / fourbar chains. The rotational motion at the output of the fourbars is coupled through a spherical five bar mechanism described in detail in Section 2.3. Briefly, the differential couples the two fourbar motions in such a manner that moving the actuators (and hence the fourbars) in phase allows the wing to purely flap, while moving the fourbars out of phase leads to wing rotation. This is the critical component for achieving the required 2 DOF motion necessary for generating lift.

Sensors : The sensors required for the MFI can be divided into several hierarchical levels. At the lowest level are sensors needed to sense the wing position if closed loop control around the wing trajectory control is required. The current strategy for the low level wing control is to do an off-board characterization of the wing dynamics followed by a table lookup on the final scale robot. See [Steltz 05] for one possible strategy of doing off-line characterization. Previously, strain gage sensors were also used for wing position sensing [Avadhanula 02]. At a higher level, we require body attitude sensors in order to stabilize the body dynamics. Some possible body orientation sensors inspired by naturally occurring counterparts in insects are halteres, ocelli and optic flow sensors [Wu 03, Wood 04].

1.3 Previous Work

There has been a dramatic increase in micro air vehicle (MAV) research over the last several years. We can roughly divide MAVs into three groups: fixed wing MAVs, rotary wing MAVs and flapping wing MAVs. There are presently a large number of fixed wing MAVs, many of which are commercially available. For example, researchers at Didel [did 06] and EPFL [Nicoud 02] have created a class of "slow flyers", which are indoor MAVs capable of impressive maneuverability. Other smaller fixed wing MAVs include the Black widow from Aerovironment [bla 06], a much smaller and faster fixed wing MAV used for outdoor reconnaissance and the Microglider [Wood 05] from the University of California, Berkeley. For sizes much below the Microglider, rigid wing MAVs will be too excessively fast to be maneuverable.

One way of avoiding this is to use rotary flight to increase the Reynolds number over the airfoil while maintaining a low body velocity. There have been a number of miniature rotary MAVs built. Currently the smallest of these MAVs built using traditional manufacturing tools are the 8.9g Epson microrobot [eps 06] and the 6.9g Pixelito [pix 06] developed by Alexander Van de Rostyne. The smallest rotary MAV is the Stanford mesicopter [mes 06] developed by a team headed by Ilan Kroo.

There are considerably fewer flapping fliers than rigid wing or rotary MAVs. One very interesting flapping flier is the CIA dragonfly [cia 06], which is an ingenious device powered by liquid propellant and stabilized by a laser beam. Some recent flapping flyers are the flapping bird developed by Sunil Agrawal at the University of Delaware [Banala 05, Madangopal 05] and the Microbat being developed by Caltech and the University of California at Los Angeles [Pornsin-Sirirak 01, Pornsin-Sirirak 00]. Both these flapping robots are the size of a small bird and their wing morphology seems to imitate flapping flight in birds rather than insects. To the best of this authors knowledge, there are no groups who are working at the same size and scale as the MFI.

1.4 Contributions

The purpose of this work was to design and fabricate the mechanical transmission of the MFI capable of generating adequate lift forces. Towards this end, the main contributions of this thesis are:

1. The kinematic design of a wing differential mechanism for converting two independent actuator motions into wing flapping and rotation.
2. A thorough dynamic modeling of this mechanism including aerodynamic models derived in [Dickinson 99].
3. A method for dynamically tuning the performance of the thorax in order to make it dynamically easier to drive.
4. Improvements to the novel micro composite fabrication method described in [Wood 04] to account for various flexure performance issues.
5. Finally, and most importantly, the various design methods described here were validated by empirically demonstrating a lift of 1400μN from a single wing. This represents a major breakthrough for flapping fliers at this scale. To the

best of this author's knowledge, this is the first time that a mechanical system has been constructed at this scale capable of generating these flight forces.

Chapter 2

Kinematics

This chapter is taken almost directly from [Avadhanula 01] with some modifications to account for the changed differential design. It also treats the slider crank mechanism in more detail accounting for the non-ideal fabrication and alignment parameters.

As described before, the MFI uses piezo-electric actuators as the primary electromechanical elements, which we model as force sources with associated inertia, stiffness and damping. The displacement from each PZT goes through a two step amplification process via a slider crank mechanism and a fourbar mechanism. Finally, the two independent inputs from the fourbars are coupled through a wing differential mechanism. This kinematic chain is represented shcematically in Fig. 2.1. This chapter describes the geometrical aspects of the various components in the mechanism.

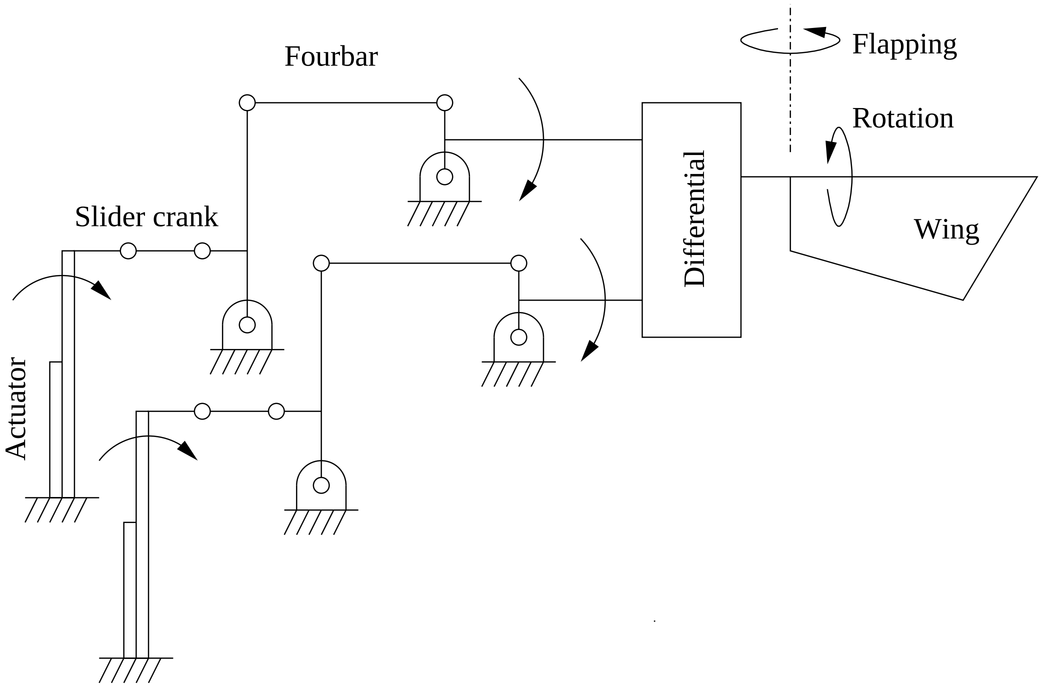

Figure 2.1: Overview of MFI kinematics

2.1 The Slider Crank Mechanism

The first stage of the amplification mechanism is a slider crank mechanism. Geometrically, it is a variant of the classical fourbar mechanism (and is often referred to as a fourbar mechanism). Its purpose in the MFI is to convert the linear motion from the PZTs into a rotary input for the fourbars and also provide a preliminary stage of amplification.

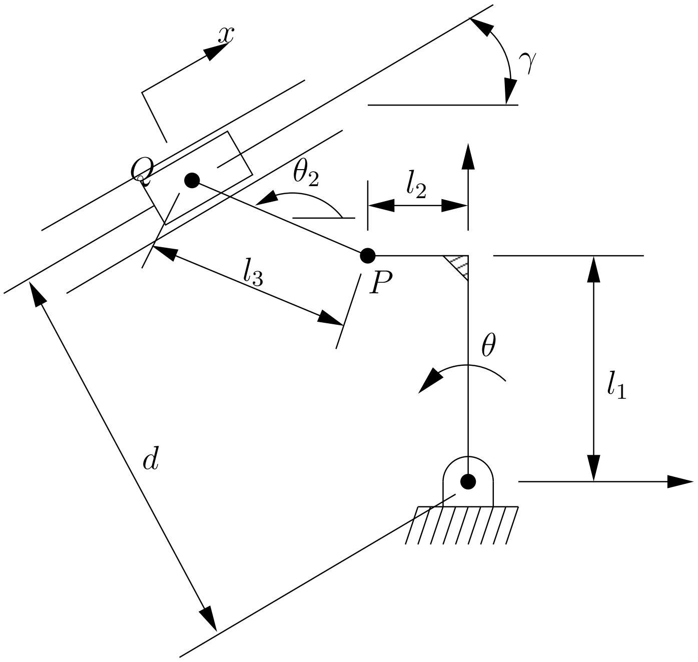

Figure 2.2: Kinematics of the slider crank

Fig. 2.2 shows the kinematic diagram of a slider crank mechanism in the presence of arbitrary misalignment. Ideally, we require that $d = l_1$ and $\gamma = 0$. With these assumptions, the kinematic diagram simplifies to the one described in [Avadhanula 01].

2.1.1 Inverse Kinematics

As we will see in subsequent chapters, from the point of view of analysing the dynamics, we are more interested in the inverse kinematics of the slider crank, i.e., finding the motion x of the actuator for a given rotation θ of the input link of the fourbar in Fig. 2.2.

We first define $x = 0$ when $\theta = 0$. The coordinates of the point Q (written as a complex number in the Argand plane) can be written as:

$$\bar{q} = \bar{p}_0 e^{j\theta} + l_3 e^{j\theta_2}, \tag{2.1}$$

where $\bar{p}_0$ are the initial complex coordinate of the point P when $\theta = 0$, which is

$$\bar{p}_0 \quad = \quad -l_2 + jl_1$$

Alternatively, the coordinates of Q can also be written as

$$\bar{q} = de^{j(\pi/2+\gamma)} + (x + x_0)e^{j\gamma} \tag{2.2}$$

Equating (2.1) and (2.2), we can solve for x in terms of θ. Note that in (2.2) we want to set x_0 to a value which gives $x(\theta = 0) = 0$. The solution of the inverse kinematics problem becomes:

$$\begin{aligned} x &= v_1 + l_3 \cos\beta - x_0 && (2.3) \\ \theta_2 &= \gamma + \beta && (2.4) \end{aligned}$$

where

$$\begin{aligned} v_1 &= \mathrm{Re}\{\bar{p}_0 e^{j(\theta-\gamma)} - de^{j\pi/2}\} && (2.5) \\ \beta &= \sin^{-1}\left(\frac{v_2}{-l_3}\right) && (2.6) \\ v_2 &= \mathrm{Im}\{\bar{p}_0 e^{j(\theta-\gamma)} - de^{j\pi/2}\} && (2.7) \end{aligned}$$

x_0 can be solved from (2.3) by

$$x_0 \quad = \quad v_1(\theta = 0) + l_3 \cos(\beta(\theta = 0))$$

2.1.2 Effect of Fabrication Errors on Kinematics

It is important to analyze the importance of various fabrication errors and misalignments on the actual kinematics achieved. For the slider crank, the two major causes of misalignment arise from $d \neq l_1$ and $\gamma \neq 0$. In order to study this, we find how the nominal inverse slider crank transmission ratio:

$$N_{sc,i}(\theta = 0) := \left| \frac{dx}{d\theta} \right|_{\theta=0}$$

varies as a function of d and γ. As described in [Avadhanula 01], without any fabrication errors, we expect this to be l_1. Fig. 2.3 shows the variation of $N_{sc,i}(0)$ with respect to d and γ. We see that $N_{sc,i}$ varies sharply with γ while not depending very critically on d. It is also significant that the range of variation in $N_{sc,i}$ over these l and d is quite large, from as low as 1.25 to as high as 2.3, almost a factor of 2.

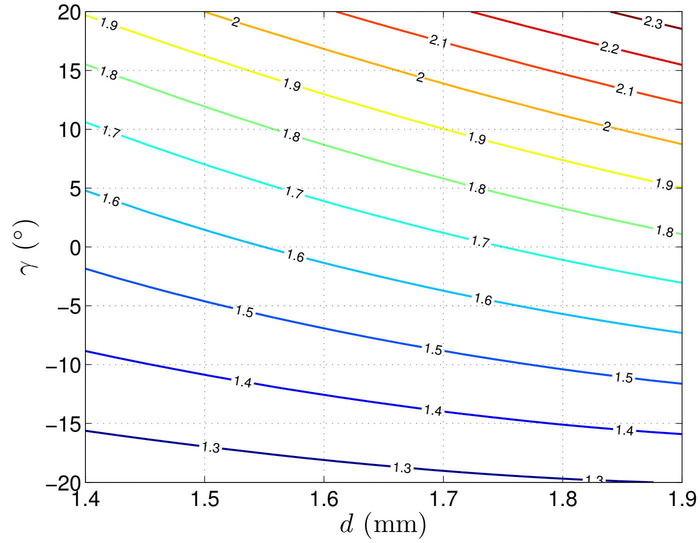

Figure 2.3: Variation of $N_{sc,i}(0)$ with respect to d and γ. The contours represent the values of $N_{sc,i}$ in mm/rads. For this plot the rest of the slider crank dimensions were fixed at $(l_1, l_2, l_3) = (1.65, 0.75, 1.5)$ mm

2.2 The Fourbar Mechanism

The fourbar mechanism is one of oldest and most commonly used mechanical transmission elements. Its many uses include quick return mechanisms used in lathes, crank and piston elements used in car engines and path following mechanisms used in many robotic manipulators. Recently, there have been attempts at fabricating micro and meso scale fourbars using MEMS techniques for micro-bots [Shimoyama 93, Yeh 94, Pornsin-Sirirak 00]. The fourbars used on the MFI are aimed at providing a large motion amplification with little inertial loading and damping losses.

2.2.1 Forward Kinematics

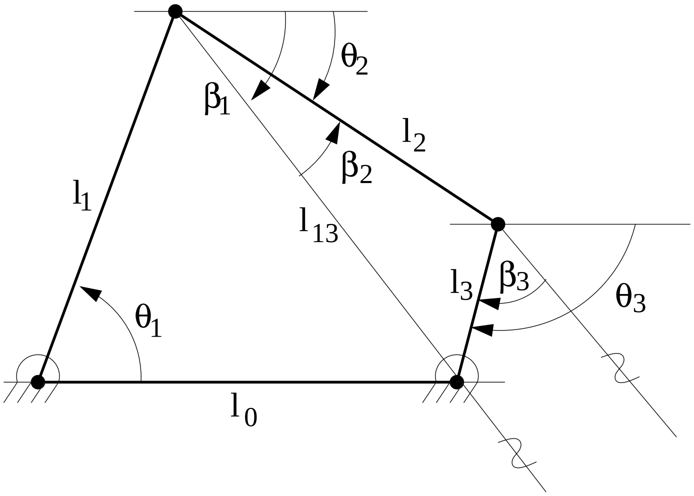

Figure 2.4: Forward Kinematics of the Fourbar Mechanism.

The forward kinematics of the fourbar mechanism involves calculating the output link angles (θ_2 and θ_3 in Fig. 2.4) given the input link angle (θ_1) and the various lengths of the fourbar. This can be calculated as

$$\begin{aligned} \theta_2 &= \beta_1 + \beta_2 && (2.8) \\ \theta_3 &= \beta_1 + \beta_3, && (2.9) \end{aligned}$$

where

$$\begin{aligned} l_{13} &= (l_1^2 + l_0^2 - 2 l_1 l_0 \cos\theta_1)^{1/2} && (2.10) \\ \beta_1 &= \sin^{-1}\left(-\frac{l_1 \sin\theta_1}{l_{13}}\right) && (2.11) \\ \beta_2 &= \cos^{-1}\left(\frac{l_2^2 + l_{13}^2 - l_3^2}{2 l_2 l_{13}}\right) && (2.12) \\ \beta_3 &= \text{atan2}\left(-\frac{l_2 \sin\beta_2}{l_3}, \frac{l_{13} - l_2 \cos\beta_2}{l_3}\right) && (2.13) \end{aligned}$$

The variation of θ_3 vs θ_1 is shown in Fig. 2.5(a). As seen in Fig. 2.5(b), the fourbar mechanism transmission ratio, defined as $\dfrac{d\theta_3}{d\theta_1}$ varies by a factor of 2 over the range of output motions.

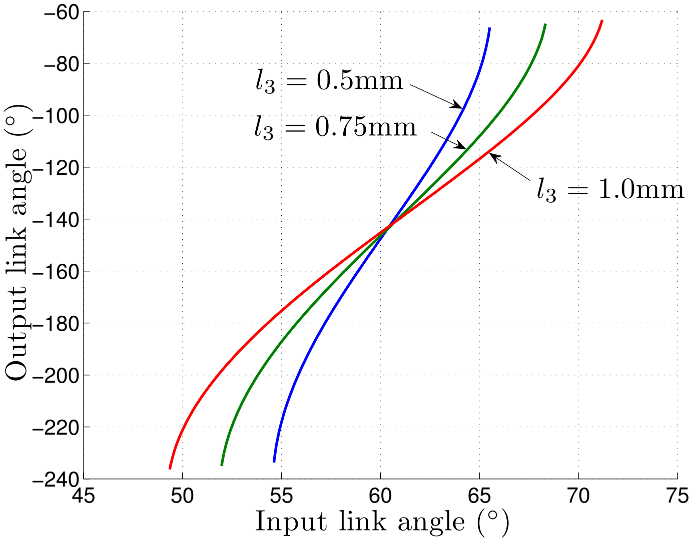

(a) Input-Output Relation

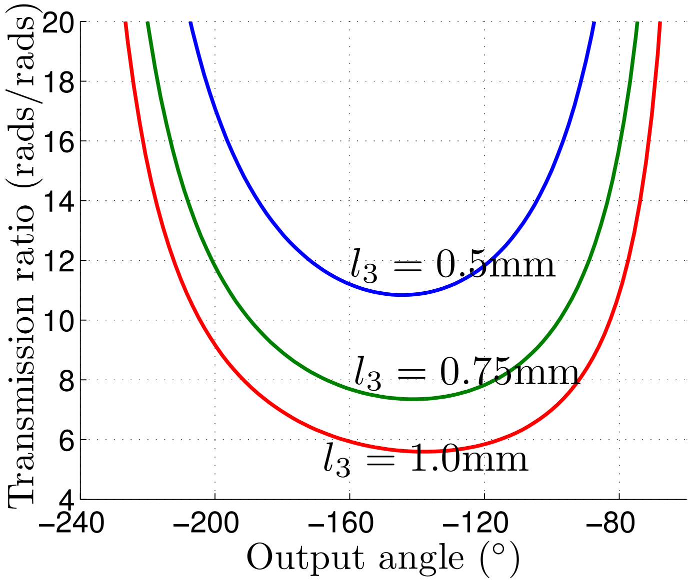

(b) Transmission Ratio ($d\theta_3/d\theta_1$)

Figure 2.5: Kinematics of the Fourbar mechanism.

2.2.2 Inverse Kinematics

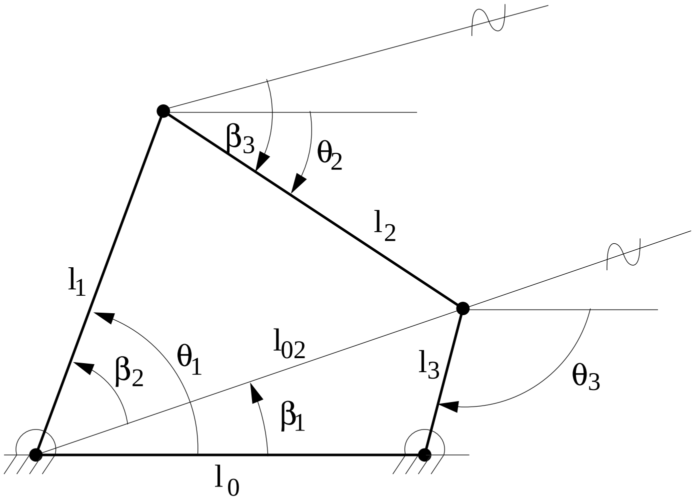

Figure 2.6: Inverse Kinematics of the Fourbar Mechanism.

The inverse kinematics of the fourbar involves finding θ_1 and θ_2 given θ_3. This can be derived from Fig. 2.6 as follows:

$$\theta_1 = \beta_1 + \beta_2 \tag{2.14}$$

$$\theta_2 = \beta_1 + \beta_3, \tag{2.15}$$

where

$$l_{02} = \left((l_0 - l_3 \cos\theta_3)^2 + l_3^2 \sin\theta_3^2\right)^{1/2} \tag{2.16}$$

$$\beta_1 = \operatorname{atan2}(-l_3 \sin\theta_3, l_0 - l_3 \cos\theta_3) \tag{2.17}$$

$$\beta_2 = \cos^{-1}\left(\frac{l_1 + l_{02}^2 - l_2^2}{2 l_1 l_{02}}\right) \tag{2.18}$$

$$\beta_3 = \operatorname{atan2}(-l_1/l_2 \sin\beta_2, (l_{02} - l_1 \cos\beta_2)/l_2) \tag{2.19}$$

2.2.3 Singularities of Motion

Since we are interested in a stroke angle of ±60° it is of interest to calculate the *singularities* of the fourbar mechanism. Geometrically, these are points at which the fourbar hits a joint limit and cannot move further when driven by the input link.

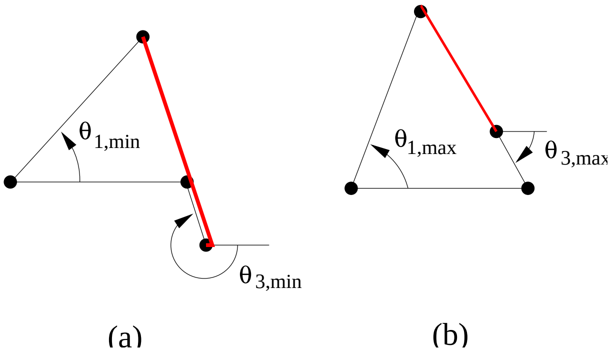

Figure 2.7: Fourbar Singularities (a) "Lower" Singularity (b) "Upper" Singularity.

These angles can be calculated as follows (see Fig. 2.7):

$$\theta_{1,min} = \cos^{-1}\left(\frac{l_1^2 + l_0^2 - (l_2 - l_3)^2)}{2l_1 l_0}\right) \tag{2.20}$$

$$\theta_{1,max} = \cos^{-1}\left(\frac{l_1^2 + l_0^2 - (l_2 + l_3)^2)}{2l_1 l_0}\right) \tag{2.21}$$

$$\theta_{3,min} = \sin^{-1}\left(-\frac{l_1 \sin\theta_{1,min}}{l_2 - l_3}\right) - \pi \tag{2.22}$$

$$\theta_{3,max} = \sin^{-1}\left(-\frac{l_1 \sin\theta_{1,max}}{l_2 + l_3}\right) \tag{2.23}$$

Mathematically, these are points at which the forward and inverse transmission ratio functions go to ∞ or 0 respectively. This has a significant effect on the effectiveness of the fourbar in driving the output as will be seen in Chapter 3.

2.3 The Wing Differential Mechanism

The kinematics of the wing differential mechanism was described previously in [Avadhanula 01]. However, since that time, the mechanism has undergone a significant kinematic improvement. The spherical joint in the original differential consisting of 3 orthogonal flexures has been replaced by a single transverse flexure. This was made possible by improved fabrication techniques which permit much better alignment than in previous methods described in [Shimada 00].

The kinematics of the latest wing differential mechanism are shown in Fig. 2.8. The mechanism consists of four mobile links labelled $\boxed{1}$-$\boxed{4}$ and five joints: 2 about the Z and one each about X, Y and W. The differential is constructed such that all the axes intersect at a single point. This implies that the differential is a spherical mechanism as described in [Releaux 76].

The fourbar output links drive links $\boxed{1}$ and $\boxed{4}$. The wing lamina is attached to link $\boxed{2}$. Link $\boxed{3}$ passively rotates about θ_y to provide the required mobility to the differential. The question of the mobility of the differential is non-trivial and will be addressed later. For now, we claim that we can solve uniquely for θ_x, θ_y and θ_w given arbitrary values of θ_1 and θ_2 as long as $|\theta_1 - \theta_2|$ is not too large. In particular, when $\theta_1 = \theta_2$, then all the links rotate about the global $+Z$ axis. This is defined to be pure flapping. When $\theta_1 \neq \theta_2$, then in addition to some rotation about the $+Z$ axis, the links also undergo rotations about the θ_x and θ_y axes. We call θ_x the ***rotation*** of the wing and θ_y the ***deviation***. Note that θ_y is analogous to the *deviation from stroke plane* mentioned in [Dickinson 99].

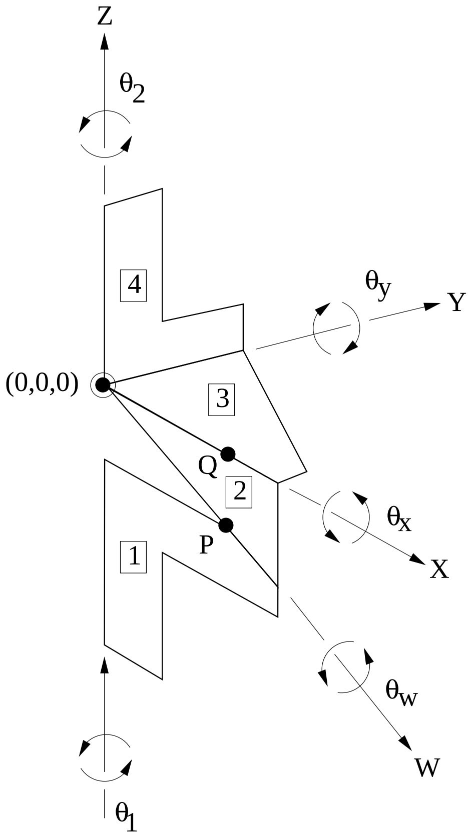

Figure 2.8: Kinematic representation of the wing differential mechanism.

2.3.1 Kinematics of the Wing Differential

In this section, we derive the forward and inverse kinematics of the wing differential mechanism. We define α as the difference in the fourbar angles:

$$\alpha = \theta_1 - \theta_2 \tag{2.24}$$

It should be noted that the angles θ_x and θ_y depend purely on α. Therefore we can restrict the leading spar rotation to zero (i.e, $\theta_2 = 0$) and consider the lagging spar to have rotated through α (i.e, $\theta_1 = \alpha$). The coordinates of the point P in Fig 2.8 in this configuration can then be found in 2 ways:

$$\mathbf{p} \quad = \quad T_z(\theta_1)\mathbf{p}_0 \tag{2.25}$$

$$\mathbf{p} \quad = \quad T_y(\theta_y)T_x(\theta_x)\mathbf{p}_0 \tag{2.26}$$

where $\mathbf{p}_0$ is the initial position of the point P when $\theta_1 = \theta_2 = 0$. Including a scaling factor, we can always consider the initial position of the point P to be $(\lambda, 0, -1)$. This λ is defined to be the differential transmission ratio. More formally:

$$\lambda := \tan(\angle(OP, OQ)) \tag{2.27}$$

Substituting $\mathbf{p}_0 = (\lambda, 0, -1)$ and $\theta_1 = \alpha$ into (2.25,2.26) and equating, we get

$$\begin{bmatrix} \lambda\cos(\alpha) \\ \lambda\sin(\alpha) \\ -1 \end{bmatrix} = \begin{bmatrix} \cos(\theta_y)\lambda - \cos(\theta_x)\sin(\theta_y) \\ \sin(\theta_x) \\ -\sin(\theta_y)\lambda - \cos(\theta_y)\cos(\theta_x) \end{bmatrix} \tag{2.28}$$

In the above equation, we want to solve for θ_x and θ_y given λ and α. This involves equating three equations in two variables. Therefore, it is not obvious that we will get a solution at all. This concern will be addressed later. For now, equating the second element of the two vectors, we can solve for θ_x as:

$$\theta_x \quad = \quad \sin^{-1}(\lambda\alpha) \tag{2.29}$$

If we equate the first element of the two vectors in (2.28), then we get:

$$\lambda\cos\alpha \quad = \quad \lambda\cos\theta_y - \cos\theta_x\sin\theta_y \tag{2.30}$$

In the equation above θ_y is the only unknown. We solve for it by defining two new constants A and β which satisfy

$$\begin{aligned} \lambda &= A\cos\beta && (2.31) \\ \cos\theta_x &= A\sin\beta && (2.32) \end{aligned}$$

This gives us

$$\theta_y = \cos^{-1}\left(\frac{\lambda\cos\alpha}{A}\right) - \beta \tag{2.33}$$

where

$$\begin{aligned} A &= \sqrt{\lambda^2 + \cos^2\theta_x} && (2.34) \\ \beta &= \tan^{-1}\left(\frac{\theta_x}{\lambda}\right) && (2.35) \end{aligned}$$

To solve for θ_w given α, we consider the situation where $\theta_1 = 0$ and $\theta_2 = -\alpha$ (so that $\theta_1 - \theta_2 = \alpha$). The coordinates of the point Q in Fig 2.8 can then be found in two ways

$$\begin{aligned} \mathbf{q} &= T_z(-\alpha)T_y(\theta_y)\mathbf{q}_0 && (2.36) \\ \mathbf{q} &= T_w(\theta_w)\mathbf{q}_0 && (2.37) \end{aligned}$$

where $\mathbf{q}_0$ is the initial position of the point Q. Including a scaling factor, this is simply $(1,0,0)'$. In the first of the two equations above, we already know θ_y given α from (2.33). Therefore, in the second equation above, the only unknown in the equation is θ_w. This is the well known Paden-Kahan subproblem-1 [Murray 93]. To solve, define the vector

$$\hat{w} = \frac{(\lambda, 0, -1)'}{\sqrt{1+\lambda^2}} \tag{2.38}$$

which represents the axis W. (Note that $\|\hat{w}\| = 1$). We want to find the rotation θ_w about $\hat{w}$ takes the point Q from $\mathbf{q}_0$ to $\mathbf{q}$. Define $\mathbf{q}_{0,T}$ and $\mathbf{q}_T$ as the "components" of $\mathbf{q}_0$ and $\mathbf{q}$ along $\hat{w}$. These can be found simply as:

$$\mathbf{q}_{0,T} = (\hat{w}'\mathbf{q}_0)\hat{w} \tag{2.39}$$

$$\mathbf{q}_T = (\hat{w}'\mathbf{q})\hat{w} \tag{2.40}$$

The components perpendicular to $\hat{w}$ are simply

$$\mathbf{q}_{0,N} = \mathbf{q}_0 - \mathbf{q}_{0,T} \tag{2.41}$$

$$\mathbf{q}_N = \mathbf{q} - \mathbf{q}_T \tag{2.42}$$

For the Paden Kahan problem to be solvable, we require

$$\mathbf{q}_{0,T} \equiv \mathbf{q}_T \tag{2.43}$$

$$\|\mathbf{q}_{0,N}\| \equiv \|\mathbf{q}_N\| \tag{2.44}$$

It is not trivial to see that these two conditions will always be satisfied for any α (assuming $\|\alpha\|$ is not too large). For now, we assume that this is true. Once the normal components are known, we can find θ_w as

$$\theta_w = \operatorname{arctan2}\left(\hat{w}'(\mathbf{q}_{0,N} \times \mathbf{q}_N), \mathbf{q}_{0,N}^T \mathbf{q}_N\right) \tag{2.45}$$

The kinematic relationships derived in this section are shown in Fig 2.9.

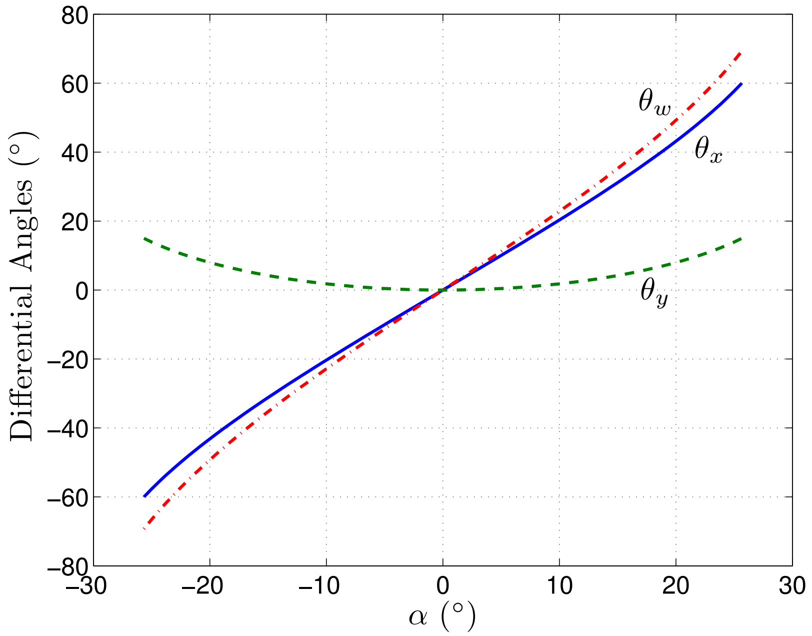

Figure 2.9: Kinematics of the Wing Differential.

It will also be useful for later to define the derivatives of the various angles, especially θ_x with respect to α. We can compute analytical expressions for the various derivatives using the symbolic toolbox of MATLAB. Although the analytical forms of these derivatives are not particularly useful, it is of interest to note that

$$\frac{d\theta_x}{d\alpha} = \frac{\lambda \cos\alpha}{\sqrt{1-\lambda^2 \sin\alpha}} \tag{2.46}$$

which gives

$$\left.\frac{d\theta_x}{d\alpha}\right|_{\alpha=0} = \lambda$$

which is the reason why we call λ the differential transmission ratio. In order to get an idea of the non-linearity of the differential, it is useful to see how much $d\theta_x/d\alpha$ varies with α. This is shown in Fig 2.10.

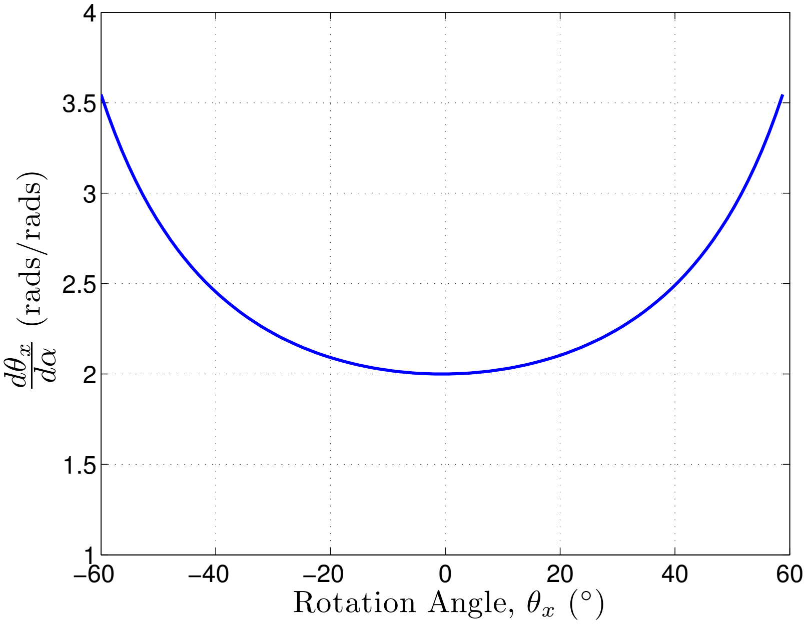

Figure 2.10: Transmission ratio of the Wing differential

2.3.2 Singularities

As in the case of the fourbar, the *singularities* of the wing differential represent the physical limits on the motion of the wing. The singularities follow directly from eqn. 2.29 as:

$$\theta_{x,min} = -\pi/2 \tag{2.47}$$

$$\theta_{x,max} = \pi/2 \tag{2.48}$$

$$\alpha_{min} = -\sin^{-1}\left(\frac{1}{\lambda}\right) \tag{2.49}$$

$$\alpha_{max} = \sin^{-1}\left(\frac{1}{\lambda}\right) \tag{2.50}$$

It is of interest to note that the maximum rotation possible mathematically is $\pi/2$. However, it can be shown that the differential transmission ratio ($\frac{d\theta_x}{d\alpha}$) goes to infinity very rapidly as $\theta_x \to \pi/2$, which means it becomes increasingly difficult to generate larger angles of attack. For example, when $\lambda = 2$, the differential transmission ratio increases five-fold for a rotation of 80° from its nominal value and ten-fold for a rotation of 85°.

2.3.3 Mobility of the wing differential

It is important to note that the fact that the differential works in a kinematic sense is not obvious at all. In other words, it is not trivial that there are solutions to the forward and inverse kinematics for arbitrary θ_1 and θ_2. To get a sense for why this is true, we can begin by analysing the mobility of the spherical five bar mechanism using the 3D version of Gruebler's mobility criterion. In 3D, each (ungrounded) link has 6 degrees of freedom and a revolute joint between two bodies adds 5 geometric constraints. This means that simplistically speaking, the total degrees of freedom in a mechanism N_l links and N_j joints should be

$$N_{dof} = 6 \times N_l - 5 \times N_j \tag{2.51}$$

The wing differential has 4 mobile links and 5 joints. This gives $N_{dof} = 24 - 25 = -1$. Thus the simplistic Gruebler's criterion claims that the spherical five bar mechanism should have a mobility of -1, whereas we claim a mobility of 2. The reason why Gruebler's criterion underestimates the mobility is due to the fact that the geometric construction of the differential makes some of the constraints added by the joints redundant. The mathematically rigorous way of finding local mobility of a mechanism is to write down all the constraint equations and then find the rank of its Jacobian. A more direct (and constructive) way to prove that the mobility of the differential is

2 is by proving that we can solve self-consistently for the angles θ_x, θ_y and θ_w given arbitrary θ_1 and θ_2 (under the assumption that $|\theta_1 - \theta_2|$ is not too large). Moreover, since we will obtain unique values for the other angles (θ_x, θ_y and θ_w), the mobility is not more than 2.

To prove this, we need to prove the following

- When $\theta_1 = \theta_2$, then the differential moves as a single rigid body about the global Z axis. Therefore, it has a mobility of at least 1. Notice that this mobility depends on the fact that the θ_1 and θ_2 axes are collinear. If this is not true, then even this mobility is not possible.

- When $\theta_1 \neq \theta_2$, then we simply need to prove that the vector equality in (2.28) yields a unique solution for θ_x and θ_y. This will give us another degree of freedom when $\alpha \neq 0$. If we equate the third element of the vectors of (2.28), then we get

  $$1 = \sin(\theta_y)\lambda + \cos(\theta_y)\cos(\theta_x) \tag{2.52}$$

  Using the same constants A and β defined in (2.34),(2.35), we can solve similarly for θ_y as

  $$\theta_y = \sin^{-1}\left(\frac{1}{A}\right) - \beta \tag{2.53}$$

  We need to prove that the values of θ_y obtained in (2.33) and (2.53) are identical.

To prove this, we rewrite A as

$$\begin{aligned} A &= \sqrt{\lambda^2 + \cos^2\theta_x} && (2.54)\\ &= \sqrt{\lambda^2 + 1 - \sin^2\theta_x} && (2.55)\\ &= \sqrt{\lambda^2 + 1 - \lambda^2\sin^2\alpha} && (2.56)\\ &= \sqrt{1 + \lambda^2\cos^2\alpha} && (2.57)\end{aligned}$$

With this in place, all that is left to prove is that

$$\sin^{-1}\left(\frac{1}{\sqrt{1+\lambda^2\cos^2\alpha}}\right) = \cos^{-1}\left(\frac{\lambda\cos\alpha}{\sqrt{1+\lambda^2\cos^2\alpha}}\right) \qquad (2.58)$$

This is true since $\cos^{-1}(x) = \sin^{-1}(\sqrt{1-x^2})$.

2.4 Summary

This chapter described the kinematics of the various components which make up the mechanical transmission of the MFI. These kinematic equations will be used in the next chapter to build a thorough dynamic model of the MFI.

Chapter 3

Dynamics of the MFI Thorax

In this chapter, we derive the complete non-linear dynamic model of the MFI thorax, which consists of the entire mechanical transmission as shown in Fig. 2.1 including the slider cranks, the fourbars, the wing differential and the wing.

The dynamics of the MFI was previously derived in [Avadhanula 01], but one of the important missing components was a model for the aerodynamic forces. This chapter incorporates the aerodynamic force models derived previously [Dickinson 99, Sane 02, Schenato 01, Sane 03] into the MFI wing dynamics. We then describe how we adjust the mechanical design of the system to make the overall dynamics easier to control (as described more precisely in Section 3.5).

3.1 The Euler Lagrange Formulation

The Euler-Lagrange equation formalization states that for a system with holonomic constraints, the following differential equation is satisfied:

$$\frac{d}{dt}\left(\frac{\partial L}{\partial \dot{q}}\right) - \frac{\partial L}{\partial q} = \frac{\partial W_{ext}}{\partial q} \tag{3.1}$$

where, L, the *Lagrangian* is defined as

$$L(q, \dot{q}) = KE(q, \dot{q}) - PE(q), \tag{3.2}$$

and q is the generalized position vector, $\dot{q}$ is the generalized velocity vector and W_{ext} is the work done on the system by external forces. In this section, we derive the complete nonlinear equation based on this formula.

The contributions to the energy arise as follows:

$$KE = KE_{\text{actuators}} + KE_{\text{fourbars}} + KE_{\text{wing-diff}} \tag{3.3}$$

$$\begin{aligned} PE = {} & PE_{\text{actuators}} + PE_{\text{slider-cranks}} \\ & + PE_{\text{fourbars}} + PE_{\text{differential}} \end{aligned} \tag{3.4}$$

The effect of the damping and aerodynamics terms on the overall dynamics (3.1) is seen via the last term, i.e, $\partial W_{ext}/\partial q$. In general, external non-conservative forces such as damping forces acting on the mechanism will depend on the position and velocity of the system. Let us assume for the moment that one of the external forces is $\mathbf{F}_{ext}(q, \dot{q})$ acting at the point $\mathbf{p}(q)$. The work done for a small change in q is given by

$$\begin{aligned} dW_{ext} &= \mathbf{F}_{ext}^T d\mathbf{p} \\ &= \mathbf{F}_{ext}^T \frac{\partial \mathbf{p}}{\partial q} dq. \end{aligned}$$

Thus

$$\frac{\partial W_{ext}}{\partial q} = \mathbf{F}_{ext}^T(q, \dot{q}) \frac{\partial \mathbf{p}(q)}{\partial q} \tag{3.5}$$

The external forces arise from the aerodynamic force felt by the wing as well as internal damping forces (which need to be modeled as an external force):

$$W_{ext} = W_{\text{aero}} + W_{\text{struct}} \tag{3.6}$$

For our analysis, we choose the generalized position and velocity vectors as

$$q = \{\theta_2, \alpha\}^t \tag{3.7}$$

$$\dot{q} = \{\dot{\theta}_2, \dot{\alpha}\}^t \tag{3.8}$$

In the following sections, we derive expressions for each of the terms in (3.3), 3.4 and 3.6 in terms of q and $\dot{q}$.

3.2 Aerodynamics of the MFI thorax

In this section we describe in detail the aerodynamic model described in [Dickinson 99, Sane 02, Schenato 01]. We perform some preliminary aerodynamic optimizations of the wing trajectory which gives us an idea of what to aim for, for getting good lift. Finally we describe how to incorporate this model into the overall dynamic model of the MFI.

[Dickinson 99] performed scaled model experiments to experimentally measure the complex aerodynamic forces generated by the motion of an insect wing. The apparatus consisted of a 25 cm scaled model of the insect wing moving in a large tank of mineral oil. By choosing the appropriate velocities and viscosities, the Reynolds number which insects experience in actual flight was reproduced in this apparatus. Force gages mounted at the base of the scaled wing measured the forces experienced by the model wing in real time. By careful analysis of the measured forces, three primary lift producing mechanisms were discovered: delayed stall, rotational lift and wake capture.

[Schenato 01] and [Sane 02] used these experimental measurements and combined them with theoretical analysis to come up with a mathematical model which predicts the instantaneous aerodynamic forces experienced by an insect wing in real time. This model only uses the instantaneous value of the orientation and velocity of the wing, thus ignoring the effect of wake capture. Wake capture is thought to contribute to about 10% of the total aerodynamic lift in a typical insect wing trajectory. It is reasonable to ignore wake capture for the MFI since we are for the present restricted to much slower rotations than in an actual insect so that the interaction between the present rotational velocity with previously generated wake is expected to be lesser than in an insect. See Fig. 7 from [Schenato 01] for a comparison of the scaled measurement data to the theoretical prediction for a smoothly sinusoidal wing trajectory.

3.2.1 Geometric Specification

Consider a wing lamina attached to the MFI wing differential as shown in Fig. 3.1. The wing is initially assumed to lie in the $(+X, -Z)$ quadrant and subsequently undergo rotations about the Z, Y and X axes (in that order). The direction of the

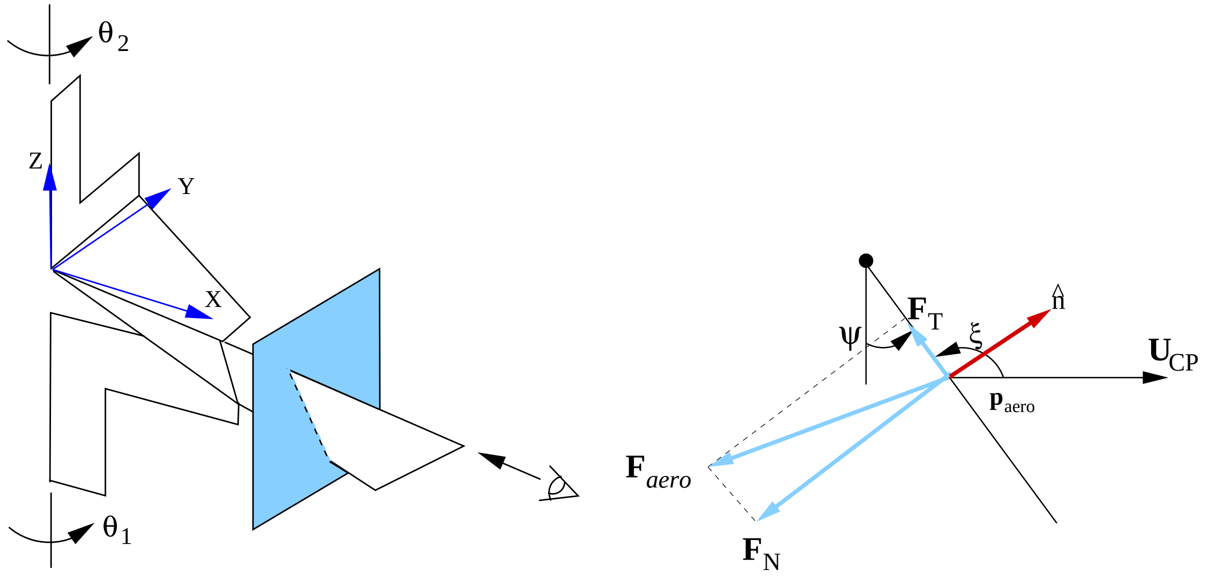

(a) (b)

Figure 3.1: Wing Aerodynamics (a) Aerodynamic Force acting on wing (b) Cross-section of wing showing aerodynamic forces

wing normal is given by:

$$\hat{\mathbf{n}} = T_z(\theta_2)T_y(\theta_y)T_x(\theta_x)\hat{\mathbf{n}}_0, \tag{3.9}$$

where $\hat{\mathbf{n}}_0$ is the initial orientation of the wing normal when $\theta_1 = \theta_2 = 0$ and $T_r(\gamma)$ represents a rotation through angle γ about the axis $\hat{\mathbf{r}}$. For our particular geometry $\hat{\mathbf{n}}_0 = \{0, 1, 0\}'$. Moreover, since θ_x and θ_y depend purely on the phase difference α, as in the case of the kinetic energy of the wing, it becomes convenient to define:

$$T_1(\theta_2) = T_z(\theta_2) \tag{3.10}$$

$$T_2(\alpha) = T_y(\theta_y)T_x(\theta_x) \tag{3.11}$$

This lets us define

$$\hat{\mathbf{n}} = T_1(\theta_2)T_2(\alpha)\hat{\mathbf{n}}_0 \tag{3.12}$$

The position of the wing center of pressure is given by:

$$\begin{aligned}\mathbf{p}_{aero} &= T_z(\theta_2)T_y(\theta_y)T_x(\theta_x)\mathbf{p}_0, &(3.13)\\ &= T_1(\theta_2)T_2(\alpha)\mathbf{p}_0 &(3.14)\end{aligned}$$

where $\mathbf{p}_0$ is the initial position of the wing center of pressure when $\theta_1 = \theta_2 = 0$.

This force can be decomposed into a normal component (which acts normal to the wing lamina) and a tangential component (which acts in the plane of the wing lamina) as shown in Fig. 3.1(b).

In order to explain results from literature, we will also rigorously define the "angle of attack". This angle is defined as the angle made by the direction of the translation velocity of the wing center of pressure with the wing lamina. This angle is shown as ξ in Fig 3.1. Mathematically, this angle can be expressed in terms of ψ and U_{cp} as follows:

$$\xi = \pi/2 + \psi\ \mathbf{sgn}(U_{cp}) \tag{3.15}$$

Thus

$$\dot{\xi} = \dot{\psi}\ \mathbf{sgn}(U_{cp}) \tag{3.16}$$

which gives

$$\mathbf{sgn}(\dot{\xi}) = \mathbf{sgn}(\dot{\psi})\mathbf{sgn}(U_{cp}) \tag{3.17}$$

3.2.2 Delayed Stall

The magnitude of the aerodynamic force exerted on the wing due to delayed stall is given by the following components:

$$|F_{tr,N}(t)| = \frac{1}{2}\rho A_w C_N(\psi(t))U_{cp}^2(t) \tag{3.18}$$

$$|F_{tr,T}(t)| = \frac{1}{2}\rho A_w C_T(\psi(t))U_{cp}^2(t) \tag{3.19}$$

In the equations above, $U_{cp}(t)$ refers to the instantaneous velocity of the wing center of pressure relative to the fluid and A_w refers to the wing area, ρ is the density of air, ψ is the angle of attack and A_w is the wing area C_N and C_T are dimensionless aerodynamic constants which will be described later. U_{cp} is calculated as

$$U_{cp}(t) = \hat{r}_2 R\dot{\theta}_2 \tag{3.20}$$

In the equation above, $\hat{r}_2$ refers to the equivalent radius of the area moment of the wing normalized by the longitudinal wing length, R. In other words, the area moment of the wing is the same as if the entire area were concentrated at a distance $\hat{r}_2 R$. Therefore, if the chord length of the wing varies as $c(r)$, $\hat{r}_2$ can be calculated as:

$$\hat{r}_2 = \frac{\int_0^R c(r)r^2 dr}{R^2 A_w} \tag{3.21}$$

Note that if we substitute (3.21) into (3.20) and back into (3.18), (3.19), we see that the translational forces depend purely on the second moment of area of the wing. Another thing to note is that the instantaneous translational forces depend on the current orientation of the wing in addition to its velocity, due to the dependence of

C_N and C_T on the rotation angle ψ. This dependence is given as [Dickinson 99]:

$$C_N(\psi) = 3.4\cos\psi \tag{3.22}$$

$$C_T(\psi) = \begin{cases} 0 & 0 < \psi < 45^\circ \\ 0.4\cos^2(2\psi) & \text{otherwise} \end{cases} \tag{3.23}$$

Fig. 3.2 shows the variation of C_N and C_T with respect to the wing rotation ψ. It is clear that C_T is very small compared to C_N, which therefore means that $F_{tr,T}$ is significant only for very large rotations. In practice, we want to avoid rotations of more than about 60°, which means that C_T is restricted to be about 0.1. This means that for all practical wing trajectories, we can reasonably neglect the effect of $F_{tr,T}$ on the wing dynamics. Therefore the magnitude of the translational force is given by (3.18). The direction of the translation force $\hat{F}_{tr}$ is always either parallel or anti-parallel to $\hat{\mathbf{n}}$ and it always points away from the direction of U_{cp}. We can write this dependence as:

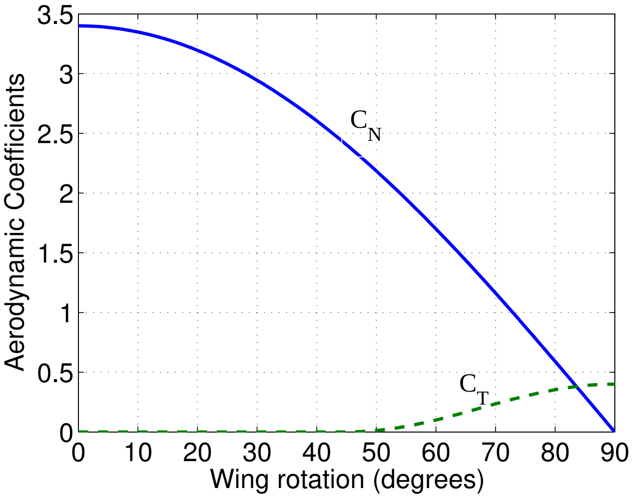

Figure 3.2: Variation of force coefficients with wing rotation

$$\hat{F}_{tr} = -\mathbf{sgn}(U_{cp})\hat{\mathbf{n}} \tag{3.24}$$

In summary, the translation force is given by:

$$\begin{aligned}\mathbf{F}_{tr} &= |F_{tr}|\hat{F}_{tr} \\ &= -\frac{1}{2}\rho A_w C_N(\psi(t))U_{cp}^2(t)\mathbf{sgn}(U_{cp}(t))\hat{\mathbf{n}} \\ &= -\frac{1}{2}\rho A_w C_N(\psi(t))U_{cp}|U_{cp}(t)|\hat{\mathbf{n}} \qquad (3.25)\end{aligned}$$

3.2.3 Rotational Lift

The aerodynamic effect of wing rotation has undergone extensive study. Some of the first studies into its effect was done by [Fung 69], where the effect of small oscillations on aerofoils in a low angle of attack and very high Reynolds number regime was explored. Some of the circulation assumptions made there have been carried over by biologists [Dickinson 99, Sane 02] to aerofoils which are undergoing large rotations in a very low Reynolds number regime (Re about 150). A major assumption consistently made in literature is that the rotational force is a normal pressure force. Therefore, it always acts normal to the wing lamina. The magnitude of the rotational force is calculated in [Sane 02, Schenato 03] as

$$|F_{rot}(t)| = \frac{1}{2}\rho A_w \hat{c} c_{max} C_{rot}|\dot{\psi}(t)||U_{cp}(t)| \qquad (3.26)$$

In the above equation, c_{max} is maximum wing chord width, and $\hat{c}$ is the normalized rotational chord which is calculated as:

$$\hat{c} = \frac{\int_0^R c^2(r)rdr}{\hat{r}_2 R A_w c_{max}} \qquad (3.27)$$

The rotational coefficient of lift, C_{rot} is given by

$$C_{rot} = 2\pi\left(\frac{3}{4} - \hat{x}_0\right) \qquad (3.28)$$

In the equation above, $\hat{x}_0$ is the normalized distance of the rotational axis from the leading edge. In most insects, this is believed to be around 1/4 [Dickinson 99]. For the moment we will assume that it is the same for the MFI. It should be noted that this formulation ignores the effect seen in [Sane 02] of the dependence of C_{rot} on $\dot{\psi}$.

Looking at Fig (3) from [Sane 02], the following deduction can be made about the direction of the rotational force. Firstly, since its a normal pressure force, it is always either parallel or anti-parallel to the wing normal. In the case where the angle of attack is increasing, then the rotational force points in the same direction as the translation force (away from the wing translational velocity). In the case where the angle of attack is decreasing, then the force points opposite to the direction of the translation force (towards the translational velocity). Mathematically, this directional dependence can be summarized as:

$$\hat{F}_{rot} = \mathbf{sgn}(\dot{\xi})\hat{F}_{tr} \tag{3.29}$$

As explained in [Sane 03], the rotational force is *not* analogous to the Magnus force to which it was previously likened [Dickinson 99], but in fact, it is a manifestation of the Kramer effect. For example, consider the case of advanced rotation of the wing. Just before the end of the downstroke, the wing has an angle of attack $> 90°$ and still increasing while the wing is still moving forward. This corresponds to the situation as shown in Fig. 3.3. Thus although the Magnus effect would predict a lift *increase* in this situation, we actually get a negative lift due to rotation. To summarize, we find the direction of rotational lift by substituting (3.17) and (3.24) into (3.29).

$$\begin{aligned}\hat{F}_{rot} &= (\mathbf{sgn}(\dot{\psi})\mathbf{sgn}(U_{cp}))(-\mathbf{sgn}(U_{cp})\hat{\mathbf{n}}) \\ &= -\mathbf{sgn}(\dot{\psi})\hat{\mathbf{n}} \end{aligned} \tag{3.30}$$

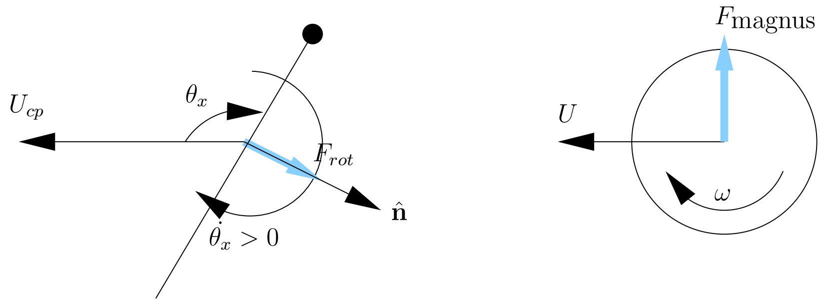

Figure 3.3: Difference between rotational lift and the Magnus effect. The left image shows the rotational component of the force on a wing lamina. In this situation, θ_x denotes the angle of attack. In this case, it is still increasing. According to [Sane 02], this leads to a rotational lift force as shown which has a negative lift component. An equivalent tennis ball spinning as shown would experience a positive lift.

Therefore, the vector representation of the rotational force is given by:

$$\begin{aligned}\mathbf{F}_{rot} &= |F_{rot}|\hat{F}_{rot} \\ &= -\frac{1}{2}\rho A_w \hat{c} c_{max} C_{rot} |\dot{\psi}(t)||U_{cp}(t)|\mathbf{sgn}(\dot{\psi})\hat{\mathbf{n}} \\ &= -\frac{1}{2}\rho A_w \hat{c} c_{max} C_{rot} \dot{\psi}(t)|U_{cp}(t)|\hat{\mathbf{n}} \qquad (3.31)\end{aligned}$$

3.2.4 Wake Capture

Wake capture is a complex phenomenon which arises due to an interaction of the insect wing with the wake which it creates due to a previous flap. When an insect rapidly moves its wings through a fluid, the fluid is given some momentum and continues to move forward. The insect wing leads this wake during the forward stroke. When the wing reverses direction and begins to travel backwards, it encounters this moving fluid, leading to an increased relative fluid flow and thereby increased aerodynamic forces. This mechanism is hard to model because it would require a model of how flow induced in a fluid by a wing decays with time. In addition, it is a highly transient effect which only generates lift in the very beginning of a stroke. We do not include this mechanism in modeling the aerodynamic force due to the wing motion.

3.2.5 Total Aerodynamic Force

Summarizing the last few sections, we can model the total aerodynamic force acting on the wing as:

$$\begin{aligned}\mathbf{F}_{aero} &= \mathbf{F}_{tr} + \mathbf{F}_{rot} \\ &= F_{aero}(\psi, \dot{\psi}, U_{cp})\hat{\mathbf{n}}, \end{aligned} \tag{3.32}$$

where F_{aero} is defined as the scalar quantity

$$F_{aero}(\psi, \dot{\psi}, U_{cp}) = -\frac{1}{2}\rho A_w \left\{ C_N(\psi(t))U_{cp}(t)|U_{cp}(t)| + \hat{c}c_{max}C_{rot}\dot{\psi(t)}|U_{cp}(t)| \right\} \tag{3.33}$$

and $\hat{\mathbf{n}}$ is defined in (3.12). From this, we can extract the lift force as the component of the total aerodynamic force along the vertical direction. In other words:

$$\mathbf{F}_L = (\mathbf{F}_{aero}^T \hat{\mathbf{z}})\hat{\mathbf{z}}, \tag{3.34}$$

where $\hat{\mathbf{z}}$ refers to the unit vector along the global $+Z$ direction. The drag force is defined as the component of the total aerodynamic force in the $X - Z$ plane *opposite to the flapping velocity.*

$$\mathbf{F}_D = (\mathbf{F}_{aero} - \mathbf{F}_L)\mathbf{sgn}(U_{cp}) \tag{3.35}$$

It should be noted that this is *not* equivalent to the thrust force, which we will define as the component of the total aerodynamic force along the global $+Y$ direction:

$$\mathbf{F}_T = (\mathbf{F}_{aero}^T \hat{\mathbf{y}})\hat{\mathbf{y}} \tag{3.36}$$

3.2.6 Preliminary Aerodynamic Optimization

Given a model of how the lift and drag vary with the wing trajectory, the natural question which arises is “What is the wing trajectory (within certain constraints) which maximizes the aerodynamic performance?” The aerodynamic performance can be characterized in various ways. The two most intuitive measures are the mean lift produced over a wing flapping cycle and the mean lift/drag ratio over a flapping cycle. In the following simplified analysis, we restrict the flapping frequency to 200Hz and the flapping amplitude to ±50° and try to find out the rotation amplitude and timing which will optimize these measures. As before, we have defined the wing flapping to be the angle made by the leading spar of the wing differential (θ_2 in Fig. 2.8) and the rotation to be the angle θ_x in Fig.2.8. In other words, with:

$$\begin{aligned}\theta_2(t) &= \frac{50\pi}{180}\cos(2\pi 200t)\\ \theta_x(t) &= \Theta_x \cos(2\pi 200t+\gamma),\end{aligned}$$

we try to find Θ_x and γ which will optimize one of the aerodynamic performance measures. Note that $\gamma = \pi/2$ corresponds to symmetric wing rotation, while $\gamma < \pi/2$ ($\gamma > \pi/2$) corresponds to *advanced* (*delayed*) rotation.

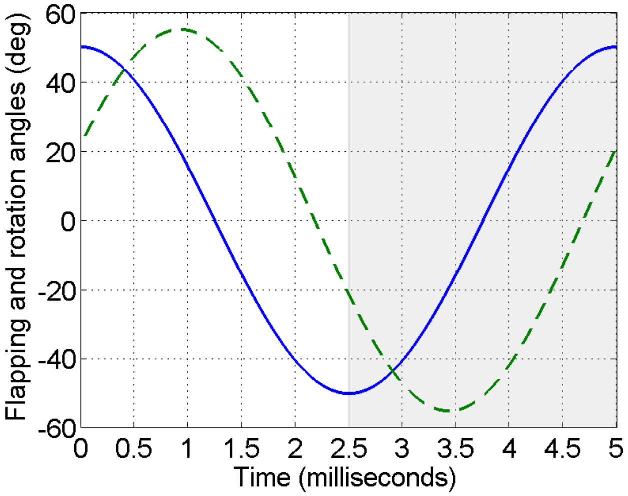

Figure 3.4: Time history of wing flapping and rotation for a typical wing trajectory.

Fig. 3.4 shows a typical wing flapping and rotation trajectory ($\Theta_x = 55°$ and $\gamma = 67°$ for this trajectory). Fig. 3.5 shows the lift and drag forces generated by this wing trajectory.

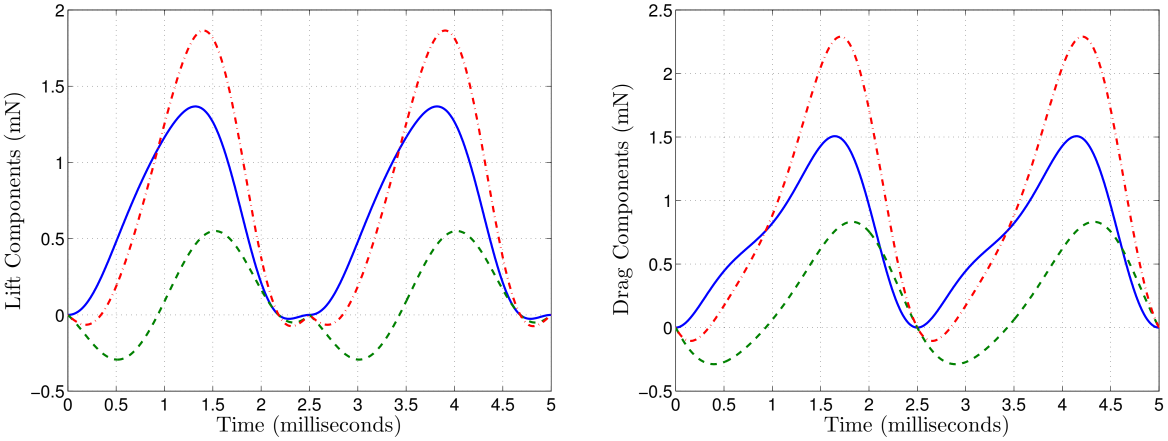

(a) Lift

(b) Drag

Figure 3.5: Time history of lift and drag forces on a wing. These forces correspond to ±50° flapping and ±55° rotation with slightly advanced rotation. The solid lines represents the contribution from delayed stall, the dashed lines represents the contribution from rotational lift and the dashed-dotted lines represents the total lift force.

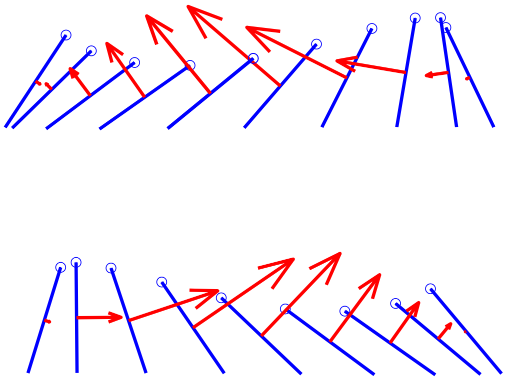

Figure 3.6: Cross-sectional view of wing chord with aerodynamic forces overlaid for an “insect” facing to the right. The top figure therefore shows the downstroke and the bottom figure the upstroke. This kinematic pattern corresponds to a slightly advanced rotation (65° phase difference between flapping and rotation) and a 55° rotational amplitude.

Fig. 3.6 shows the cross-section of the wing with these forces overlaid. Using (3.33) and substituting values of $\psi(t)$, $\dot{\psi}(t)$ and $U_{cp}(t)$ calculated from θ_x, $\dot{\theta}_x$ and $\dot{\theta}_2$, we can get the time history of the lift and drag forces $F_L(t)$ and $F_D(t)$. By averaging this over one wing flapping cycle, we can calculate the mean lift and drag over a wing beat. These mean lift and drag numbers are functions of Θ_x and γ. Fig. 3.7 shows the variation of the mean lift over a wing beat as a function of the rotational amplitude (Θ_x) and the rotation timing (γ). From the figure, we immediately see that the maximum lift is obtained from a wing trajectory which has a rotation of about 55° and with a rotation phase of about 67° (i.e, advanced rotation). This optimal wing trajectory gives a lift of about 750 μN.

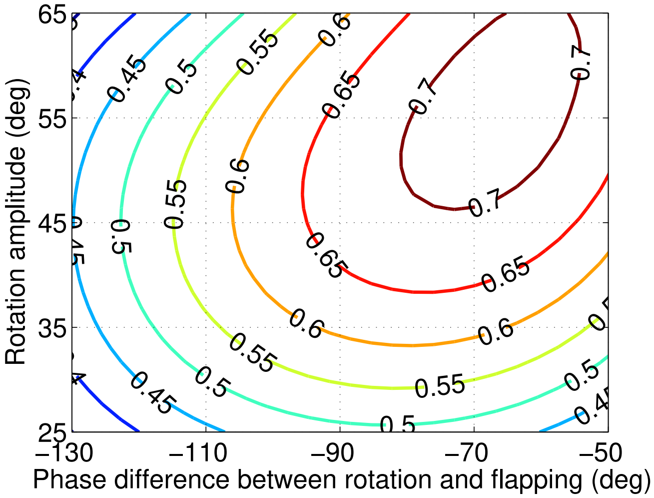

Figure 3.7: Lift contour over the two kinematic parameters. The lift is shown in mN

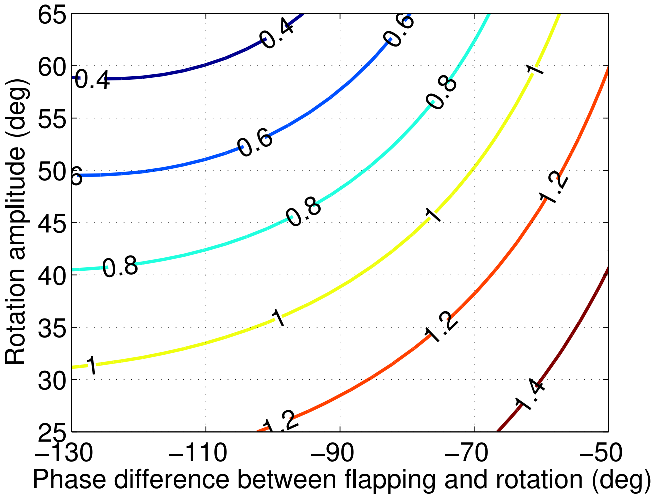

Figure 3.8: Drag contour over the two kinematic parameters. The drag is shown in mN

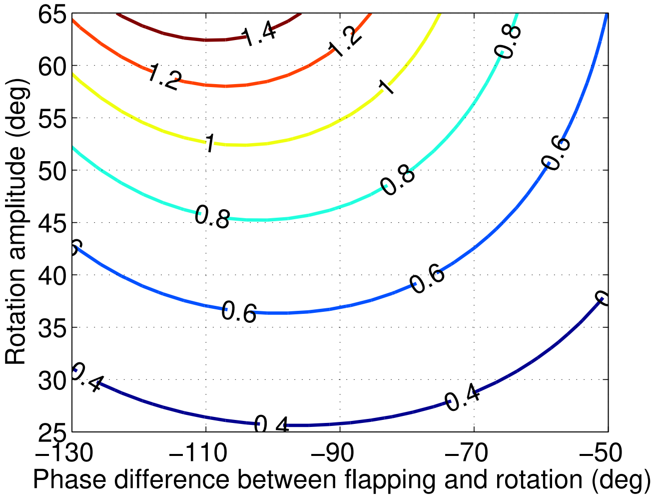

Figure 3.9: Contour of mean lift to drag ratio over the two kinematic parameters of interest.

Fig. 3.8 shows the variation of the mean drag over a wing beat as a function of rotational amplitude and timing. From this figure, we observe that the wing drag over a cycle decreases with increasing rotational amplitude and delayed rotation. For all practical purposes, it is not feasible to attain rotations of more than 65° with the current differential design. Thus there is no "optimal" trajectory which minimizes wing drag. Instead, the rule is to merely increase the rotation amplitude and delay the wing rotation.

Fig. 3.9 shows the variation of the ratio of the mean lift to the mean drag over a wing beat. Like in the case of the drag, there is no clear "optimal" wing trajectory which maximizes this ratio. For the range of reasonable rotation angles, we find the maximum ratio at the maximum possible rotation (65°) and a delayed rotation (the zero rotation point lags the zero flapping velocity point by 20°).

3.2.7 Incorporating Aerodynamics into MFI dynamics

Incorporating the aerodynamic models derived thus far into the wing dynamics of the MFI is simply a matter of using (3.5) and substituting the value of $\mathbf{F}_{aero}$ (3.32) for $\mathbf{F}$ and $\mathbf{p}_{aero}$ (3.13) for $\mathbf{p}$.

$$\begin{aligned}\frac{\partial \mathbf{p}_{aero}}{\partial \theta_2} &= \frac{\partial}{\partial \theta_2}\left(T_1(\theta_2)T_2(\alpha)\mathbf{p}_0\right)\\ &= T_1'(\theta_2)T_2(\alpha)\mathbf{p}_0\end{aligned} \tag{3.37}$$

$$\begin{aligned}\frac{\partial \mathbf{p}_{aero}}{\partial \alpha} &= \frac{\partial}{\partial \alpha}\left(T_1(\theta_2)T_2(\alpha)\mathbf{p}_0\right)\\ &= T_1(\theta_2)T_2'(\alpha)\mathbf{p}_0\end{aligned} \tag{3.38}$$

$$\begin{aligned}\mathbf{F}_{aero} &= F_{aero}(\theta_2, \alpha, \dot{\theta}_2, \dot{\alpha})\hat{\mathbf{n}}\\ &= F_{aero}(\theta_2, \alpha, \dot{\theta}_2, \dot{\alpha})T_1(\theta_2)T_2(\alpha)\hat{\mathbf{n}}_0\end{aligned} \tag{3.39}$$

$$\begin{aligned}\frac{\partial W_{aero}}{\partial \theta_2} &= \left(T_1(\theta_2)T_2(\alpha)F_{aero}(q,\dot{q})\right)^T T_1'(\theta_2)T_2(\alpha)\hat{\mathbf{n}}_0 \\ &= \mathbf{p}_0^T T_2^T(\alpha)T_1^T(\theta_2)T_1'(\theta_2)T_2(\alpha)\hat{\mathbf{n}}_0 F_{aero}(q,\dot{q})\end{aligned} \tag{3.40}$$

$$\begin{aligned}\frac{\partial W_{aero}}{\partial \alpha} &= \left(T_1(\theta_2)T_2(\alpha)F_{aero}(q,\dot{q})\mathbf{p}_0\right)^T T_1(\theta_2)T_2'(\partial\alpha)\hat{\mathbf{n}}_0 \\ &= \mathbf{p}_0^T T_2^T(\alpha)T_1^T(\theta_2)T_1(\theta_2)T_2'(\alpha)\hat{\mathbf{n}}_0 F_{aero}(q,\dot{q})\end{aligned} \tag{3.41}$$

Since the wing is assumed to be a plane lamina initially in the $(X, -Z)$ quadrant, we can use

$$\mathbf{p}_0 = \{x_0, 0, -z_0\}^T \tag{3.42}$$

$$\hat{\mathbf{n}}_0 = \{0, 1, 0\}^T \tag{3.43}$$

Defining

$$\begin{aligned} r_1 &:= \mathbf{p}_0^T T_2^T(\alpha)T_1^T(\theta_2)T_1'(\theta_2)T_2(\alpha)\hat{\mathbf{n}}_0 \\ &= x_0\cos\theta_y\cos\theta_x - z_0\sin\theta_y \end{aligned} \tag{3.44}$$

$$\begin{aligned} r_2 &= \mathbf{p}_0^T T_2^T(\alpha)T_1^T(\theta_2)T_1(\theta_2)T_2'(\alpha)\hat{\mathbf{n}}_0 \\ &= -x_0\theta_y'\sin\theta_x + z_0\theta_x' \end{aligned} \tag{3.45}$$

where $\theta_y' = \dfrac{\partial\theta_y}{\partial\alpha}$ and $\theta_x' = \dfrac{\partial\theta_x}{\partial\alpha}$. As expected, r_1 and r_2 are independent of θ_2 and depend purely on α. Substituting this back into (3.40) and (3.41), we get

$$\frac{\partial W_{aero}}{\partial \theta_2} = (x_0\cos\theta_y\cos\theta_x - z_0\sin\theta_y)F_{aero}(\alpha, \dot{\theta}_2, \dot{\alpha}) \tag{3.46}$$

$$\frac{\partial W_{aero}}{\partial \alpha} = (-x_0\theta_y'\sin\theta_x + z_0\theta_x')F_{aero}(\alpha, \dot{\theta}_2, \dot{\alpha}) \tag{3.47}$$

where F_{aero} is calculated from (3.33). It is of interest to see that when $\alpha = 0$, we get

$$\frac{\partial W_{aero}}{\partial \theta_2} = x_0 F_{aero}(\alpha = 0, \dot{\theta}_2, \dot{\alpha}) \tag{3.48}$$

$$\frac{\partial W_{aero}}{\partial \alpha} = \lambda z_0 F_{aero}(\alpha = 0, \dot{\theta}_2, \dot{\alpha}) \tag{3.49}$$

3.3 Structural dynamics of the MFI thorax

In this section, we describe the contribution to the overall dynamics from the structural components of the MFI thorax, such as the actuator, slider-crank, fourbar and wing differential. Some of these models were described previously in [Avadhanula 01]. However, we very briefly repeat them here for the sake of completion and also to account for slight improvements in the model.

3.3.1 Kinetic Energy of the Actuator

The KE of the actuators is given by:

$$KE_{\text{act}} = \frac{1}{2}(m_{pzt,1}\dot{x}_1^2 + m_{pzt,2}\dot{x}_2^2), \tag{3.50}$$

where x_1 and x_2 are the positions of the actuators and $m_{pzt,1}$ and $m_{pzt,2}$ are the equivalent linear inertia of the actuator in the actuator coordinate systems. The positions of the actuators, x_j are related to the fourbar output angles θ_j by the inverse transmission ratio T_{inv}. In other words:

$$x_j = T_{inv}(\theta_j), \quad j = 1, 2 \tag{3.51}$$

Substituting this into (3.1) gives:

$$\left(\frac{d}{dt}\left(\frac{\partial}{\partial \dot{q}}\right) - \frac{\partial}{\partial q}\right) KE_{\text{actuators}} = \begin{bmatrix} m_{act,1}(\theta_1) + m_{act,2}(\theta_2) & m_{act,1}(\theta_1) \\ m_{act,1}(\theta_1) & m_{act,1}(\theta_1) \end{bmatrix} \begin{bmatrix} \ddot{\theta}_2 \\ \ddot{\alpha} \end{bmatrix},$$

where $m_{act,j}$ are the equivalent inertias of the actuators in the fourbar output coordinate system and are related to $m_{pzt,j}$ as

$$m_{act,i} = \left(T_{inv}(\theta_i)\right)^2 m_{pzt,i} \tag{3.52}$$

To get an idea of what m_{act} is for a typical actuator, we get $m_{pzt} = 12$ mg for an actuator with a linear stiffness of 500N/m and a resonant frequency of about 1000Hz. From this, we get $m_{act} = 1.4$ mg-mm^2 for a fourbar transmission ratio T_{inv}^{-1} of 3000 rad/m. Note that m_{act} will actually vary with θ since T_{inv} varies with θ.

3.3.2 Kinetic Energy of the Slider Crank and Fourbar

The kinetic energy of a fourbar mechanism is given by:

$$KE_{fb}(\theta, \dot{\theta}) = \frac{1}{2} \sum_{i=1}^{i=3} m_{l,i} \dot{x}_{cg,i}^2, \tag{3.53}$$

where $m_{l,i}$ is the mass of the i^{th} link of the fourbar mechanism and $\dot{x}_{cg,i}$ is the velocity of the CG of the i^{th} link, which depends both on θ and $\dot{\theta}$ as:

$$\dot{x}_{cg,i} = \frac{\partial x_{cg,i}(\theta)}{\partial \theta} \dot{\theta} \tag{3.54}$$

We can calculate $x_{cg,i}$, the position of the CG of the i^{th} link using the kinematic solutions (2.8), (2.9) and (2.14). For our analysis, we make the following assumptions:

1. The slider crank is assumed to be a part of the fourbar input link for purposes of calculating the inertia. This is a very safe assumption to make since the slider crank contributes almost nothing to the overall inertia.

2. Links $\boxed{3}$ and $\boxed{4}$ of the differential (Fig. 2.8) are assumed to make up the output link of the top fourbar, while link $\boxed{1}$ is assumed to make up the output link of the bottom fourbar. This makes the inertias of the two fourbars slightly unequal.

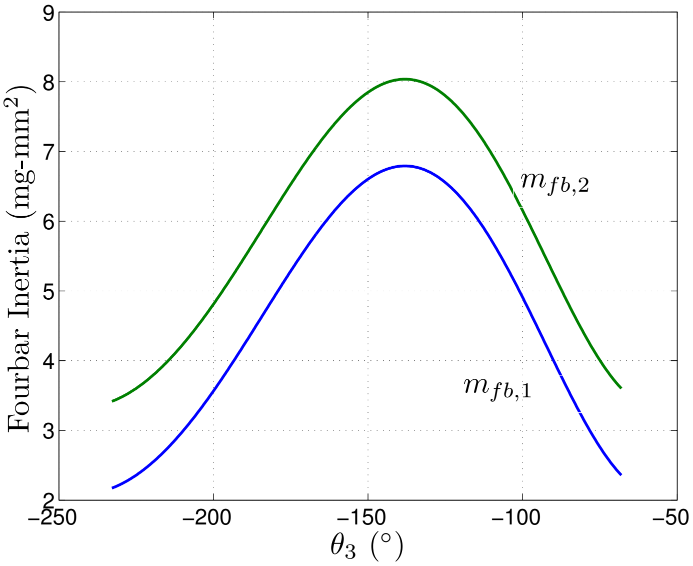

Figure 3.10: Fourbar Inertia components

Finally, the contribution of the fourbar KE to the overall dynamics can be derived as:

$$\left(\frac{d}{dt}\left(\frac{\partial}{\partial \dot{q}}\right) - \frac{\partial}{\partial q}\right) KE_{\text{four-bars}} = \begin{bmatrix} m_{fb,1}(\theta_1) + m_{fb,2}(\theta_2) & m_{fb,1}(\theta_1) \\ m_{fb,1}(\theta_1) & m_{fb,1}(\theta_1) \end{bmatrix} \begin{bmatrix} \ddot{\theta}_2 \\ \ddot{\alpha} \end{bmatrix},$$

where the equivalent fourbar inertias in the wing hinge coordinates are given by:

$$m_{fb}(\theta) = \sum_{i=1}^{i=3} m_{l,i} \left(\frac{\partial x_{cg,i}}{\partial \theta}\right)^2 \tag{3.55}$$

The variation of the fourbar inertia with fourbar output angle for the latest MFI fourbar model is given in Fig. 3.10. The asymmetry in the fourbar inertias is due to the inertia of links $\boxed{3}$ and $\boxed{4}$ of the differential being considered part of the top fourbar ($m_{fb,2}$), while only the inertia of link $\boxed{1}$ of the differential is considered part of the bottom fourbar ($m_{fb,1}$).

3.3.3 Kinetic Energy of the Wing

Note that for purposes of calculating the inertia, the total kinetic energy of the wing is calculated as:

$$KE_{\text{wing-diff}} = KE_{\text{wing}} + KE_{\text{diff},3} + KE_{\text{match}}, \tag{3.56}$$

where KE_{wing} is the KE of the wing itself. $KE_{\text{diff},3}$ is the inertia of link $\boxed{3}$ of the differential (Fig. 2.8) and KE_{match} is the inertia of the matching spar. The analysis for incorporating the wing inertia into the overall dynamics has been done in [Avadhanula 01] and is given as:

$$\left(\frac{d}{dt}\left(\frac{\partial}{\partial q}\right) - \frac{\partial}{\partial q}\right) KE_{\text{wing-diff}} = \begin{bmatrix} m_{w,1} & m_{w,12} \\ m_{w,12} & m_{w,2} \end{bmatrix} \begin{bmatrix} \ddot{\theta}_2 \\ \ddot{\alpha} \end{bmatrix} + \begin{bmatrix} 0 \\ 1/2 m'_{w,2} \dot{\alpha}^2 \end{bmatrix} \tag{3.57}$$

where

$$\begin{bmatrix} m_{w,1} \\ m_{w,2} \\ m_{w,12} \end{bmatrix} = \begin{bmatrix} c^2_{\theta_y} & 1 - c^2_{\theta_x} \cdot c^2_{\theta_y} & -s_{2\theta_y} c_{\theta_x} \\ \theta'^2_y & \theta'^2_y c^2_{\theta_x} + \theta'^2_x & -2\theta'_y \theta'_x s_{\theta_x} \\ 0 & \theta'_y s_{\theta_x} c_{\theta_y} - \theta'_x s_{\theta_y} & \theta'_x c_{\theta_y} c_{\theta_x} + \theta'_y s_{\theta_y} s_{\theta_x} \end{bmatrix} \begin{bmatrix} J_{xx} \\ J_{zz} \\ J_{xz} \end{bmatrix} \tag{3.58}$$

where θ_x and θ_y are the angles shown in Fig. 2.8 and c_γ and s_γ are short forms for $\cos\gamma$ and $\sin\gamma$ respectively. J_{xx}, J_{xz} and J_{zz} are the components of the inertia distribution of the wing in the wing local coordinate system. If we assume that the wing (along with link $\boxed{3}$ of the differential and the matching spar lie in the $X - Z$ plane in the configuration shown in Fig. 2.8), then these components are found as:

$$\begin{bmatrix} J_{xx} & J_{xz} \\ J_{xz} & J_{zz} \end{bmatrix} = \int_W \rho \begin{bmatrix} x_w \\ z_w \end{bmatrix} \begin{bmatrix} x_w \\ z_w \end{bmatrix}^T dx_w dz_w \tag{3.59}$$

For the latest MFI differential, these inertia terms vary with θ_x, the wing rotation as shown in Fig. 3.11

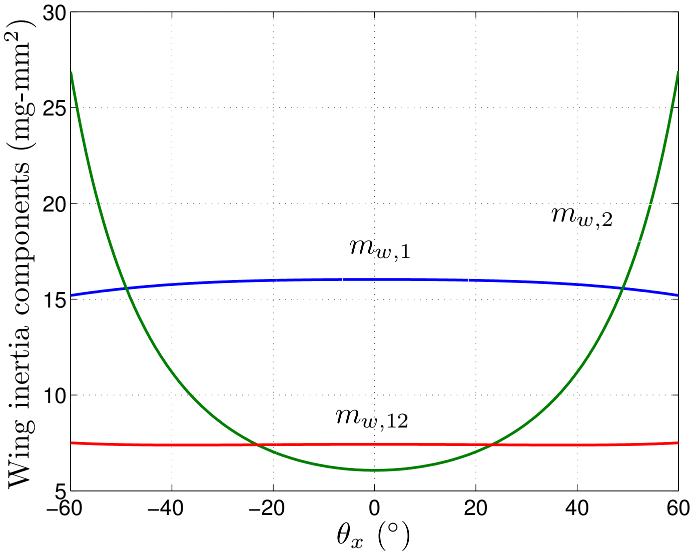

Figure 3.11: Wing inertia components

3.3.4 Potential Energy of the Actuator

The stiffness of the actuator in the linear actuator coordinates is assumed to be constant. This gives the PE of the actuator as:

$$PE_{act} = \frac{1}{2}K_{pzt}(x - x_p)^2 \tag{3.60}$$

where K_{pzt} is the linear stiffness of the actuator and x is the linear displacement of the actuator in the actuator coordinates, which is related to the fourbar output angle θ via T_{inv} the inverse fourbar transmission ratio. x_p represents the “placement” of the actuator relative to the fourbar. Recall from the kinematics of the fourbar and slider crank that T_{inv} is defined such that

$$T_{inv}(\theta_3 = \pi/2) = 0 \tag{3.61}$$

Since $\theta_3 = \pi/2$ corresponds to the fourbar position for which the fourbar flexures are all stress free, this corresponds to saying that we define the *kinematic zero position* of the actuator as the minimum PE position of the fourbar. x_p accounts for the fact that we can (and do) place the actuator in such a way that the resultant total PE minimum is at a different θ_3 than for the fourbar minimum PE.

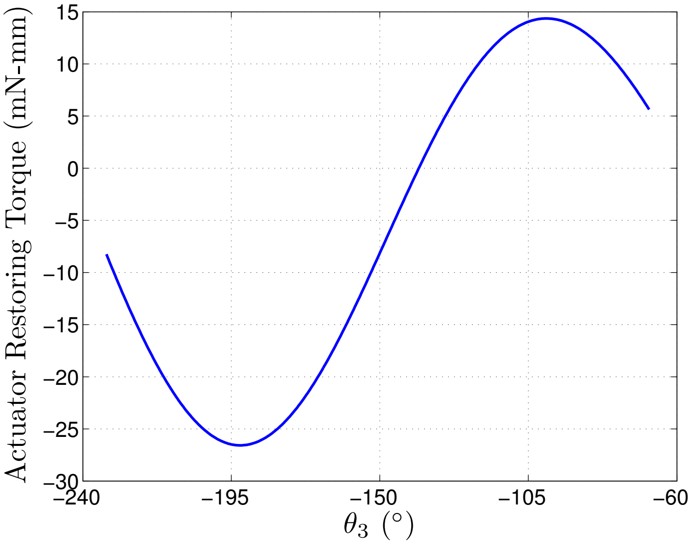

Figure 3.12: Variation of Actuator torque with fourbar output angle for $x_p = 0$.

From this we can calculate the contribution to the overall dynamics as:

$$\frac{\partial PE_{\text{act}}}{\partial q} = \begin{bmatrix} F_{\text{act,1}}(\theta_1) + F_{\text{act,2}}(\theta_2) \\ F_{\text{act,1}}(\theta_2) \end{bmatrix} \tag{3.62}$$

where $F_{\text{act,i}}$ is the restoring torque produced by the i^{th} actuator in the wing hinge coordinate system:

$$\begin{aligned} F_{\text{act}}(\theta) &= \frac{\partial PE_{act}}{\partial \theta} \\ &= K_{pzt}(T_{inv}(\theta) - x_p)\frac{T_{inv}(\theta)}{\partial \theta} \end{aligned} \tag{3.63}$$

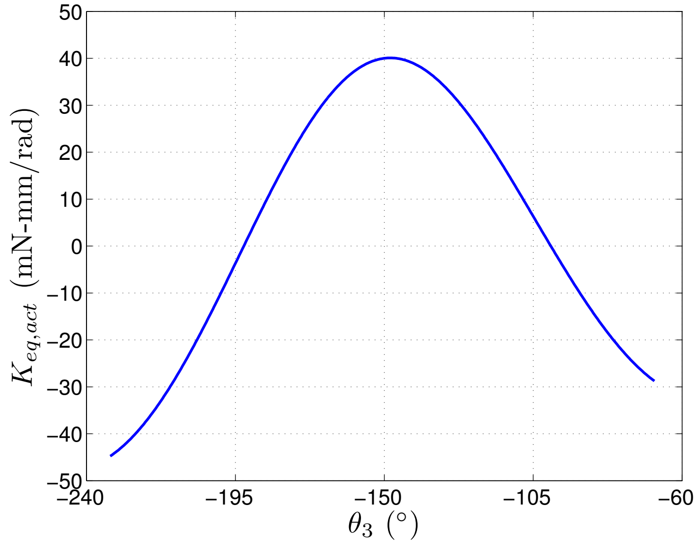

Figure 3.13: Nominal actuator stiffness for small motions

The variation of F_{act} with respect to the fourbar output angle is given in Fig. 3.12 The following two important points about this variation should be emphasized:

1. The actuator restoring torque is *not* symmetric about the zero torque angle if we place the actuator such that it is stress-free when the fourbar flexures are stress-free.

2. The actuator restoring actually changes direction for large enough fourbar angles. In other words, the nominal actuator stiffness actually becomes negative as shown in Fig. 3.13. This extremely non-intuitive result arises from the extreme non-linearity in the fourbar transmission. As we will see later, this is the most important reason for the "jump resonant" behavior of fourbars.

3.3.5 Potential Energy of the Slider Crank and Fourbar

The PE stored in the fourbar and slider crank flexures is given by:

$$PE_{\text{slider-crank}} = \frac{1}{2}\sum_{i=1}^{2} k_{sc,i}\theta_{sc,i}^2 \tag{3.64}$$

$$PE_{\text{fourbar}} = \frac{1}{2}\sum_{i=1}^{i=4} k_{fb,i}\theta_{fb,i}^2 \tag{3.65}$$

where $\theta_{fb,i}$ is the angle which the i^{th} fourbar flexure bends through (from its stress-free position). $k_{fb,i}$ is the rotational stiffness of the i^{th} fourbar flexure. We assume that the flexures behave as perfect rotary joints with added rotational springs. The rotational stiffness can be calculated as:

$$k_{fb,i} = \frac{Ew_i t_i^3}{12 l_i} \tag{3.66}$$

where E is the flexural modulus of the flexure material, w_i is the width of the flexure, t_i is the thickness and l_i is the length of the flexure.

From this we can find the contribution to the overall dynamics as:

$$\frac{\partial PE_{\text{fourbars}}}{\theta q} = \begin{bmatrix} F_{fb,1}(\theta_1) + F_{fb,2}(\theta_2) \\ F_{fb,1}(\theta_1) \end{bmatrix} \tag{3.67}$$

$$\frac{\partial PE_{\text{slider-cranks}}}{\theta q} = \begin{bmatrix} F_{sc,1}(\theta_1) + F_{sc,2}(\theta_2) \\ F_{sc,1}(\theta_1) \end{bmatrix} \tag{3.68}$$

where:

$$F_{fb}(\theta) = \sum_{i=1}^{4} k_{fb}\theta_{fb,i}\frac{\partial \theta_{fb,i}}{\partial \theta} \tag{3.69}$$

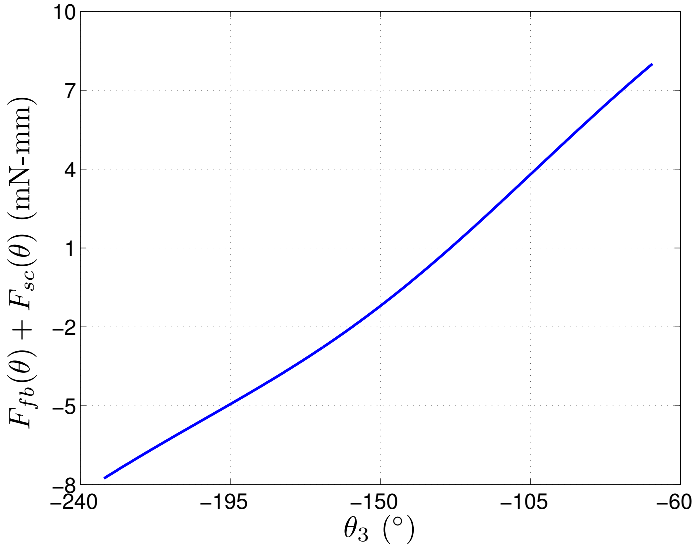

Figure 3.14: Restoring torque by fourbar and slider crank on wing hinge

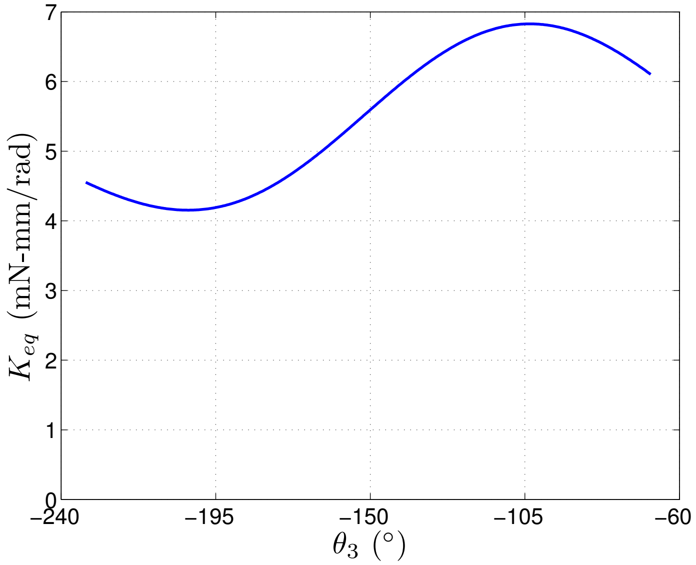

Figure 3.15: Small motion equivalent stiffness of the fourbar and slider crank

The variation of $(F_{fb}+F_{sc})(\theta)$ with respect to θ, the fourbar output angle is shown in Fig. 3.14. We can also find the equivalent stiffness of the fourbar and slider crank for small motions about a given position. This is found as:

$$K_{eq} = \frac{\partial}{\partial\theta}(F_{fb}(\theta) + F_{sc}(\theta)) \tag{3.70}$$

Note that this stiffness is only valid for sufficiently small motions around the given output angle. For larger angles, it no longer makes sense to talk of a stiffness. The variation of K_{eq} versus θ is shown in Fig. 3.15.

3.3.6 Potential Energy of the Differential

The potential energy stored in the differential flexures is given by:

$$PE_{\text{differential}} = \frac{1}{2}(k_x(\theta_x + \theta_x^0)^2 + k_y(\theta_y + \theta_y^0)^2 + k_w(\theta_w + \theta_w^0)^2) \tag{3.71}$$

where k_x is the rotational stiffness of the flexure corresponding to the θ_x axis (see Fig. 2.8) and similarly for k_y and k_w. Since we assume that these flexures behave as ideal rotational joints with a constant rotational stiffness, we can calculate k_x (and similarly k_y and k_w) as:

$$k_x = \frac{E w_x^2 t_x^3}{12 l_x} \tag{3.72}$$

where w_x, t_x and l_x are the width, thickness and the length of the θ_x flexure and E is the Young's modulus of the flexure material.

θ_x^0 is the angle made by the θ_x flexure with respect to the stress-free position when $\theta_x = 0$. This is to account for pre-bends which the fabrication process subjects on the flexures. In our case, the fabrication process makes:

$$\theta_x^0 = \frac{\pi}{2} \tag{3.73}$$

$$\theta_y^0 = 0 \tag{3.74}$$

$$\theta_w^0 = -\frac{\pi}{2} \tag{3.75}$$

Using these equations, we can find the contribution of the differential PE to the total dynamics as:

$$\frac{\partial}{\partial q} PE_{\text{differential}} = \begin{bmatrix} 0 \\ F_{\text{diff}}(\alpha) \end{bmatrix} \tag{3.76}$$

where $F_{\text{diff}}(\alpha)$ is the restoring torque produced by the differential to resist the difference in the fourbar output angles. It is given by:

$$F_{\text{diff}}(\alpha) = \sum_{\nu=x,y,w} k_\nu(\theta_\nu + \theta_\nu^0)\frac{\partial \theta_\nu}{\partial \alpha} \tag{3.77}$$

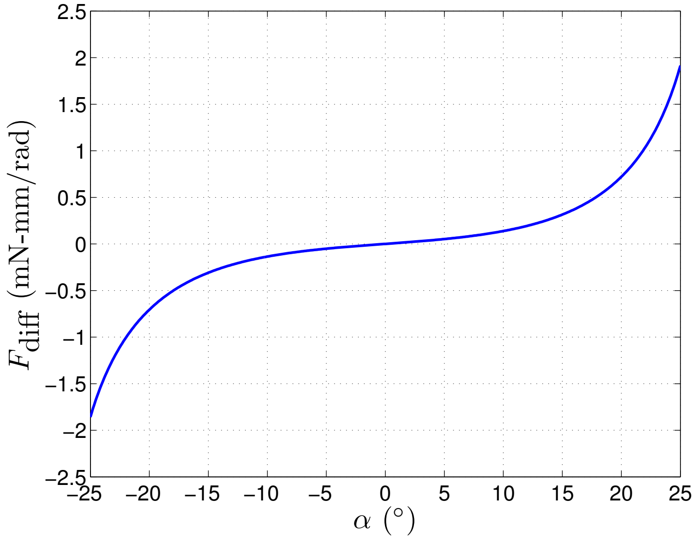

Figure 3.16: F_{diff} vs. α

The variation of F_{diff} with α is shown in Fig. 3.16. As can be seen, the restoring torque is highly non-linear. This is apparent if we calculate the nominal differential stiffness vs α. This is given by:

$$K_{\text{diff}}(\alpha) = \frac{\partial}{\partial \alpha} PE_{\text{diff}} \tag{3.78}$$

This stiffness is of course only valid for very small rotations. The variation of K_{diff} is shown in Fig. 3.17.

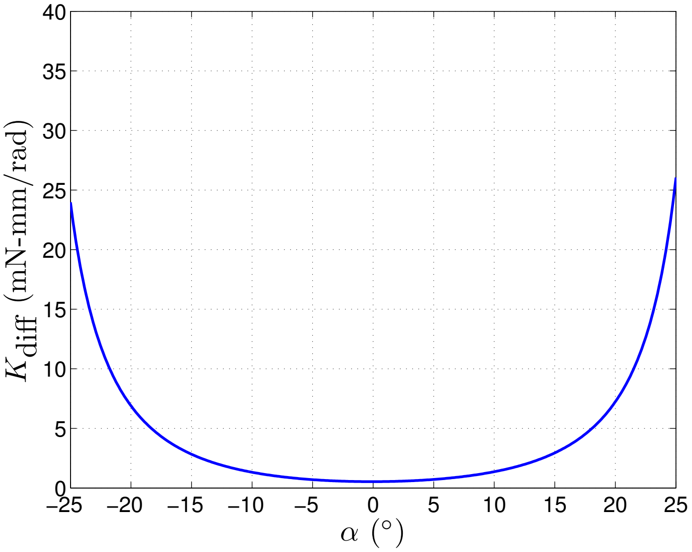

Figure 3.17: Variation of differential stiffness with α.

It can be seen that the nominal differential stiffness varies from a minimum of just 0.5mN-mm/rad (when $\alpha = 0$) to a maximum of 35mN-mm/rad (when $\alpha = 26°$), a change of almost two orders of magnitude. $\alpha = 26°$ corresponds to a rotation angle $\theta_x = \frac{\pi}{3}$ for a differential transmission ratio $\lambda = 2$. Although this seems to imply that it is extremely hard to get large rotations from the differential, in practice as well as simulations it is very easy to get large rotations from the differential (sometimes so large that the differential is damaged). This is because although the stiffness with respect to α is very high (equivalent to a spring with a stiffness of 315 N/m connected between the actuators in the actuator reference frame), when we consider the stiffness with respect to the rotation angle θ_x, it is actually quite low. The equivalent stiffness with respect to θ_x can be found simply as:

$$\hat{K}_{\text{diff}}(\theta_x) = \frac{\partial^2}{\partial \theta_x^2} PE_{\text{diff}}(\theta_x) \tag{3.79}$$

In other words, we need to write the potential energy stored in the differential flexures as a function of θ_x and then find its second derivative with respect to θ_x. This stiffness is shown in Fig. 3.18:

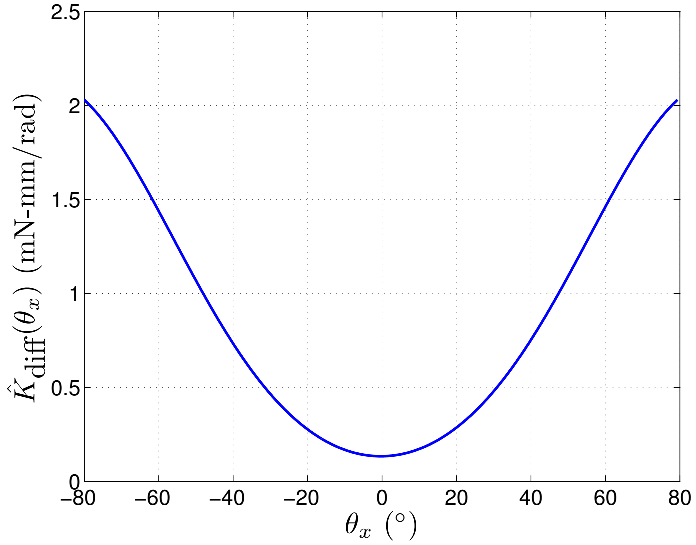

Figure 3.18: Variation of differential stiffness as a function of rotation angle

As can be seen, the stiffness in this reference frame is only 1.5 mN-mm/rad at $\theta_x = \frac{\pi}{3}$, which corresponds to just 13 N/m in the actuator coordinate system.

3.3.7 Internal Actuator and Fourbar Damping

The internal damping forces in the actuator and the fourbars need to be modeled as time varying external force in order to incorporate them into the Euler-Lagrange formulation. We assume that the work done by these damping forces is of the form:

$$dW_{\mathrm{damp}} = F_{\mathrm{damp}}(\dot{\theta}_1)d\theta_1 + F_{\mathrm{damp}}(\dot{\theta}_2)d\theta_2 \tag{3.80}$$

where F_{damp} is assumed to be of the form:

$$F_{\mathrm{damp}}(\dot{\theta}) = B\dot{\theta}, \tag{3.81}$$

where B is a constant. In other words, we assume that the actuator and fourbar damping can be treated as a linear damping force (with a constant damping coefficient) which acts directly on the wing hinge output. Note that recent research has shown that the actuator model is much more complicated and in particular, its internal damping might also be stress and velocity dependent. We ignore this effect for now with the caveat that this might in fact be an important effect for further study. With this assumption, the contribution of the fourbar and actuator damping becomes:

$$\frac{\partial}{\partial q}W_{\mathrm{damp}} = \begin{bmatrix} B_1\dot{\theta}_1 + B_2\dot{\theta}_2 \\ B_1\dot{\theta}_1 \end{bmatrix} \tag{3.82}$$

3.3.8 Work done by Actuators

The work done by the MFI actuators is given by:

$$dW_{act} = F_{act}dx \tag{3.83}$$

where dx is the differential motion of the actuator in the actuator coordinates. This is related to the fourbar output angle by:

$$dx = T'_{inv}(\theta)d\theta \tag{3.84}$$

Thus, we have:

$$dW_{act} = F_{act}T'_{inv}(\theta)d\theta \tag{3.85}$$

F_{act} is the linear force generated by the actuator. For the moment, we assume that this varies linearly with the applied voltage to the actuator.

From this, we can write the contribution of the actuator forces to the overall dynamics as:

$$\frac{dW_{act}}{dq} = \begin{bmatrix} T'_{inv}(\theta_1) + T'_{inv}(\theta_2) \\ T'_{inv}(\theta_1) \end{bmatrix} \begin{bmatrix} F_{act,1} \\ F_{act,2} \end{bmatrix} \tag{3.86}$$

3.4 Complete Dynamic model

With the contributions of the various structural components of the MFI and the aerodynamics derived in the previous sections, we can put these together to write down the complete differential equation which governs the motion of the MFI thorax.

$$\mathbf{M}\begin{bmatrix} \ddot{\theta}_2 \\ \ddot{\alpha} \end{bmatrix} + \mathbf{F}_{\text{damp}} + \mathbf{F}_{\text{aero}} + \mathbf{F}_{\text{stiff}} + \begin{bmatrix} 0 \\ \frac{1}{2}m'_{w,2}\dot{\alpha}^2 \end{bmatrix} = \mathbf{T}_{in}\begin{bmatrix} F_{act,1} \\ F_{act,2} \end{bmatrix}, \tag{3.87}$$

where

$$\mathbf{M} = \begin{bmatrix} \begin{pmatrix} m_{fb,1}(\theta_2 + \alpha) + m_{fb,2}(\theta_2) \\ + m_{act,1}(\theta_2 + \alpha) + m_{act,2}(\theta_2) \\ + m_{w,1} \end{pmatrix} & \begin{pmatrix} m_{fb,1}(\theta_2 + \alpha) \\ + m_{act,1}(\theta_2 + \alpha) \\ + m_{w,12} \end{pmatrix} \\ \\ \begin{pmatrix} m_{fb,1}(\theta_2 + \alpha) \\ + m_{act,1}(\theta_2 + \alpha) \\ + m_{w,12} \end{pmatrix} & \begin{pmatrix} m_{fb,1}(\theta_2 + \alpha) \\ + m_{act,1}(\theta_2 + \alpha) \\ + m_{w,2} \end{pmatrix} \end{bmatrix} \tag{3.88}$$

$$\mathbf{F}_{\text{damp}} = \begin{bmatrix} B_1\dot{\theta}_1 + B_2\dot{\theta}_2 \\ B_1\dot{\theta}_1 \end{bmatrix} \tag{3.89}$$

$$\mathbf{F}_{\text{aero}} = \begin{bmatrix} r_1(\alpha) \\ r_2(\alpha) \end{bmatrix} F_{aero}(\alpha, \dot{\alpha}, \dot{\theta}_2) \tag{3.90}$$

$$\mathbf{F}_{\text{stiff}} = \begin{bmatrix} F_{act,1}(\theta_1) + F_{act,2}(\theta_2) + F_{fb,1}(\theta_1) + F_{fb,2}(\theta_2) \\ F_{act,1}(\theta_1) + F_{fb,1}(\theta_1) + F_{diff}(\alpha) \end{bmatrix} \tag{3.91}$$

$$\mathbf{T}_{in} = \begin{bmatrix} T'_{inv}(\theta_1) & T'_{inv}(\theta_2) \\ T'_{inv}(\theta_1) & 0 \end{bmatrix} \tag{3.92}$$

3.5 Matching Spar Design

In this section, we describe the “dynamically tuned” design aspect of the MFI thorax. As described previously in [Avadhanula 01], the mechanical design of the MFI is tuned in a way to give optimal dynamical performance.

3.5.1 Linearized System Dynamics

If we linearize the system described in (3.87) for small motions around $\theta_2 = -135°$ (the minimum PE position of the fourbar flexures) and $\alpha = 0°$ (the nominally flat position of the differential), we get a linear system of the form:

$$\mathbf{M}_{lin} \begin{bmatrix} \ddot{\theta}_2 \\ \ddot{\alpha} \end{bmatrix} + \mathbf{B}_{lin} \begin{bmatrix} \dot{\theta}_2 \\ \dot{\alpha} \end{bmatrix} + \mathbf{K}_{lin} \begin{bmatrix} \theta_2 \\ \alpha \end{bmatrix} = \mathbf{T}_{\mathbf{i,lin}} \begin{bmatrix} F_1 \\ F_2 \end{bmatrix} \tag{3.93}$$

where the linearized system matrices are given by:

$$\mathbf{M}_{lin} = \begin{bmatrix} m_1 & m_{12} \\ m_{12} & m_2 \end{bmatrix} \tag{3.94}$$

$$\mathbf{B}_{lin} = \begin{bmatrix} 2B & B \\ B & B \end{bmatrix} \tag{3.95}$$

$$\mathbf{K}_{lin} = \begin{bmatrix} 2K_{tot} & K_{tot} \\ K_{tot} & K_{tot} + K_{diff} \end{bmatrix} \tag{3.96}$$

$$\mathbf{T}_{in,lin} = T_{inv} \begin{bmatrix} 1 & 1 \\ 1 & 0 \end{bmatrix} \tag{3.97}$$

where

$$m_1 = m_{act,1} + m_{fb,1} + m_{act,2} + m_{fb,2} + m_{w,1} \tag{3.98}$$

$$m_{12} = m_{act,1} + m_{fb,1} + m_{w,12} \tag{3.99}$$

$$m_2 = m_{act,1} + m_{fb,1} + m_{w,2} \tag{3.100}$$

$$K_{tot} = k_{act,1} + k_{fb,1} \tag{3.101}$$

$$B = B_1 \tag{3.102}$$

Note that we have made the (reasonable) assumption that $k_{act,1} = k_{act,2}$, $k_{fb,1} = k_{fb,2}$ and $B_1 = B_2$. By using the transformation:

$$\begin{bmatrix} \theta_2 \\ \alpha \end{bmatrix} = \begin{bmatrix} 0 & 1 \\ 1 & -1 \end{bmatrix} \begin{bmatrix} \theta_1 \\ \theta_2 \end{bmatrix} \tag{3.103}$$

we can transform (3.93) to get the dynamic equation relating $\{F_1, F_2\}^T$ (the two actuator force inputs) to $\{\theta_1, \theta_2\}$ (the two fourbar output angles):

$$\begin{bmatrix} M_{11} & M_{12} \\ M_{12} & M_{22} \end{bmatrix} \begin{bmatrix} \ddot{\theta}_1 \\ \ddot{\theta}_2 \end{bmatrix} + \begin{bmatrix} B & 0 \\ 0 & B \end{bmatrix} \begin{bmatrix} \dot{\theta}_1 \\ \dot{\theta}_2 \end{bmatrix} + \begin{bmatrix} K_{tot} + K_{diff} & -K_{diff} \\ -K_{diff} & K_{tot} + K_{diff} \end{bmatrix} \begin{bmatrix} \theta_1 \\ \theta_2 \end{bmatrix} = \begin{bmatrix} F_1 \\ F_2 \end{bmatrix} \tag{3.104}$$

where:

$$M_{11} = m_2 \tag{3.105}$$

$$M_{12} = m_{12} - m_2 \tag{3.106}$$

$$M_{22} = m_{11} - 2m_{12} + m_2 \tag{3.107}$$

We can further convert this dynamic description into a 2 input 2 output transfer function form:

$$\begin{bmatrix} \Theta_1(s) \\ \Theta_2(s) \end{bmatrix} = \begin{bmatrix} G_{11}(s) & G_{12}(s) \\ G_{12}(s) & G_{22}(s) \end{bmatrix} \begin{bmatrix} F_1(s) \\ F_2(s) \end{bmatrix} \tag{3.108}$$

3.5.2 Inertial Matching Condition

In the method of "dynamic tuning" described in [Avadhanula 01], we designed the mechanism such that the following conditions are met:

1. There is minimal coupling at DC, i.e. $G_{12}(s \rightarrow 0) = 0$.
2. The dynamics along the diagonal are identical, i.e., $G_{11}(s) = G_{22}(s)$

These conditions require the following criteria about the system parameters to be met:

1. The differential stiffness is very small $K_{diff} \ll K_{tot}$.
2. The wing inertia is distributed in a way that enforces $m_{w,2} = m_{w,12} = 0.5m_{w,1}$. This was accomplished by choosing the wing placement relative to the differential.

This method has a few drawbacks:

1. The condition $K_{diff} \ll K_{tot}$ implies that we need to make the differential flexures very thin. This has the very undesirable effect of creating undesirable vibration modes in the differential. Making flexures thinner also makes the differential more fragile and hence reduces lifetime.

2. Choosing the wing placement with respect to the differential is error-prone and it also only approximately meets the condition that $m_{w,12} = m_{w,2} = 0.5m_{w,1}$ because we are trying to achieve two independent constraints with a single variable. Moreover, placing the wing at an offset with respect to the differential creates a somewhat weaker joint between the differential and the wing.

3. That method also does not account for slight differences in the inertias of the two fourbars (since the differential halves attached to the fourbars are not identical).

4. Moreover, the design aim which we set that there is minimal DC coupling $G_{12}(s \leftarrow 0) = 0$ is not so directly useful because we finally want to drive the two fourbars at their resonance. A more direct aim of the design should be to reduce the coupling between the fourbars at the common resonant frequency.

All these drawbacks inspired an improved dynamic tuning method which relies on what is called a "matching spar". In this method, the following design aims are to be met:

1. The dynamics along the diagonal are identical, i.e, $G_{11}(s) = G_{22}(s)$.

2. The cross-coupling dynamics are reduced at the resonant frequency of the fourbars. In other words,

$$\omega_r = \arg\max_{\omega} |G_{11}(j\omega)| \implies \omega_r = \arg\min_{\omega} |G_{12}(j\omega)| \tag{3.109}$$

In this method, we place a small low inertia "matching spar", which is a small bar of carbon fiber on the differential along with the wing. This changes the total inertia of the differential, or the $m_{w,1}$, $m_{w,12}$ and $m_{w,2}$ terms in (3.104). This changes the transfer function (3.108) in such a manner that the two conditions above will be met.

We proceed by finding the transfer function corresponding to (3.104). This is done by simply taking the Laplace transform of both sides:

$$\begin{bmatrix} M_{11}s^2 + Bs + (K_{tot} + K_{diff}) & M_{12}s^2 - K_{diff} \\ M_{12}s^2 - K_{diff} & M_{22}s^2 + Bs + (K_{tot} + K_{diff}) \end{bmatrix} \begin{bmatrix} \Theta_1(s) \\ \Theta_2(s) \end{bmatrix} = \begin{bmatrix} F_1(s) \\ F_2(s) \end{bmatrix} \tag{3.110}$$

Solving for $\Theta_i(s)$ gives:

$$\begin{bmatrix} \Theta_1(s) \\ \Theta_2(s) \end{bmatrix} = \frac{1}{D(s)} \begin{bmatrix} M_{22}s^2 + Bs + (K_{tot} + K_{diff}) & -(M_{12}s^2 - K_{diff}) \\ -(M_{12}s^2 - K_{diff}) & M_{11}s^2 + Bs + (K_{tot} + K_{diff}) \end{bmatrix} \begin{bmatrix} F_1(s) \\ F_2(s) \end{bmatrix} \tag{3.111}$$

where

$$\begin{aligned} D(s) = {} & (M_{11}s^2 + Bs + (K_{tot} + K_{diff}))(M_{22}s^2 + Bs + (K_{tot} + K_{diff})) \\ & - (M_{12}s^2 - K_{diff})^2 \end{aligned} \tag{3.112}$$

In order to satisfy the first condition $G_{11}(s) = G_{22}(s)$, we require the following condition to be met:

$$\begin{aligned} & M_{11} = M_{22} \\ \Longrightarrow {} & m_2 = m_1 - 2m_{12} + m_2 \\ \Longrightarrow {} & m_{12} = \frac{1}{2}m_1 \end{aligned} \tag{3.113}$$

In order to satisfy (3.109), we need to find out the resonant frequency of the diagonal elements of the transfer function matrix. The two resonant frequencies are given by the roots of $D(s)$. With the assumption that $M_{11} = M_{22}$, we can write down $D(s)$ as:

$$\begin{aligned} D(s) &= (M_{11}s^2 + Bs + K_{tot} + K_{diff})^2 - (M_{12}s^2 - K_{diff})^2 \quad (3.114) \\ &= (M_{11}s^2 + Bs + K_{tot} + K_{diff} + M_{12}s^2 - K_{diff}) \\ &\qquad (M_{11}s^2 + Bs + K_{tot} + K_{diff} - M_{12}s^2 + K_{diff}) \quad (3.115) \\ &= ((M_{11} + M_{12})s^2 + Bs + K_{tot})((M_{11} - M_{12})s^2 + Bs + K_{tot} + 2K_{diff}) \\ &\qquad (3.116) \end{aligned}$$

For the two resonant frequencies to be identical, we require

$$\frac{M_{11} + M_{12}}{K_{tot}} = \frac{M_{11} - M_{12}}{K_{tot} + 2K_{diff}} \tag{3.117}$$

Substituting M_{11} and M_{12} from (3.105) and (3.106), we can reduce this condition to the following condition on m_1 and m_2:

$$m_2 = \frac{K_{tot} + K_{diff}}{2K_{tot}} m_1 \tag{3.118}$$

Note that (3.113) and (3.118) guarantee that there is a single resonant frequency for the linearized transfer function and that $G_{11}(s) = G_{22}(s)$. We will show that these conditions automatically guarantee (3.109). Notice that the resonant frequency of the system is given by:

$$\begin{aligned} \omega_r &= \arg\max_{\omega} |G_{11}(j\omega)| \\ &= \sqrt{\frac{K_{tot}}{M_{11} + M_{12}}} \end{aligned} \tag{3.119}$$

Substituing this in the expression for $G_{12}(s)$ gives:

$$G_{12}(j\omega_r) = M_{12}\omega_r^2 + K_{diff} = \frac{M_{12}K_{tot}}{M_{11} + M_{12}} \tag{3.120}$$

If we use (3.117), we can easily see that

$$\frac{M_{12}}{M_{11}+M_{12}} = -\frac{K_{diff}}{K_{tot}} \tag{3.121}$$

which when substituted back into (3.120) gives:

$$G_{12}(j\omega_r) = 0 \tag{3.122}$$

Thus we have shown the following:

Inertia Matching

If the wing inertia components $m_{w,1}$, $m_{w,12}$ and $m_{w,2}$ are chosen in such a manner that the following two conditions are met:

$$\frac{m_{12}}{m_1} = \frac{1}{2} \tag{3.123}$$

$$\frac{m_2}{m_1} = \frac{K_{tot}+K_{diff}}{2K_{tot}} \tag{3.124}$$

then the following conditions are met for the performance of the nominally linearized system:

$$G_{11}(s) = G_{22}(s) \tag{3.125}$$

$$\arg\min_{\omega} G_{12}(j\omega) = \arg\max_{\omega} G_{11}(j\omega) \tag{3.126}$$

3.5.3 Matching Spar Design

Once the desired ratios m_2/m_1 and m_{12}/m_1 are found, we need to design a matching spar which will ensure that we do attain these desired ratios. Recall that we can write m_1, m_{12} and m_2 as:

$$m_1 = m_{act,1} + m_{act,2} + m_{fb,1} + m_{fb,2} + J_{xx,w} + J_{xx,d} + J_{xx,m} \tag{3.127}$$

$$m_2 = m_{act,1} + m_{fb,1} + \lambda^2(J_{zz,w} + J_{zz,d} + J_{zz,m}) \tag{3.128}$$

$$m_{12} = m_{act,1} + m_{fb,1} + \lambda(J_{xz,w} + J_{xz,d} + J_{xz,m}) \tag{3.129}$$

where J_{xx} and others are defined in (3.59). The problem now reduces to finding $J_{xx,m}$, $J_{zz,m}$ and $J_{xz,m}$ such that (3.118) and (3.113) are satisfied. Since we only need to satisfy two constraints and we have three design variables, we can arbitrarily fix one of these variables. Since we will want to minimize the total flapping inertia of the wing, we fix $J_{xx,m} = 2 \times 10^{-12}$mg-mm^2 (below which it will be hard to fabricate the matching spar) and calculate $J_{zz,m}$ and $J_{xz,m}$ such that the inertia matching conditions are met.

Once $J_{xx,m}$, $J_{zz,m}$ and $J_{xz,m}$ are calculated, it remains to calculate the shape and placement of the matching spar to get the desired inertia distribution. We choose the simplest possible shape for the matching spar, which is a rectangle cut out from 40μm carbon fiber. The design variables are the length, width and placement of the rectangle on the differential. This is shown in Fig. 3.19. In this figure, we design for l_m, w_m and z_{off} to get the desired inertia distribution. The inertia components in terms of these design variables are given by:

$$J_{xx,m} = \frac{4}{3}\rho_A l_m w_m^3 + 4\rho_A l_m w_m x_{off}^2 \tag{3.130}$$

$$J_{zz,m} = \frac{4}{3}\rho_A w l_m^3 + 4\rho_A l_m w_m z_{off}^2 \tag{3.131}$$

$$J_{xz,m} = 4\rho_A x_{off} z_{off} w_m l_m \tag{3.132}$$

These equations can be solved numerically to get the desired l_m, w_m and z_{off} for a given $J_{xx,m}$, $J_{zz,m}$ and $J_{xz,m}$.

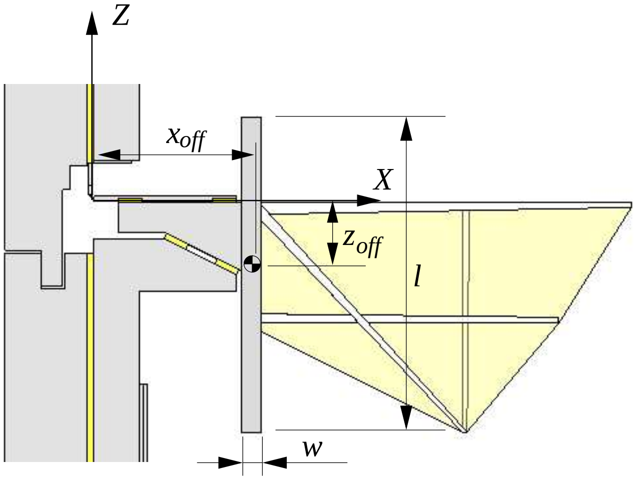

Figure 3.19: Placement of matching spar

3.5.4 Example

As a working example, we consider the mass, stiffness and damping parameters for the recent-most MFI design:

Parameter	Value	Units
$m_{fb,1} + m_{act,1}$	6.77	mg-mm^2
$m_{fb,2} + m_{act,2}$	8.02	mg-mm^2
K_{tot}	45	mN-mm/rad
K_{diff}	20	mN-mm/rad
x_{off}	3.5	mm

Table 3.1: Inertial and stiffness parameters in latest MFI

For these parameters, the final design of the matching spar is

Parameter	Value (mm)
l_m	13.23
w_m	0.18
z_{off}	1.84

Table 3.2: Latest matching spar parameters

With this matching spar, the nominal linearized transfer function is shown in Fig. 3.20. As can be seen, the two conditions are very neatly met.

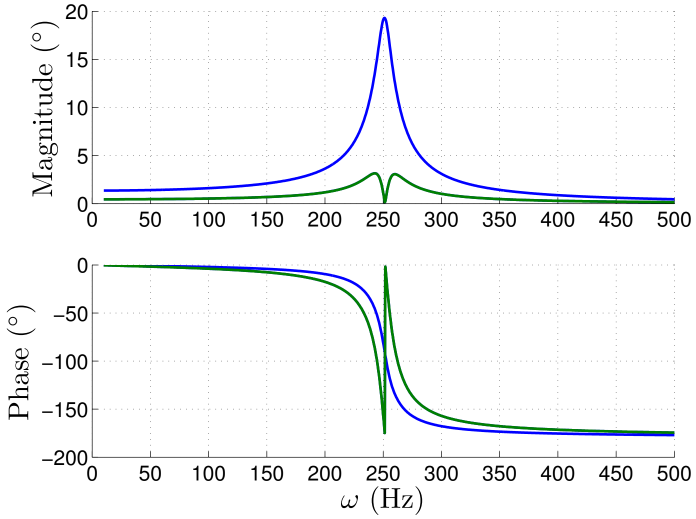

Figure 3.20: Dynamics with optimal matching spar design. Note that the Q is much higher than in reality because the linearized dynamics does not include the effect of wing damping which is the major source of damping in the structure. However, the general "shape" of the frequency response should be unaffected by the additional wing damping.

Fig. 3.21 shows the experimentally measured frequency response of $04 - \chi$, a 2 DOF structure. As can be seen, we see a single peak in the diagonal dynamics (i.e., from V_i to θ_i) and a low coupling in the off-diagonal terms (i.e., from V_1 to θ_2 and V_2 to θ_1). To see the improvement which the matching spar makes to the overall dynamics, we contrast this with the experimentally measured frequency sweep of a 2 DOF structure made in 2001, which is shown in Fig. 3.22. This structure shows a huge amount of coupling between the two actuators as shown in Fig. 3.22(b). Moreover, we see two frequency resonances due to inadequately designed inertia distribution.

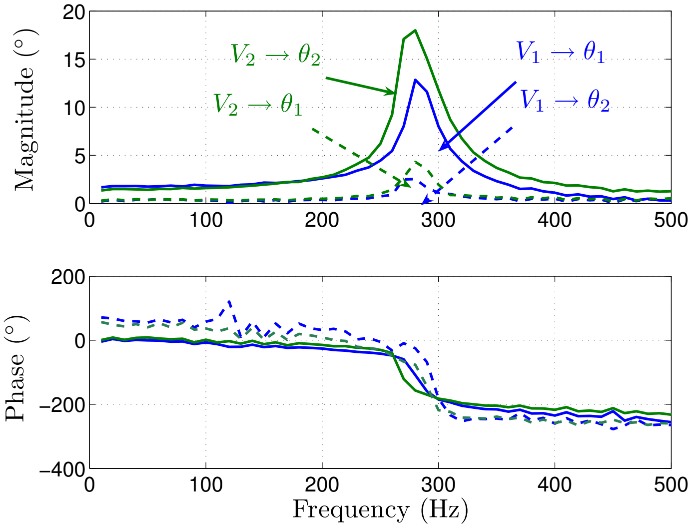

Figure 3.21: Experimentally measured frequency response of $04-\chi$, a 2DOF structure.

3.6 Summary

In this chapter, we modeled the complete dynamics of a 2 DOF structure including the aerodynamics of the MFI wing. We described a way to optimally design the MFI differential in order to obtained "tuned" dynamics. This design principle was validated with experimentally measured frequency responses.

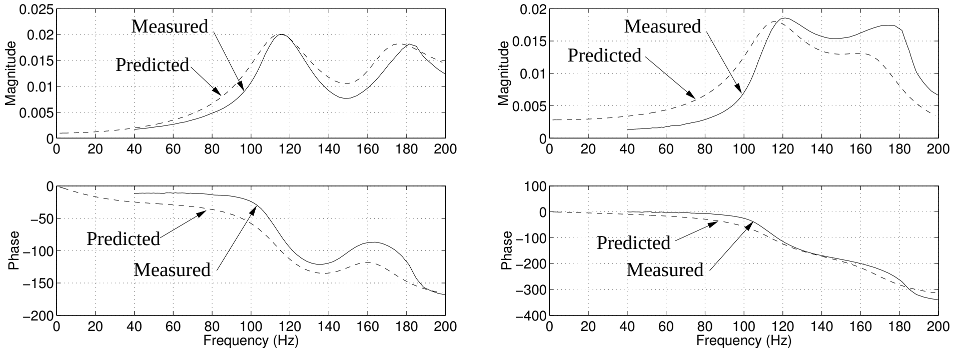

(a) $V_{i,1} \rightarrow V_{0,1}$ (b) $V_{i,2} \rightarrow V_{0,1}$

Figure 3.22: Comparison of predicted (dashed) and actual (solid) strain gage dynamics [Avadhanula 01]. Note that the units do not correspond to degrees of motion but to strain gage volts.

Chapter 4

Fourbar Dynamics and System Identification

The previous chapter described the over-all dynamic behavior of the MFI thorax including the aerodynamic model described in [Dickinson 99]. Since the derived model contains significant non-linearities, it is important to provide some validation of the model. In this chapter, we attempt to do this for part of the overall dynamics. Since a major part of the non-linearity of the system arises due to the fourbar kinematics, in this chapter, we concentrate particularly on the non-linear dynamics of the fourbar. We also validate the system parameters by performing system identification on the dynamics of a single fourbar.

4.1 Simplification of Fourbar Dynamics

We consider the dynamics of a single fourbar with a wing connected to it at a 45° angle of attack and at the same distance from the wing hinge as in the case of a full 2 degree of freedom (DOF) structure. This angle of attack was chosen to mimic the angle of attack which is seen for major part of a typical stroke cycle of a 2 DOF structure. All the analysis in this chapter was performed on the structure named $06-\alpha$.

We begin by re-stating the dynamics of a single DOF fourbar structure. This can be extracted easily from the overall system dynamics (3.87), by considering only the state variable θ_2. For the remainder of this chapter, we will drop the subscript and define θ as the angle made by the fourbar output. To summarize, the complete dynamics is given by:

$$\begin{aligned}(m_{fb}(\theta)+m_{act}(\theta)+m_{w,1})\ddot{\theta}&\\ +B_1\dot{\theta}+F_{aero}(\alpha=\alpha_0,\dot{\alpha}=0,\dot{\theta})r_1(\alpha=\alpha_0)&\\ +F_{k,act}(\theta)+F_{k,fb}(\theta)=T'_{inv}(\theta)V_{act}&\end{aligned} \tag{4.1}$$

In this equation, the angle of attack of the wing is fixed at 45°. This corresponds to a phase difference $\alpha=\alpha_0$ calculated from (2.29) as $\arcsin(\frac{\pi}{4\lambda})$. The aerodynamic parameters in the fourbar dynamics are calculated for this equivalent phase difference. In the above dynamics, non-linearity arises due to the fact that the inertia, damping and stiffness all vary with the state variable.

The dependence of m_{fb} on θ is given in Fig. 3.10. We can also simplify the aerodynamic damping term for the case of constant angle of attack as:

$$F_{aero} r_1 = B_2 \dot{\theta}^2 \tag{4.2}$$

where B_2 is a constant:

$$B_2 = \frac{1}{2} \rho A_w C_N(\alpha_0) x_0^3 \tag{4.3}$$

where ρ is the density of air, A_w is the wing area, C_N is the normal force coefficient for $\theta_x = \pi/4$ (which evaluates to 2.4) and x_0 is the equivalent wing length, i.e, the distance from the wing hinge at which the aerodynamic forces are assumed to act. B_2 has units of torque/(angular velocity squared). Finally, the variation of $F_{k,act}$ with θ is given in Fig. 3.12 and the variation of $F_{k,fb}$ with θ is given in Fig. 3.14.

Thus we can restate the exact dynamics of the fourbar mechanism as:

$$J(\theta)\ddot{\theta}(t) + F_{\text{damp}}(\dot{\theta}(t)) + F_{\text{stiff}}(\theta(t)) = T_i(\theta(t)) V_{act}(t) \tag{4.4}$$

4.1.1 Polynomial Approximation

A first step in the simplification of the fourbar dynamics is to approximate the terms in the dynamics as polynomials. Since we desire to simplify the polynomial descriptions, we shift the origin of the various curves such that the polynomial fits become most succinct. The shift is done both for the state variable θ and the input V_{act} in the following manner:

$$\theta \leftarrow \theta - \theta_0 \tag{4.5}$$

$$V_{act} \leftarrow V_{act} - V_{act,0} \tag{4.6}$$

Naturally, we need to choose θ_0 and $V_{act,0}$ to satisfy:

$$F_{k,fb}(\theta_0) + F_{k,act}(\theta_0) = T_{inv}(\theta_0)V_{act,0} \tag{4.7}$$

This shift is then equivalent to driving the structure with a constant DC bias of $V_{act,0}$ and measuring the displacement of the system about the DC bias of the output.

For the given system parameters shown in Figs. 3.10,3.11,3.12,3.14, we choose $\theta_0 = -145°$ and $V_{act} = -5V$, which enables us to get the following polynomial descriptions of the various terms:

$$\hat{J}(\theta) = J_0(1 - c\theta^2) \tag{4.8}$$

$$\hat{F}_{\text{damp}}(\dot{\theta}) = B_1\dot{\theta} + B_2\dot{\theta}|\dot{\theta}| \tag{4.9}$$

$$\hat{F}_{\text{stiff}}(\theta) = k_0\theta(1 - a\theta^2) \tag{4.10}$$

$$\hat{T}_i(\theta) = T_{i,0}(1 - b\theta^2) \tag{4.11}$$

Fig. 4.1 shows the comparision of the polynomial approximations of the various dynamic terms with the exact value. The polynomials correspond to the values of the various parameters specified in Table. 4.1.

Thus, we have an approximate "polynomial" dynamical system given by:

$$\hat{J}\ddot{\theta} + \hat{F}_{\text{damp}}(\dot{\theta}) + \hat{F}_{\text{stiff}}(\theta) = \hat{T}_i(\theta)V_{act} \tag{4.12}$$

4.2 The Describing Function Method

The describing function method is a well-studied technique for analysing the periodic behavior of non-linear systems. It is defined as a *quasi-linear approximation*

	Value	Units
J	22.3×10^{-12}	kg-m^2
c	0.10	
k_0	4.18×10^{-5}	Nm/rad
a	0.38	
B_1	2.61×10^{-9}	Nm/(rad/s)
B_2	9.77×10^{-12}	Nm/(rad/s)^2
$T_{i,0}$	2.0×10^{-7}	m/rad
b	0.42	

Table 4.1: Parameters used in polynomial fit (Fig. 4.1)

technique [Gelb 68]. The particular method described here has been termed as a "Single Sinusoid Describing Function" method (DF). The underlying philosophy is both intuitive and simple. Since we know (intuitively) that the forced response of a fourbar to periodic input has to be periodic, we approximate the forced response of the fourbar as a sum of harmonics. The simplification arises from the premise that we can get a reasonably good approximation to the actual output trajectory by "throwing away" the higher harmonic content of the output. We note that this is actually a significant assumption which has received considerable attention [Sanders 93, Bergen 71] and proceed with the caveat that a mathematical proof that the describing function method works at all is not going to be provided here. However, we will present a convincing argument using full non-linear simulation that the describing function method, at least for our case, works very well indeed.

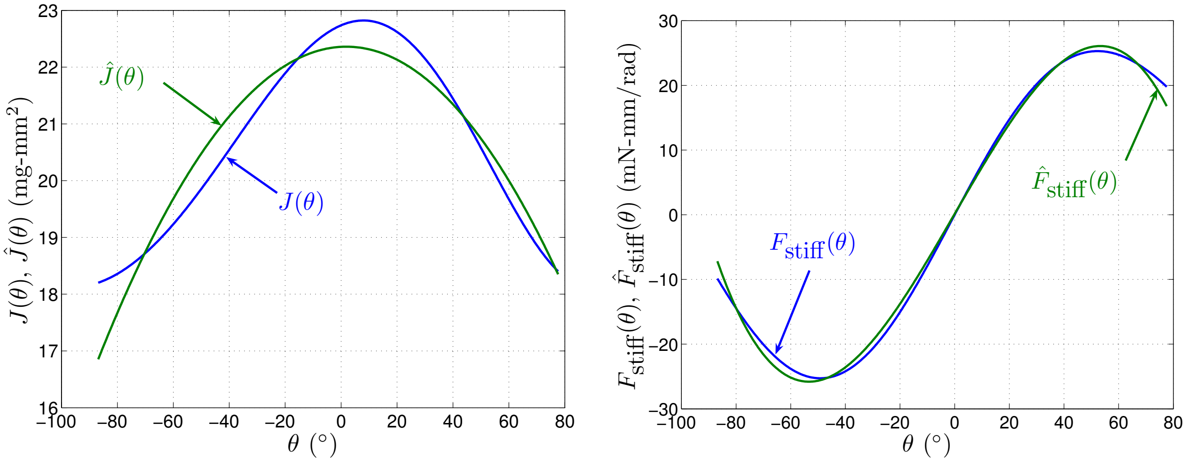

(a) $J(\theta)$ and $\hat{J}(\theta)$

(b) $F_{\text{stiff}}(\theta)$ and $\hat{F}_{\text{stiff}}(\theta)$

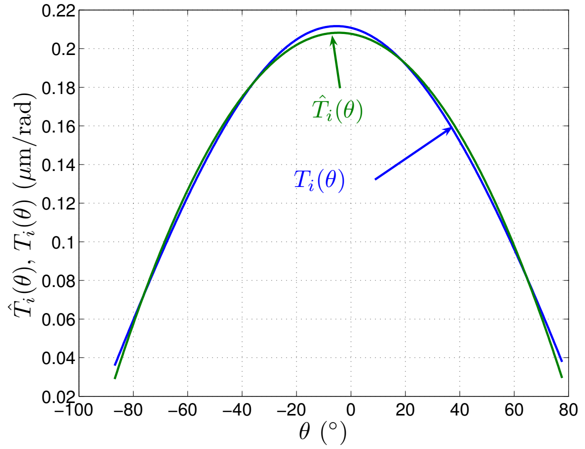

(c) $T_i(\theta)$ and $\hat{T}_i(\theta)$

Figure 4.1: Comparision of exact and approximate system parameters.

We will use the describing function method for a relatively simple task, namely getting the periodic response of the 1 DOF system for a forced sinusoidal input. We know that since our plant is non-linear, the output is not necessarily sinusoidal for a sinusoidal input. However, for the moment, we further restrict ourselves to the task of finding the first harmonic of the output waveform. To do this we proceed by first approximating the input and the output by simple sinusoidal trajectories:

$$u(t) = u_0 \sin(\omega t + \phi) \tag{4.13}$$

$$\theta(t) = \theta_0 \sin(\omega t) \tag{4.14}$$

We then substitute these waveforms into the polynomial approximation of the dynamics given by (4.12). For this given $\theta(t)$, we notice that the left hand side of the dynamics will have higher harmonic content. The Describing Function method proceeds by approximating this as a pure sinusoid at the driving frequency. This is done by taking the first harmonic of the various terms. As an example, consider the term $\hat{F}_{\text{damp}}(t)$:

$$\begin{aligned} \hat{F}_{\text{damp}}(t) &= B_1\dot{\theta} + B_2\dot{\theta}|\dot{\theta}| \\ &= B_1\theta_0\omega\cos(\omega t) + B_2(\theta_0\omega)^2\cos(\omega t)|\cos(\omega t)| \end{aligned}$$

The first harmonic of $\hat{F}_{\text{damp}}(t)$ can be found as:

$$\begin{aligned} \hat{F}_{\text{damp}}(t) \approx &\left(\frac{\omega}{\pi}\int_0^{2\pi/\omega} F_{\text{damp}}(\tau)\cos(\omega\tau)d\tau\right)\cos(\omega t) \\ &+ \left(\frac{\omega}{\pi}\int_0^{2\pi/\omega} F_{\text{damp}}(\tau)\sin(\omega\tau)d\tau\right)\sin(\omega t) \end{aligned} \tag{4.15}$$

This gives us

$$\hat{F}_{\text{damp}}(t) \approx \left(B_1\theta_0\omega + \frac{8B_2\theta_0^2\omega^2}{3\pi}\right)\cos(\omega t) \tag{4.16}$$

Similarly

$$\hat{J}(\theta(t))\ddot{\theta}(t) \approx J_0(1 - \frac{3}{4}c\theta_0^2)\theta_0\omega^2 \tag{4.17}$$

$$\hat{F}_{\text{stiff}}(t) \approx k_0\theta_0\left(1 - \frac{3}{4}a\theta_0^2\right)\sin(\omega t) \tag{4.18}$$

Note that for the $\hat{T}_i(\theta(t))u(t)$ term, we find the first harmonic of the whole compound term instead of finding approximations of each individual factor. This gives the following expression

$$\hat{T}_i(\theta(t))u(t) = T_{i,0}(1 - b\theta_0^2 \sin^2(\omega t))u_0 \sin(\omega t + \phi) \tag{4.19}$$

$$\approx T_{i,0}u_0 \left(1 - \frac{3}{4}b\theta_0^2\right) \cos\phi \sin(\omega t) + T_{i,0}u_0 \left(1 - \frac{1}{4}b\theta_0^2\right) \sin\phi \cos(\omega t) \tag{4.20}$$

Substituing the approximate expressions for $\hat{F}_{\text{damp}}(t)$, $\hat{F}_{\text{stiff}}(t)$ and $\hat{T}_i(\theta(t))u(t)$ into (4.12), we get the following:

$$\begin{aligned} &- J\theta_0\omega^2 \left(1 - \frac{3}{4}c\theta_0^2\right) \sin\omega t \\ &\qquad + \left(B_1\theta_0\omega + B_2\frac{8}{3\pi}\theta_0^2\omega^2\right) \cos\omega t + k_0\theta_0 \left(1 - \frac{3}{4}a\theta_0^2\right) \sin\omega t \\ &\approx \\ &T_{i,0}u_0 \left(1 - \frac{3}{4}b\theta_0^2\right) \cos\phi \sin(\omega t) + T_{i,0}u_0 \left(1 - \frac{1}{4}b\theta_0^2\right) \sin\phi \cos(\omega t) \end{aligned} \tag{4.21}$$

Equating coefficients of $\sin\omega t$ and $\cos\omega t$, we get

$$-J_0\theta_0\omega^2 \left(1 - \frac{3}{4}c\theta_0^2\right) + k_0\theta_0 \left(1 - \frac{3}{4}a\theta_0^2\right) = T_{i,0}u_0 \left(1 - \frac{3}{4}b\theta_0^2\right) \cos\phi \tag{4.22}$$

$$B_1\theta_0\omega + B_2\frac{8}{3\pi}\theta_0^2\omega^2 = T_{i,0}u_0 \left(1 - \frac{1}{4}b\theta_0^2\right) \sin\phi \tag{4.23}$$

This is the basic solution obtained using the describing function method. As can be seen, the method essentially converts a non-linear ODE into a set of non-linear algebraic equations which give the relationship between the drive amplitude and frequency and the output amplitude and phase.

The problem now is to find θ_0 and ϕ given u_0 and ω. In a linear system, this relationship is expressed succinctly with the frequency response graph, where we find the functions $\theta_0(u_0, \omega)$ and $\phi(u_0, \omega)$. For non-linear systems such as in our case, it is extremely difficult to get an explicit solution for $\theta_0(u_0, \omega)$ and $\phi(u_0, \omega)$. Instead, we solve for u_0 and ϕ explicitly given θ_0 and ω:

$$u_0^2 = \left(\frac{-J_0 \left(1 - \frac{3c}{4}\theta_0^2\right) \theta_0 \omega^2 + k_0 \theta_0 \left(1 - \frac{3}{4} a \theta_0^2\right)}{T_{i,0} \left(1 - \frac{3}{4} b \theta_0^2\right)} \right)^2 + \left(\frac{B_1 \theta_0 \omega + B_2 \frac{8}{3\pi} \theta_0^2 \omega^2}{T_{i,0} \left(1 - \frac{1}{4} b \theta_0^2\right)} \right)^2 \tag{4.24}$$

$$\phi = \tan^{-1} \left[\left(\frac{B_1 \theta_0 \omega + B_2 \frac{8}{3\pi} \theta_0^2 \omega^2}{-J_0 \left(1 - \frac{3}{4} c \theta_0^2\right) \theta_0 \omega^2 + k_0 \theta_0 \left(1 - \frac{3}{4} a \theta_0^2\right)} \right) \left(\frac{1 - \frac{3}{4} b \theta_0^2}{1 - \frac{1}{4} b \theta_0^2} \right) \right] \tag{4.25}$$

If we draw isocontours of constant $u_0 = \bar{u}_0$, then the points on the contour will correspond to the solutions of θ_0 for the given u_0 and ω. Such iso-contours can be thought to correspond to the solutions of θ_0 for a given u_0 and ω. If the plant had been a linear plant, these contours would have corresponded to the frequency response of the plant at increasing input amplitude. In the case of a non-linear plant like ours, these contours are called the “Single Sinusoid Driving Response” [Gelb 68]. Fig. 4.2 shows a set of such contours for the plant parameters corresponding to those in Table 4.1.

4.2.1 Validity of the Describing Function method

Note that in getting the “frequency response” of our plant using the Describing Function method (DF), we have made two approximations. The first is in approximating the exact plant dynamics given by (4.4) by a polynomial approximation (4.12).

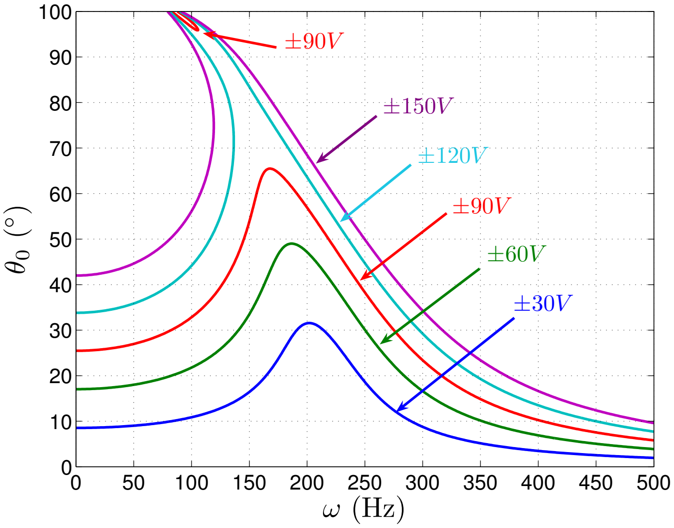

Figure 4.2: Contours of constant u_0

The next approximation is the DF approximation, i.e, trying to get the frequency response of the dynamics given by (4.12) by "throwing away" the higher harmonics of the output. In this section, we study the validity of these two approximations. We start with the latter approximation.

The DF Approximation

The DF approximation is stated as follows: Given that the dynamics of a system are given by (4.12), for the input

$$u(t) = u_0 \sin \omega t$$

the output is given by:

$$\theta(t) = \theta_0 \sin(\omega t - \phi) + \sum_{k=2}^{\infty} \theta_k \sin(k\omega t - \phi_k)$$

where θ_0 and ϕ are obtained by solving the non-linear algebraic equations (4.24) and (4.25). We can immediately see that this approximation leads to errors by comparing the exact DC motion with the approximate DC motion. The DF prediction of the DC motion follows from (4.24) by substituting $\omega = 0$. This gives:

$$u_{0,df} = \frac{k_0\theta_0\left(1 - \frac{3}{4}a\theta_0^2\right)}{T_{i,0}\left(1 - \frac{3}{4}b\theta_0^2\right)} \tag{4.26}$$

On the other hand, we can find the DC motion predicted by the polynomial dynamics (4.12) by substituting $\omega = 0$ as:

$$u_{0,ex} = \frac{k_0\theta_0\left(1 - a\theta_0^2\right)}{T_{i,0}\left(1 - b\theta_0^2\right)} \tag{4.27}$$

Thus the prediction of DC motion using the DF approximation will not be equal to the prediction using the exact dynamics. However, since the values of the nonlinear parameters a and b as shown in Table. 4.1 are almost equal, therefore the DC predictions do not vary too much as shown in Fig. 4.3. An interesting consequence of the fact that $a = b$ is that the input-output relationship is very linear for low frequencies. In other words, the weakening transmission implied by (4.11) almost exactly cancels the effect of the softening spring implied by (4.10). Fig. 4.4 shows a comparison of the frequency response predicted by the DF approximation with a full non-linear ODE45 simulation done using MATLAB. The solid lines represent the contours of constant u_0 as calculated by the DF approximation. The marker points correspond to the first harmonic of $\theta(t)$ obtained by simulating the dynamics given by (4.12) using a full ODE45 simulator for the parameters given in Table 4.1. As can be seen, the predictions match up almost exactly with a small amount of variation at high amplitudes. This once again implies that the DF approximation, at least for our case is very accurate at predicting the frequency response.

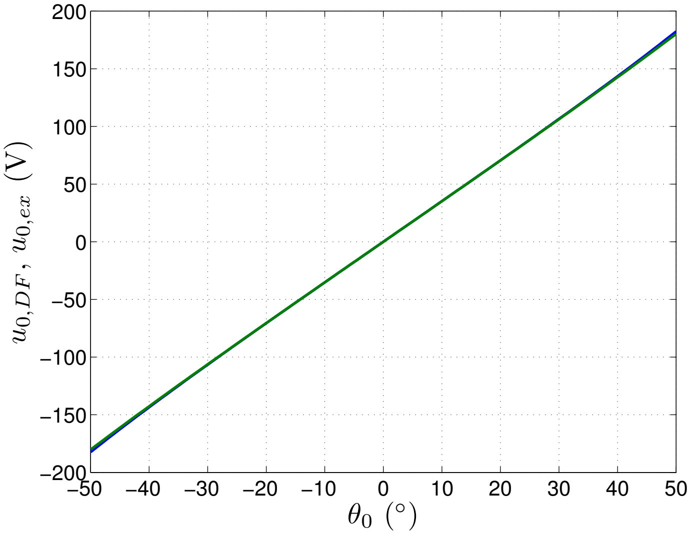

Figure 4.3: Comparison of DC motion predicted by the DF approximation and the exact polynomial dynamics. The two predictions are so similar that the lines are not distinguishable.

.

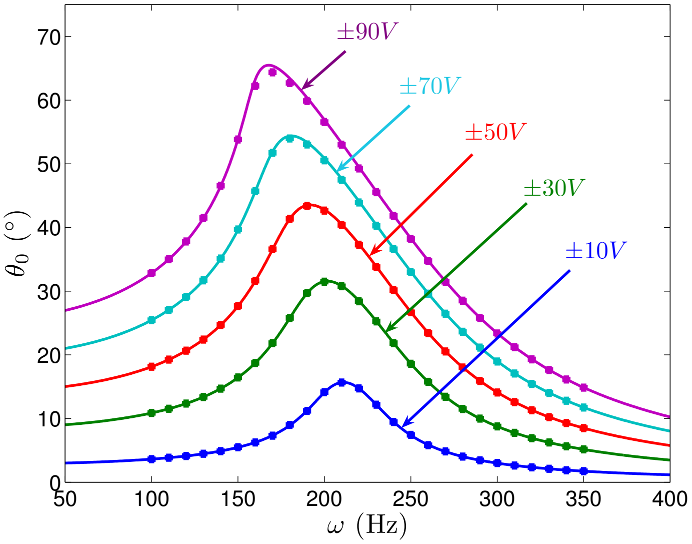

Figure 4.4: Comparison of frequency response predicted by the DF approximation and the exact polynomial dynamics.

The Polynomial Approximation

The DF method of finding the frequency response is preceded by the polynomial approximation where we approximate the plant dynamics given by (4.4) by the polynomial plant dynamics (4.12). Fig. 4.5 shows a comparison of the frequency response obtained via a full non-linear simulation of the exact plant dynamics with the response predicted by the DF method. The solid lines correspond to the frequency response predicted by the DF method. The line with the markers correspond to the frequency response obtained via full nonlinear simulation. Note that since the exact plant dynamics is non-linear, frequency response here corresponds to driving the plant with a sinusoidal input and then finding the frequency component of the output at the driving frequency. As can be seen, we still see a good agreement between the full

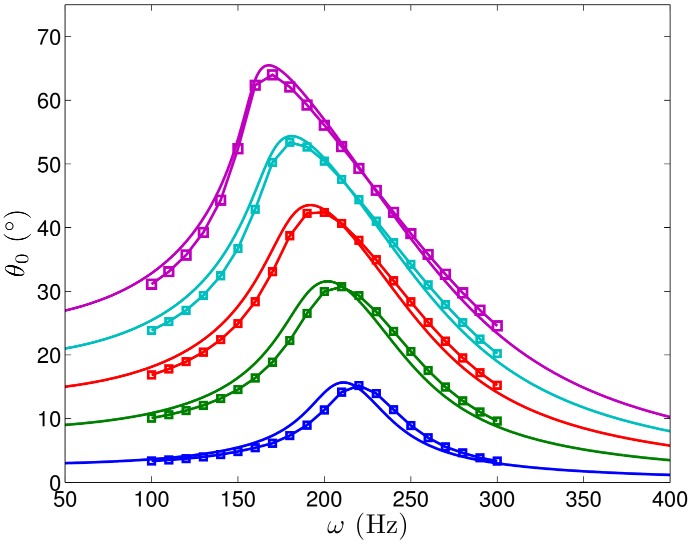

Figure 4.5: Comparison of frequency response of exact plant dynamics (4.4) and DF frequency response (4.24).

nonlinear dynamics and the DF method.

4.3 Jump Resonance in Fourbar Mechanisms

The DF method allows us to explore an interesting aspect of the non-linear dynamics of the fourbar mechanism called “Jump Resonance”. This is a phenomenon where there is a sudden jump in the output amplitude for a small change in the input frequency with the input amplitude kept constant. Such a phenomenon cannot occur in a linear system. Let us concentrate on the $u = \pm 130$ contour shown in Fig. 4.2.

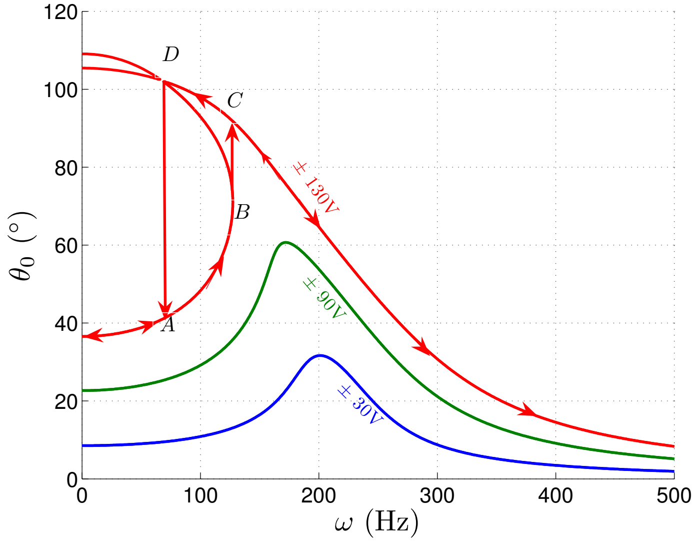

Figure 4.6: Jump resonance exhibited by one degree of freedom fourbar

This contour corresponds to the possible solutions for the output amplitudes at each input frequency with the input amplitude held constant at 150. To see how jump resonance occurs, let us assume that we start with a low input frequency, say 50Hz and slowly increase it keeping $u_0 = 150$ as shown in Fig. 4.6. Between $\omega = \omega_A$ and $\omega = \omega_B$, we have multiple solutions for θ_0. The actual steady state solution will be based on how we approach the frequency ω. To be more precise, while slowly increasing the input frequency, till $\omega = \omega_B$, since we always have a local solution, the output amplitude increases along the path $A - B$. Beyond $\omega = \omega_B$, there is no output amplitude solution in the vicinity of $\theta_{0,B}$. Therefore, increasing the frequency even by a small amount suddenly makes the output amplitude jump to the vicinity of $\theta_{0,C}$. Thus when we start from a low frequency and slowly increase to a high frequency, the path traced by the fourbar output is *low*–A–B–C–*high*, where B–C is a sudden "jump". Similarly, when we sweep from a high frequency to low, the path traced is *high*–C–D–A–*low*, where D–A is a sudden "jump".

It is clear from looking at Fig. 4.6 that not all input amplitudes give rise to a "jump resonance" behavior. For example, at $u_0 = \pm 90$, the contour does not "fold back", which means that sweeping the frequency slowly will not lead to any sudden jumps. This phenomenon presents additional constraints on the maximum allowed input amplitudes which can be applied to the fourbar mechanism.

4.4 Identification of Nonlinear Dynamic Parameters

The DF method also allows us to perform a system parameter identification of the various dynamic parameters of the fourbar dynamics.

4.4.1 Problem Statement

Given an experimentally measured set of frequency responses, try to determine the system parameters which best predict the measurements. More formally, we assume that the system can be modeled by the following simplified second order nonlinear

ODE as described in (4.12), where the various mass and stiffness terms are given in (4.8)–(4.11).

Solving this nonlinear ODE involves finding the output waveform $\theta(t)$ given the input waveform $u(t)$. In particular, we can solve for $\theta(t)$ given that the input is a single sinusoid of the form $u(t) = u_0 \sin(\omega t)$. If we solve the ODE, we will in general get a non-sinusoidal output waveform. For the present, we are interested only in the primary harmonic. This can be calculated by first solving the nonlinear ODE and then extracting the first harmonic by a simple Fourier transform. This yields the amplitude and relative phase

$$\theta_{0,m} = S_{\theta_0}(u_0, \omega, \lambda) \tag{4.28}$$

$$\phi_m = S_\phi(u_0, \omega, \lambda) \tag{4.29}$$

where λ corresponds to the system parameters:

$$\lambda = \{J, B_1, B_2, k_0, a, b\} \tag{4.30}$$

Using this method, we can generate a set of "modeled" frequency response (FRSP) points of the form:

$$\text{FRSP}_{\text{model}} = \{(u_0, \omega, \theta_{0,m}, \phi_m)_1, \cdots\} \tag{4.31}$$

In this problem, we are *given* a set of measured frequency responses of the form $\{u_0, \omega, \theta_0, \phi\}$. A single measurement of this form refers to driving the system with a known input sinusoid of the form $u_0 \sin(\omega t)$ and measuring the amplitude and relative phase θ_0 and ϕ of the first harmonic of the output waveform. Thus we are given a set of measurement points:

$$\text{FRSP}_{\text{exp}} = \{(u_0, \omega, \theta_{0,e}, \phi_e)_1, \cdots\} \tag{4.32}$$

Our problem then is to find λ (the set of system parameters) such that the difference between the measured and modeled frequency responses is minimized:

$$\min_{\lambda} \|\mathrm{FRSP}_{\mathrm{exp}} - \mathrm{FRSP}_{\mathrm{model}}\| \tag{4.33}$$

4.4.2 Experimental Data

The experimental data consists of a series of frequency responses of a fourbar at increasing input amplitudes as shown in Fig. 4.7.

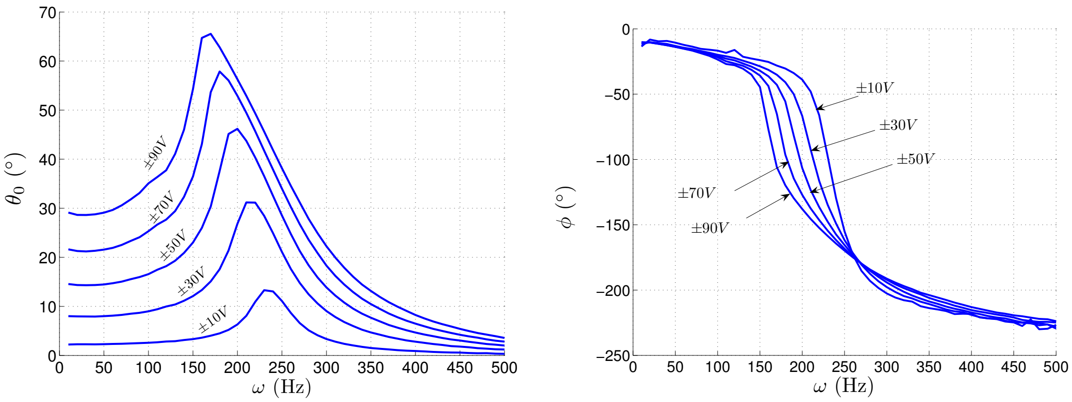

(a) Magnitude

(b) Phase

Figure 4.7: Experimental data

Each curve above represents the first harmonic of the output when the input amplitude is held constant and the input frequency is swept from 10Hz to 500Hz in steps of 10Hz. The labels on each curve represent the input amplitude (voltage) applied to the actuator for that sweep.

4.4.3 Application of the Describing Function method

As described previously, the method of "describing function" gives an approximate solution to the nonlinear ODE. Without going into detail here, we substitute $u(t) = u_0 \sin(\omega t + \phi)$ and $\theta(t) = \theta_0 \sin(\omega t)$ into (4.4) and then equate the first harmonic of both sides of the equation, i.e, the coifficients of $\sin \omega t$ and $\cos \omega t$. This gives the following equalities:

$$\begin{aligned} -J\theta_0\omega^2 + k_0\theta_0 \left(1 - \frac{3}{4}a\theta_0^2\right) &= u_0 \left(1 - \frac{3}{4}b\theta_0^2\right) \cos\phi \qquad (4.34) \\ B_1\theta_0\omega + B_2\frac{8}{3\pi}\theta_0^2\omega^2 &= u_0 \left(1 - \frac{1}{4}b\theta_0^2\right) \sin\phi \qquad (4.35) \end{aligned}$$

Thus for each set of drive amplitude and drive frequency $(u_{0,i},\ \omega_i)$ and the corresponding output amplitude and phase measurements $(\theta_{0,i},\ \phi_i)$, we get two linear equations in the system parameters λ as follows:

$$\begin{bmatrix} -\theta_{0,i}\omega_i^2 & \theta_{0,i} & -\frac{3}{4}\theta_{0,i}^3 & \frac{3}{4}u_{0,i}\theta_{0,i}^2\cos\phi & 0 & 0 \\ 0 & 0 & 0 & \frac{1}{4}u_{0,i}\theta_{0,i}^2\sin\phi & \theta_{0,i}\omega_i & \frac{8}{3\pi}\theta_{0,i}^2\omega^2 \end{bmatrix} \begin{bmatrix} J \\ k_0 \\ k_0 a \\ b \\ B_1 \\ B_2 \end{bmatrix} \approx \begin{bmatrix} u_{0,i}\cos\phi_i \\ u_{0,i}\sin\phi_i \end{bmatrix} \qquad (4.36)$$

By stacking up a number of such measurements, we can form a regression equation of the form:

$$A\lambda \approx B \tag{4.37}$$

where A is composed by stacking up 2×6 matrix blocks on the left hand side of (4.36) and B is composed by stacking up 2×1 matrix blocks in the right hand side of (4.36). To solve for the system parameters λ, we need to perform the following minimization:

$$\min_{\lambda} \|A\lambda - B\| \tag{4.38}$$

If we use the $\mathcal{L}_2$ norm in the above minimization, the estimated system parameters can be found as:

$$\hat{\lambda} = A^{\dagger} B \tag{4.39}$$

where $A^{\dagger}$ represents the pseudo inverse of A. As a first step in making A better conditioned, we change coordinates so that ω is measured in $rads/ms$, θ is measured in $rads$ and u_0 is measured in hectoVolts (i.e, 100V is represented by $u_0 = 1$.)

4.4.4 The Problem due to Phase Delay

If we try to apply the procedure above to the measured data, we get a bad fit as shown in Fig. 4.8. The red lines with labels represent the contours of constant u_0 as found by the describing function using the fitted parameters $\hat{\lambda}$. The blue lines represent the measured magnitude. For this figure, we used all the measured frequency points for all applied input amplitudes. As can be seen the fit has significant

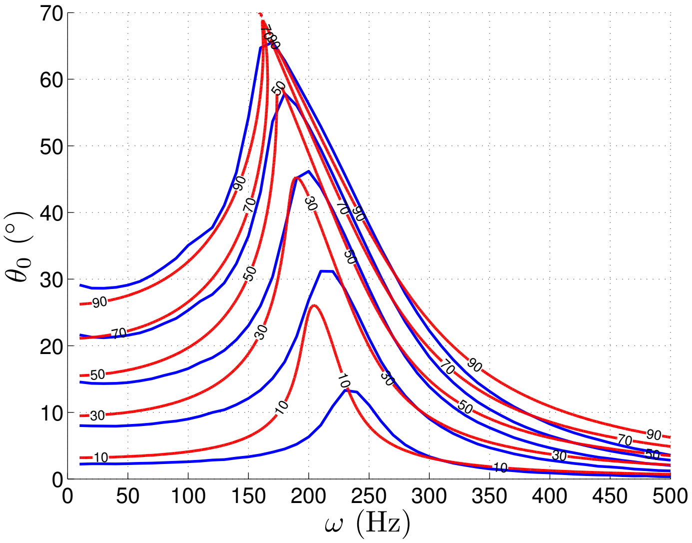

Figure 4.8: Comparision of measured magnitude with “fitted” amplitude

deviations from the measurement.

If we try to use the measurement points from a single input amplitude measurement, we see that the fit for that particular frequency sweep improves, while the fit on the other sweeps deteriorates significantly as shown in Fig. 4.9, which shows the fit when only the measurement with $u_0 = \pm 50V$ is used. The thick red line with the label represents the “fitted” frequency response at $u_0 = \pm 50V$, while the thick blue line represents the measurement at $u_0 = \pm 50V$.

Even when trying to fit a single input amplitude sweep, we notice that the fit is not quite as good as we expect it to be considering that the measured amplitude looks like a “well behaved” second order system. In particular, the sharp “corner” in the predicted frequency response is suspicious. In order to understand the source of

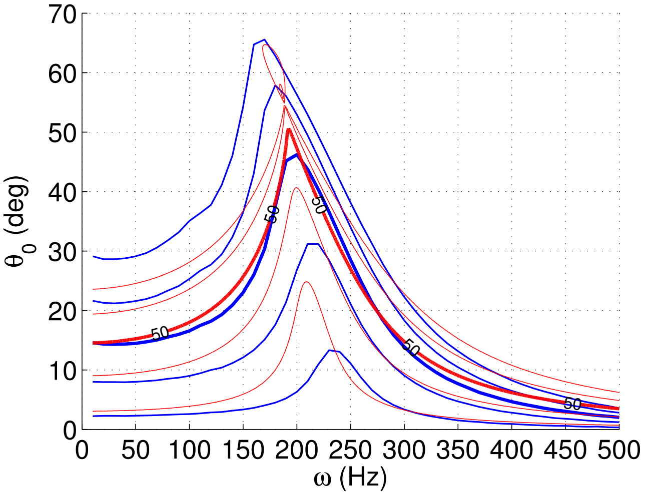

Figure 4.9: Comparision of measured magnitude with "fitted" amplitude when only the measured frequency sweep at $u_0 = \pm 50V$ is used.

the error in the fit, we break up the matrices A and B from (4.37) as

$$A = \begin{bmatrix} A_1 & 0_{N\times 3} \\ 0_{N\times 2} & A_2 \end{bmatrix} \tag{4.40}$$

$$B = \begin{bmatrix} B_1 \\ B_2 \end{bmatrix} \tag{4.41}$$

where

$$A_1 = \begin{bmatrix} -\theta_{0,i}\omega_i^2 & \theta_{0,i} & -\frac{3}{4}\theta_{0,i}^3 & \frac{3}{4}u_{0,i}\theta_{0,i}^2\cos\phi \end{bmatrix} \tag{4.42}$$

$$A_2 = \begin{bmatrix} \frac{1}{4}u_{0,i}\theta_{0,i}^2\sin\phi & \theta_{0,i}\omega_i & \frac{8}{3\pi}\theta_{0,i}^2\omega^2 \end{bmatrix} \tag{4.43}$$

$$B_1 = [u_{0,i}\cos\phi_i] \tag{4.44}$$

$$B_2 = [u_{0,i}\sin\phi_i] \tag{4.45}$$

We also break up the system parameters λ as

$$\lambda = \begin{bmatrix} \lambda_1 \\ \lambda_2 \end{bmatrix} \tag{4.46}$$

where $\lambda_1 = \{J, k_0, k_0 a, b\}$ and $\lambda_2 = \{b, B_1, B_2\}$. Note that λ_1 and λ_2 share the parameter b, which represents the input saturation. If $\hat{\lambda}_1$ and $\hat{\lambda}_2$ represent the estimates of λ_1 and λ_2, then we expect that

$$A_1\hat{\lambda}_1 \approx B_1 = u_0 \cos\phi \tag{4.47}$$

$$A_2\hat{\lambda}_2 \approx B_2 = u_0 \sin\phi \tag{4.48}$$

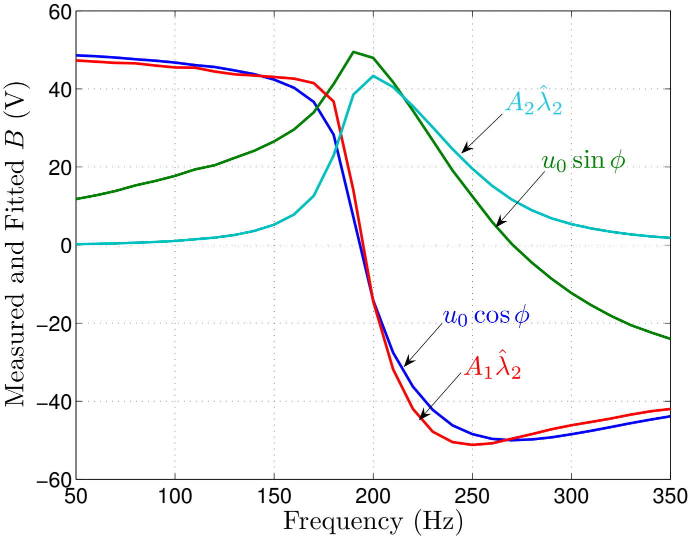

Figure 4.10: Comparision between the actual and fitted B

However, as Fig. 4.10 shows, although $A_1\hat{\lambda}_1$ and $B_1 = u_0 \cos\phi$ match up pretty well, the match between $A_2\hat{\lambda}_2$ and $B_2 = u_0 \sin\phi$ is very poor. This implies that $u_0 \sin\phi$ has some behavior which none of the columns of A_2 have. This can be easily seen in Fig. 4.11. As can be seen, none of the basis functions used for fitting $u_0 \sin\phi$

ever change sign like $u_0 \sin\phi$ does. Now, $u_0 \sin\phi$ changes sign because as shown in Fig. 4.7(b), the measured phase decreases below $-180°$ due to the constant slope and offset added onto it due to the delay inherent in the experimental measurement.

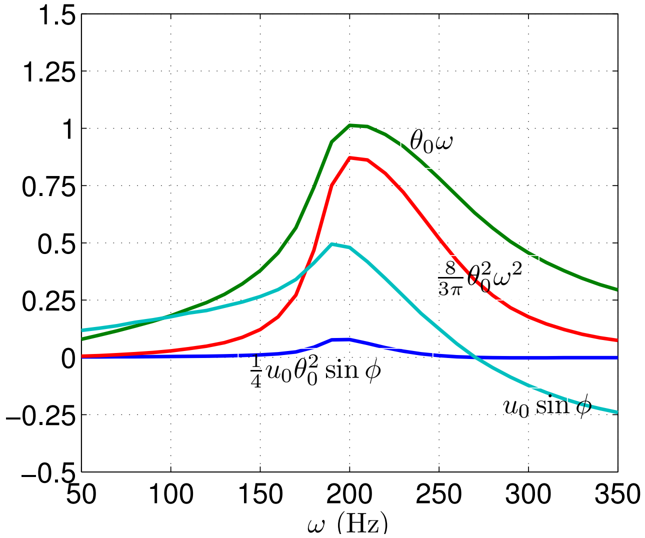

Figure 4.11: Basis functions for fitting $u_0 \sin\phi$. Note that although ω is depicted on the X axis in Hz, the values plotted use the value of ω in $rads/ms$.

To account for this, we change the system identification problem (4.36) to include an affine phase offset. Thus we get:

$$\begin{bmatrix} -\theta_{0,i}\omega_i^2 & \theta_{0,i} & -\frac{3}{4}\theta_{0,i}^3 & \frac{3}{4}u_{0,i}\theta_{0,i}^2\cos\phi & 0 & 0 \\ 0 & 0 & 0 & \frac{1}{4}u_{0,i}\theta_{0,i}^2\sin\phi & \theta_{0,i}\omega_i & \frac{8}{3\pi}\theta_{0,i}^2\omega^2 \end{bmatrix} \begin{bmatrix} J \\ k_0 \\ k_0 a \\ b \\ B_1 \\ B_2 \end{bmatrix} \approx \begin{bmatrix} u_{0,i}\cos(\phi_i - \omega t_0 - \phi_0) \\ u_{0,i}\sin(\phi_i - \omega t_0 - \phi_0) \end{bmatrix} \tag{4.49}$$

The parameters to be estimated now are $\{J, k_0, a, B_1, B_2, b, t_0, \phi_0\}$. Unfortunately, the estimation of t_0 and ϕ_0 is more complicated due to the fact that the regression equation is not linear in t_0 and ϕ_0. Thus our minimization problem becomes

$$\min_{\lambda, t_0, \phi_0} \|A\lambda - \tilde{B}\| \tag{4.50}$$

where $\tilde{B}$ is defined simply as:

$$\tilde{B} = \begin{bmatrix} u_{0,i}\cos(\phi_i - \omega t_0 - \phi_0) \\ u_{0,i}\sin(\phi_i - \omega t_0 - \phi_0) \end{bmatrix} \tag{4.51}$$

Instead of trying to tackle this as a single nonlinear optimization problem, we break it up into two separate optimization problems by considering the optimization of t_0 and ϕ_0 separately. Thus we get:

$$\min_{t_0, \phi_0} \min_{\lambda} \|A\lambda - \tilde{B}\| \tag{4.52}$$

The optimization of λ for given values of t_0 and ϕ_0 proceeds as before. The optimization of t_0 and ϕ_0 is done using `MATLAB`'s `fminunc` function for unconstrained optimization.

Accounting for the phase offset imeediately provides us a much better fit with the experimentally measured data.

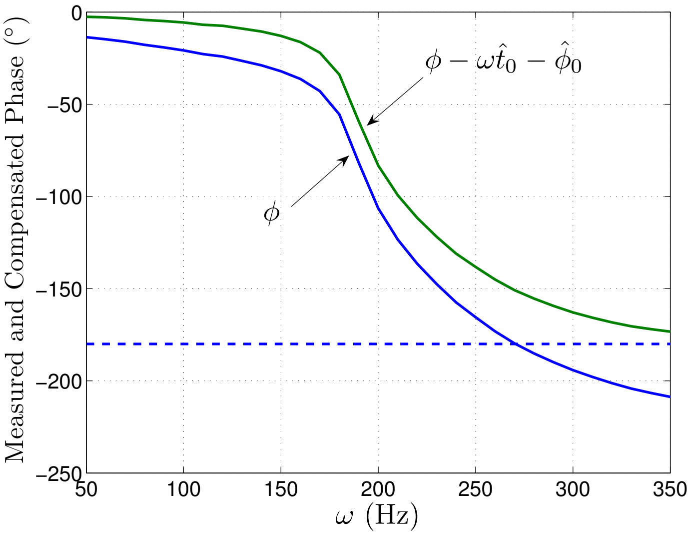

Figure 4.12: Phase after accounting for affine phase offset

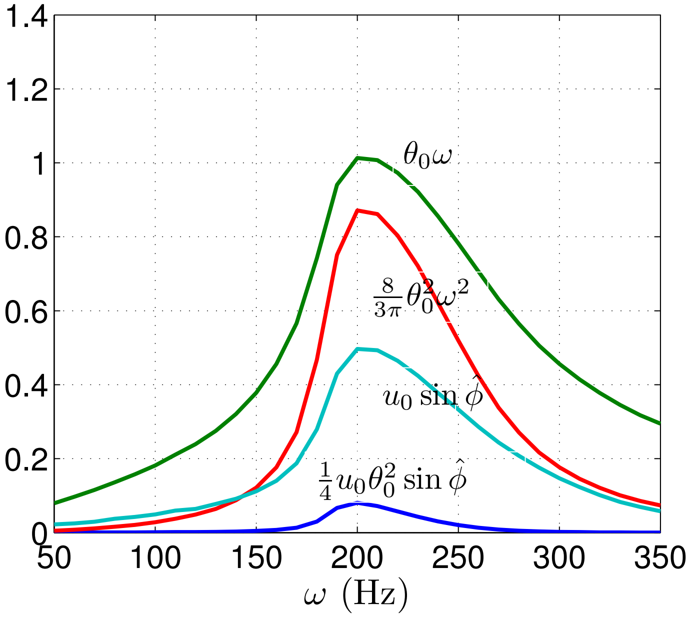

Figure 4.13: Basis functions for fitting $u_0 \sin\hat{\phi}$. $\hat{\phi}$ is defined as $\phi - \omega\hat{t}_0 - \hat{\phi}_0$, where $\hat{\phi}_0$ and $\hat{t}_0$ are optimal values after performing the minimization (4.52).

Fig. 4.12 shows the change in the phase of the measurement after accounting for the system delay. The figure shows the original phase measurement for the $u = \pm 50V$ frequency sweep and the fitted phase after accounting for the delay. As can be seen, the fitted phase remains above $-180°$. This has the desired effect on the $\tilde{B}_2$ as shown in Fig. 4.13. $u_0 \sin \hat{\phi}$ no longer changes signs which means that the basis functions, i.e, the columns of A_2 have a much better chance of fitting it.

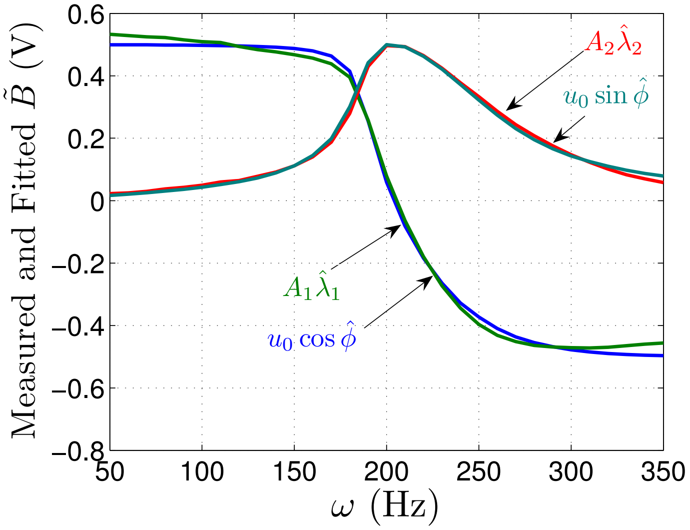

Figure 4.14: Comparision of actual and fitted $\tilde{B}$

Fig. 4.14 shows the comparision of the actual and fitted $\tilde{B}$ after accounting for the phase offset for the $u_0 = \pm 50V$ measurement. As can be seen, we immediately get a much better fit with the measured data. If we utilize this procedure to get the fit considering all the data points, we get a very good fit as shown in Fig. 4.15. The fit for large input amplitudes is much better than for small input amplitudes, but overall this is still a very good fit. Since we know all the geometric and other fabrication parameters for 06-α (the 1 DOF structure being studied in this chapter), we can also simulate the frequency response by calculating a-priori the values of J, k_0 etc.

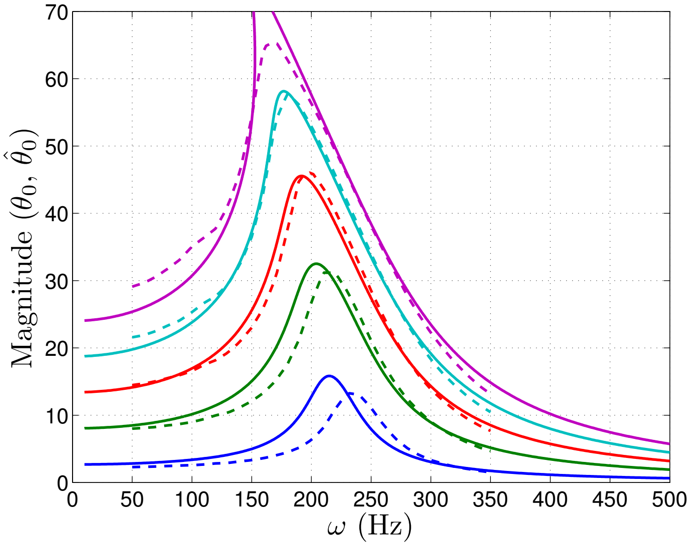

Figure 4.15: Final magintude fit of $06 - \alpha$ using the extended describing function method

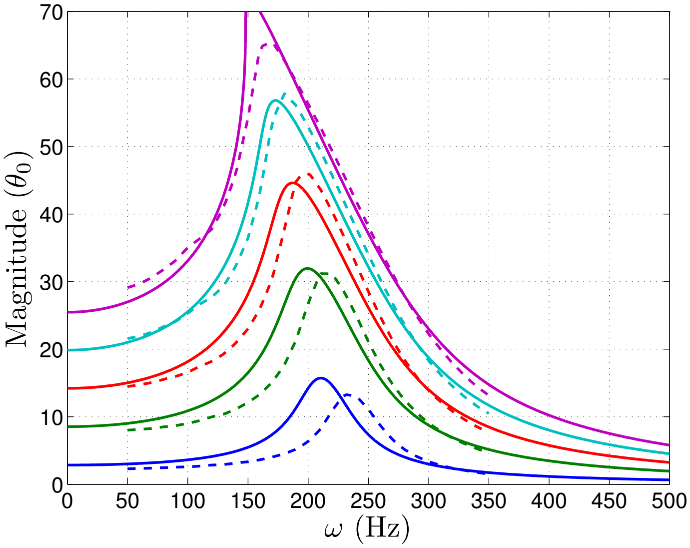

Figure 4.16: Comparision of $06 - \alpha$ experimental frequency sweep with simulated frequency sweep

Param	SysID	Calculation	Units
J	22×10^{-12}	22.8×10^{-12}	kg-m^2
k_0	4.19×10^{-5}	4.18×10^{-5}	N-m/rad
a	-0.3801	-0.3850	–
b	0.4267	0.4186	–
B_1	2.6×10^{-9}	2.6×10^{-9}	N-m-s/rad
B_2	8.24×10^{-12}	9.77×10^{-12}	N-m-s^2/rad^2
$T_{i,0}$	1.966×10^{-7}	2.07×10^{-7}	N-m/V

Table 4.2: Comparision of parameters obtained with system ID with prameters calculated via dynamics

Fig. 4.16 shows the comparision of the measured frequency response with the simulated frequency response. Table. 4.2 compares the parameters obtained using the system ID approach with the parameters calculated using fabrication data. As can be seen, there is a very good agreement between the calculated parameters and those obtained via system ID.

4.5 Estimation of internal damping

Another important performance criterion in the performance of a fourbar is its transmission efficiency. This is dependent on the internal damping inherent in the fourbar flexures. In order to estimate this, we performed a series of system identification experiments on a single DOF fourbar, by flapping the wing while it was enclosed in a vacuum chamber such that the pressure of air in which the wing was flapping could be controlled. We performed these experiments at 5 pressure points and estimated the system parameters λ at each pressure. At each pressure point, we measured experimentally the frequency response of the system to increasing input amplitudes up to $\pm 40V$. By extrapolating the estimate of B_1 to zero ambient pressure, we can estimate the internal damping arising purely due to the mechanical damping inherent in the flexures and the actuator. Fig. 4.17 shows the frequency response measurements at the 5 pressure points. The pressure in inches of mercury below atmosphere is denoted beneath each figure. The response of the "fitted" system is shown superimposed on each measured frequency response. As can be seen, we get a very good fit between the measured and fitted frequency responses. Fig. 4.18 shows the variation of the various system parameters with decreasing pressure. We immediately notice that the estimates of the nonlinear system parameters do not agree with the *a priori* estimates of the parameters shown in Table 4.2 as well as the parameters obtained by the system ID with large input amplitudes. This is reasonable because the effect of non-linearities is felt more acutely with larger input amplitudes and therefore they can be estimated more accurately by measuring the response for large input amplitudes. Another thing to note from these measurements is that B_1 decreases with decreasing pressure. This implies that in the overall system dynamics, we cannot really "separate" the influence of aerodynamics from the internal damping.

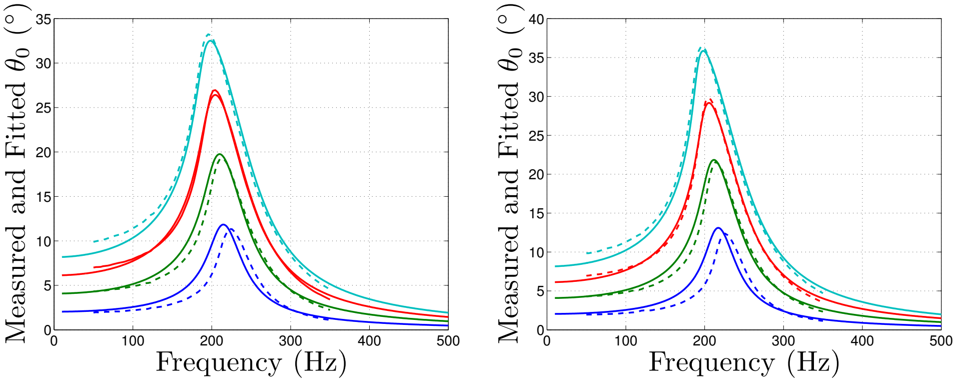

(a) 0 in Hg

(b) -6 in

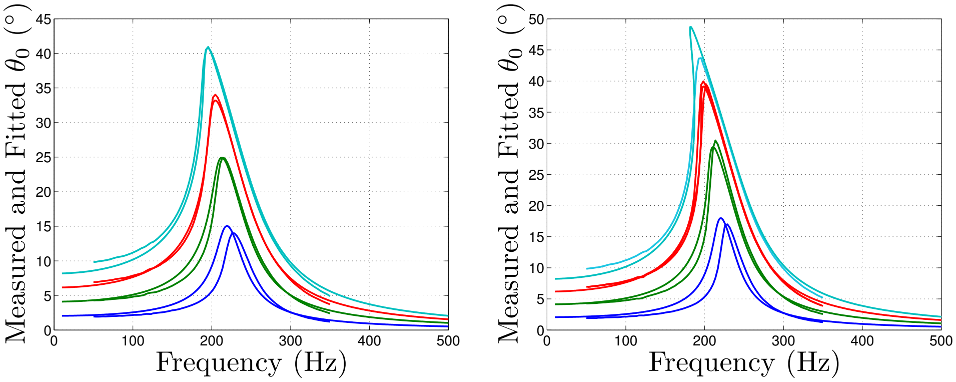

(c) -12 in Hg

(d) -18 in

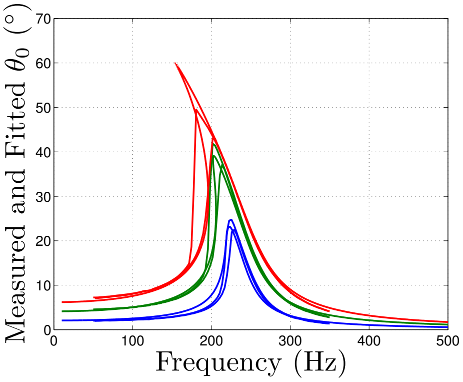

(e) -23 Hg

Figure 4.17: Vaccuum measurements of $06 - \alpha$

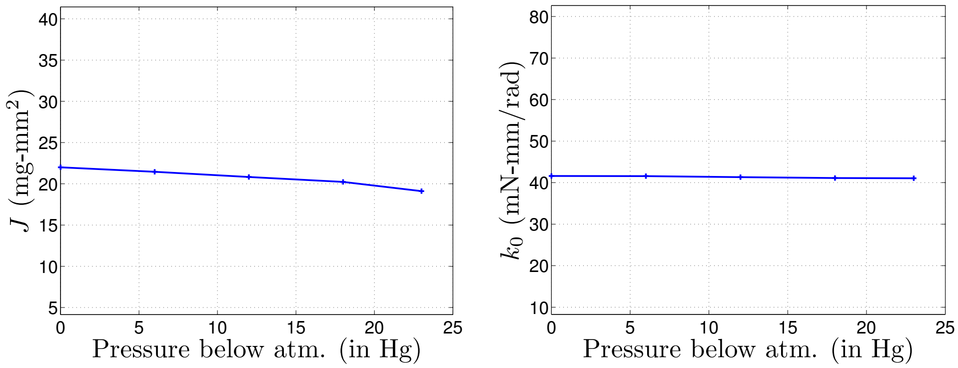

(a) J (mg-mm^2)

(b) k_0 (mN-mm/rad)

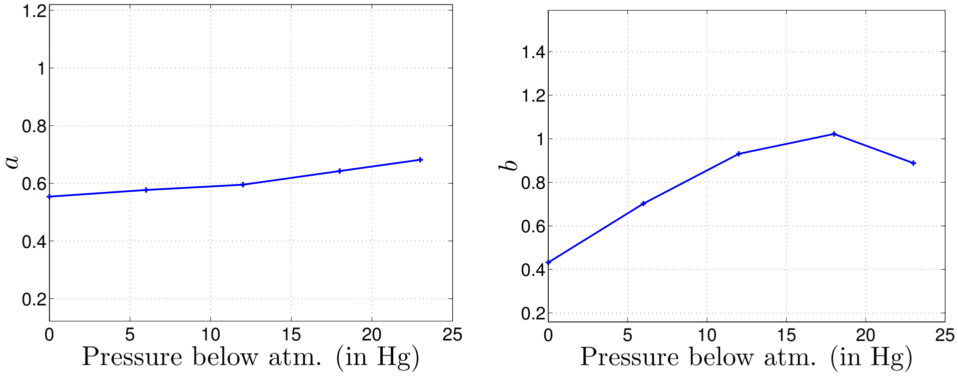

(c) a

(d) b

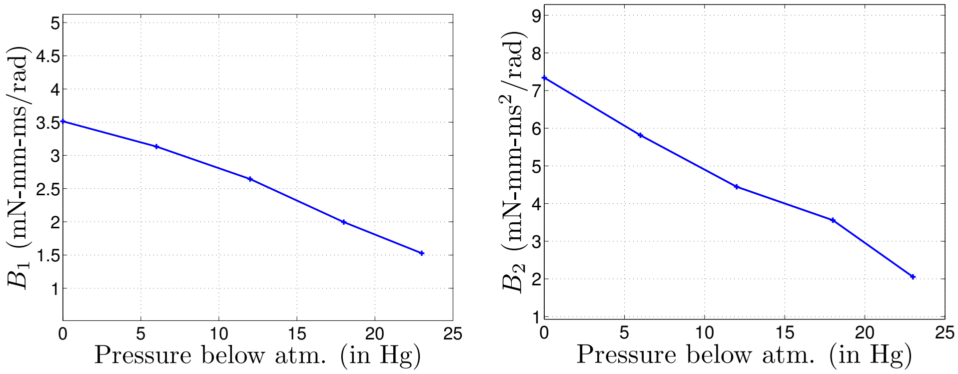

(e) B_1 (mN-mm-ms/rad)

(f) B_2 (mN-mm-ms^2/rad^2)

Figure 4.18: Vaccuum system ID parameters for $06 - \alpha$

However, extrapolating B_1 and B_2 to -29” Hg (i.e, perfect vacuum) still provides a good way to estimate the internal material damping of the actuator and flexures. By extrapolating the data shown in Fig. 4.18(e,f), we see that for very low pressures B_1 reduces to 1 mN-mm-ms/rad and B_2 reduces to 0.84 mN-mm-ms^2/rad^2. The power dissipated by the damping terms is given by:

$$P_{out} = \frac{1}{2}\left(B_1 + B_2\frac{8}{3\pi}\theta_0\omega\right)\theta_0^2\omega^2 \tag{4.53}$$

If we compare the power dissipations for the two cases: in full atmospheric pressure and in vacuum, we see that

$$P_{out,atm} = 4.71\ mW$$

$$P_{out,vac} = 0.85\ mW$$

where we have used $\theta_0 = \pi/4$, $\omega = 200$Hz and:

	Atmospheric pressure	Vacuum
B_1	3.6 mN-mm-ms/rad	1 mN-mm-ms/rad
B_2	7.3 mN-mm-ms^2/rad^2	0.83 mN-mm-ms^2/rad^2

From this we can see that the internal material damping in the fourbar and actuator consume about 18% of the total power. This implies that the *transmission efficiency* of the fourbar is at least 80%, if not better.

4.6 Summary

In this chapter, we described a simplification to the fourbar dynamics which allowed us to apply the powerful *Describing Function* method to study the fourbar dynamics from a more analytical perspective. We described the jump resonance behavior of the fourbar which can be analyzed elegantly using this method. We also validated the non-linear behavior of the fourbar by performing parameter identification of the fourbar dynamics and showing that we get close agreement to the parameters obtained using a-priori calculations. The internal damping of the actuator and fourbar system was estimated to verify that the mechanical transmission is highly efficient at converting mechanical motion from the actuator into wing motion.

Chapter 5

Design and Fabrication Issues

Thus far, we have concentrated on the theoretical aspects of the MFI such as the kinematics, dynamic analysis and system identification. In this chapter, we will concentrate on the mechanical design and fabrication aspects of the MFI. The structural components of the MFI are described as *flexural mechanisms*, where rigid links are joined together by flexures which approximate rotational joints. In this chapter, we will concentrate on various aspects of building flexural mechanisms focussing particularly on the design of the flexures. Some of the design principles in the construction of flexural mechanisms have been studied previously [Carricato 01, Kang 04] and have been used in increasingly many applications [Kota 99, Yi 03]. Some of the basic design issues involved in the fabrication of small length flexural mechanisms have treated previously in [Howell 94]. Researchers have also studied various kinds of flexures for obtaining rotational motion from the point of view of optimal force transmission [Goldfarb 99]. Related work is currently ongoing on methods of automatically folding flexural mechanisms [Sahai 03] and embedding wiring inside the flexures themselves [Sahai 05]. The various performance aspects of the carbon fiber (CF) links have been elaborated in [Wood 03]. In this chapter, we study an application of some of these general design principles and intuition to the manufacturing process presently used in the MFI project.

During the first few years of the MFI project, the manufacturing process consisted of folding up flat steel shim into hollow triangular beams as described in [Shimada 00]. This process involved a lot of careful gluing and folding and suffered from excessive flexure peel. It also limited the alignment to what could be achieved manually. Moreover, the time required to build a typical fourbar mechanism in this process was on the order of a couple of days.

[Wood 03] introduced a radically improved way of making composite meso-structures by utilizing flexures sandwiched between carbon fiber sheets. This fabrication method completely avoids the problem of manually gluing flexures (and the resultant peeling problems) by utilizing the strong bond formed between carbon fiber epoxy sheets while curing. It is also a significantly shorter process, taking about 5 times less time than the previous steel folding technique to build an equivalent part. By "freezing" some of the flexural joints, elaborate 3D structures can be built from planar 2D patterns.

For this chapter, we use two flexural mechanisms currently used in the MFI project as driving examples. The first is the fourbar mechanism which is designed to amplify the motion of the PZT actuators by about 3000 rads/m described in Section 2.2. The second is differential mechanism shown in Fig. 2.8. Two important performance criteria for judging the performance of the fourbar mechanism are its "parallel stiffness"

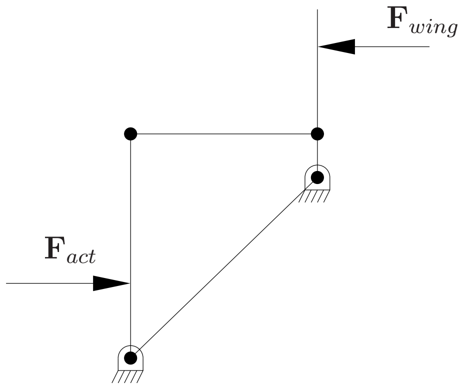

Figure 5.1: Kinematic diagram of a simple fourbar mechanism showing the typical external forces acting on it.

and its "serial stiffness". Parallel stiffness refers to the force F_{act} required to drive the input joint (Fig. 5.1) with all the links left free to rotate. For planar mechanisms like fourbars, this stiffness depends purely on the stiffness of the flexures. As we will later show, for 3D mechanisms, we also need to be very careful about alignment of the flexures. Serial stiffness refers to the free movement possible at the output link of the fourbar when the input link is fixed. In Fig. 5.1, this refers to the motion caused by F_{wing} when the input link is fixed.

5.1 Force Analysis

In this section we do a force analysis of the fourbar and give a systematic method for choosing the correct flexure orientations. To see why this is important, we focus first on a simple flexural setup. Consider two basic singular mechanisms with the flexures oriented differently (Fig. 5.2(a),(b)). If the flexures were ideal pin joints, then in both cases, the force F would not cause any motion at all, i.e the two configurations would be infinitely stiff. If we perform a small motion finite element analysis (FEA) of the two configurations, we find that the stiffness in the first case is almost an order of magnitude more than the second. This result implies that it is advantageous to have the flexures oriented in such a manner that the force transmitted through them always points along their length. To utilize this knowledge of flexural hinges, we first need to find out the direction of the forces transmitted through the various flexures for the typical external forces acting on the mechanism. Fig. 5.1 shows the typical forces acting on the fourbar mechanism of the MFI. Here $\mathbf{F}_{wing}$ is the wing force acting on the output link of the fourbar and $\mathbf{F}_{act}$ is the actuator force acting on the input link. For this analysis, we make the following simplifying assumptions. First we assume that each flexure is an ideal pin joint with a torsional spring. Thus it is capable of transmitting both forces and moments. However, the transmitted forces are independent of the rotation of the flexure, while the transmitted moment follows directly from the rotation. Next, we assume that the links move quasi-statically,

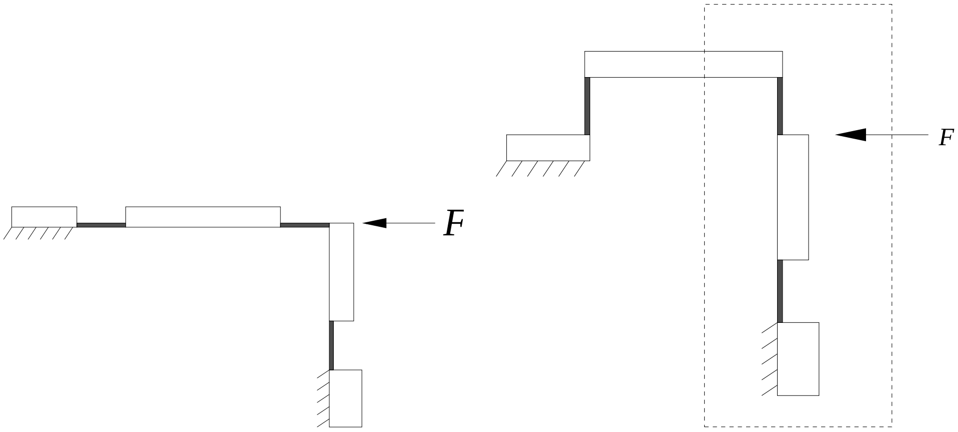

(a) (b)

Figure 5.2: FEA analysis of two simple flexural mechanisms.

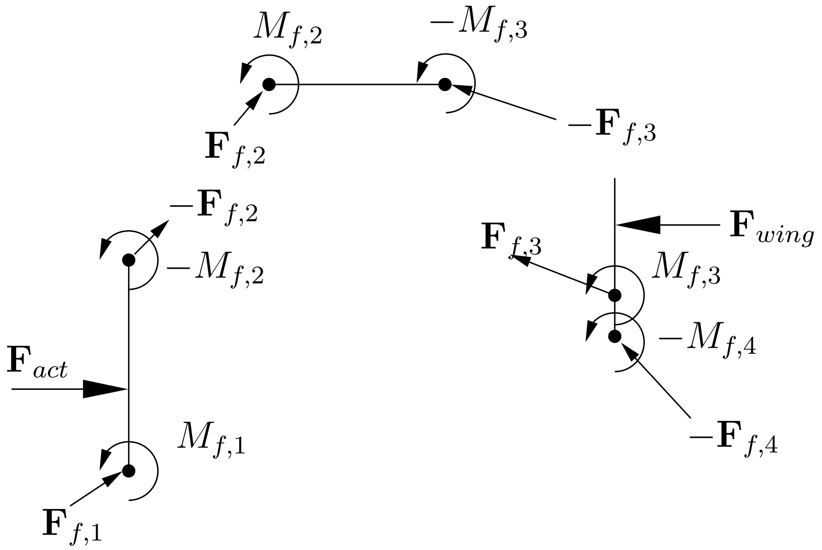

Figure 5.3: Exploded view of the fourbar links showing the flexure forces acting on the links

i.e., the links have no acceleration. This implies that given a fourbar configuration (specified by the link angles) and a force $\mathbf{F}_{wing}$ acting on the output link, we also need to also specify a unique blocking force $\mathbf{F}_{act}$ to retain the fourbar at the given configuration. Since we know the way in which the actuator is attached to the fourbar, we will assume that the direction of $\mathbf{F}_{act}$ is known relative to the input link. The problem statement therefore becomes: Given a force $\mathbf{F}_{wing}$ acting on the output link of the fourbar, find the four vector forces transmitted through the fourbar flexures and the magnitude of the required blocking force $\mathbf{F}_{act}$. Thus we need to solve for 9 unknown quantities.

Fig. 5.3 shows an exploded view of the fourbar links showing the forces and moments acting on the various links. For our problem, we have to solve for the vectors $\mathbf{F}_{f,i}$, $i = 1, \ldots 4$ and the scalar, $|\mathbf{F}_{act}|$. $\mathbf{F}_{f,i}$ here represents the force transmitted via the i^{th} flexure from the $(i-1)^{th}$ to the i^{th} link. Similarly, $M_{f,i}$ represents the moment transmitted to the i^{th} link via the flexure connecting it to the $(i-1)^{th}$ link. The forces and moments have to satisfy the following equilibrium equations for each of the link they act upon:

$$\begin{aligned} \mathbf{F}_{f,i} - \mathbf{F}_{f,i+1} + \mathbf{F}^{i}_{ext} &= 0 \qquad (5.1) \\ \begin{pmatrix} \mathbf{F}_{f,i} \times r^{i}_{1} - \mathbf{F}_{f,i+1} \times r^{i}_{2} \\ +M_{f,i} - M_{f,i+1} + M^{i}_{ext} \end{pmatrix} &= 0 \qquad (5.2) \end{aligned}$$

$$i = 1, \ldots, 3$$

Thus there are 9 scalar equilibrium equations involving 9 unknowns.

In the above equation r^{i}_{1} and r^{i}_{2} are the moment arms of $\mathbf{F}_{f,i}$ and $-\mathbf{F}_{f,i+1}$ about the center of gravity (CG) of the i^{th} link. Note that we can simplify the solution method of (5.1) and (5.2) by proceeding with link 2 which has no external forces acting on it. This solution method for fourbars is well-known (see [Carricato 01] for example) and will not be further elaborated upon here. See Here we present the final results of the force analysis. Fig. 5.4 shows the forces transmitted through the various flexures super-imposed on the fourbar geometry for various configurations. These forces were calculated in response to a constant force $\mathbf{F}_{wing}$ acting normal to the output link of the fourbar for all these configurations.

Fig. 5.5 shows how the transmitted flexural forces vary with the configuration of the fourbar. At the extremes, where the fourbar exhibits "stiffening" in the actuator coordinates, we see that we require a much larger $\mathbf{F}_{act}$ to balance the same wing force $\mathbf{F}_{wing}$. This analysis tells us the direction in which the forces are transmitted via the various flexures. This provides us the best way to orient the various flexures in the

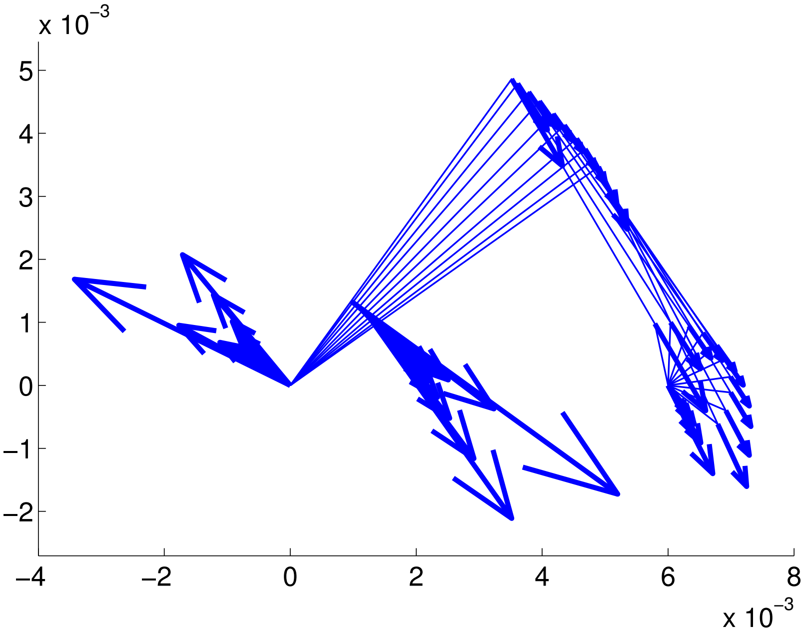

Figure 5.4: Forces transmitted through the fourbar flexures

fourbar during fabrication for the most efficient force transmission. Combined with various fabrication limitations, this gives the fabricated configuration of our latest fourbar as shown in Fig. 5.6. Note how all the flexures are oriented to be along the mean direction of the transmitted forces. We have experimentally measured the serial stiffness of the optimized fourbar mechanism and found it to be well over 4000 N/m. This is a huge improvement from the serial stiffness of previous fourbars which had a measured serial stiffness of about 1000 N/m.

5.2 Buckling strength of the flexures

The force analysis of the fourbar also allows us to calculate the maximum forces which can be transmitted through it. Alternatively, it allows us to design the fourbar

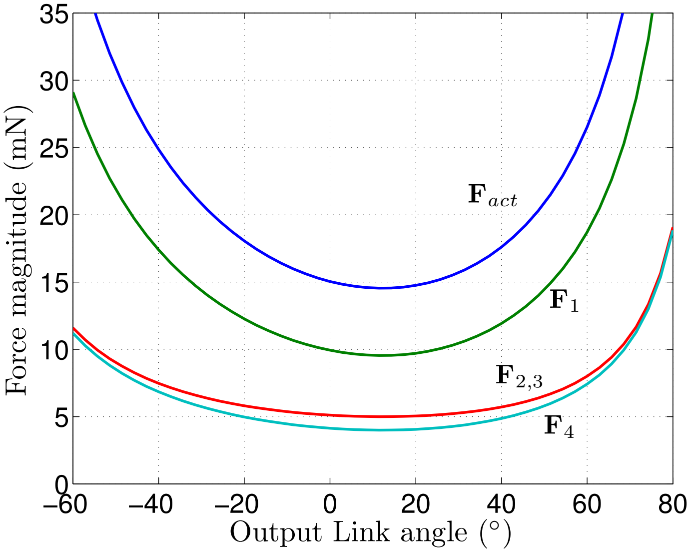

Figure 5.5: Variation of transmitted Flexural Forces

flexures to match a given maximum force which needs to be blocked by the actuator. For the MFI, the maximum blocking force of the actuator is about 100mN. This allows us to calculate the maximum forces being transmitted through the various flexures. Using the previous analysis, we find that $|\mathbf{F}_1| = 65$mN, $|\mathbf{F}_2| = |\mathbf{F}_3| = 35$mN and $|\mathbf{F}_4| = 27$mN for $|\mathbf{F}_{act}| = 100$mN. This force configuration is able to withstand a aerodynamic force of 7mN applied at the centroid of the wing.

We want to design the flexures to not buckle under these kinds of loads. The maximum force which a flexure of length l can withstand before buckling is given by

$$F_{cr} = \frac{EI\pi^2}{l^2}, \tag{5.3}$$

where E is the Young's modulus, I is the moment of area and l is the length. In practice, we will design with a factor of safety of 5 since the flexures are not always exactly parallel to the direction of the transmitted force. For our flexures, fabrication

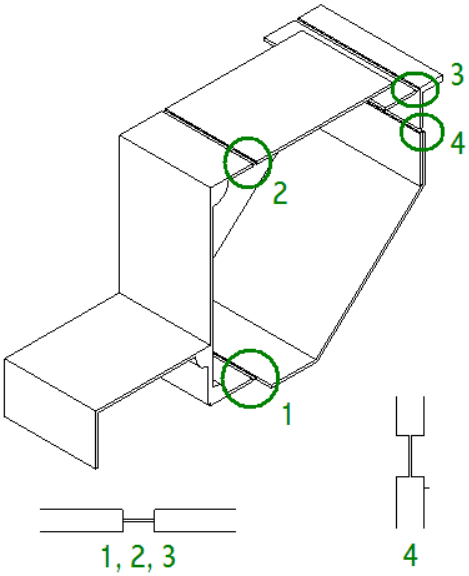

Figure 5.6: Latest MFI Fourbar design

constraints restrict us to flexure lengths of 125μm or greater and a thickness of either 12.5μm or 6.25μm. Since a 12.5μm flexure 125μm long cannot be used in the 3^{rd} and 4^{th} joints of the fourbar because the of the large fourbar motions, this puts yet another constraint on the allowable dimensions of the flexures. Taking all these factors into account, we finally arrive at the following flexure dimensions:

	1	2	3	4
l (μm)	125	125	125	125
w (mm)	3	3	4	4
t (μm)	6.25	6.25	12.5	12.5

5.3 Calculation of parallel stiffness

The parallel stiffness of a flexural mechanism is easy to calculate if we assume that each flexure is an ideal rotational joint with a constant rotational stiffness. For small rotational angles, the rotational stiffness of a flexure is given as

$$k_{flex} = \frac{EI}{l} \tag{5.4}$$

In an N-link mechanism, the total PE stored in the flexures of the mechanism is given by:

$$PE_{tot} = \sum_{i=1}^{N} 1/2 k_i \gamma_i^2 \tag{5.5}$$

where k_i is the stiffness of the i^{th} flexure calculated using (5.4) and γ_i is the total deflection of the i^{th} flexure. To find the rotational stiffness of the mechanism with respect to the driving actuation angle, call it α, we need to first find the restoring force for a given value of α. This is given by the gradient of the PE as:

$$\begin{aligned} F &= \frac{\partial PE}{\partial \alpha} \\ &= \sum_{i=1}^{N} k_i \gamma_i \frac{\partial \gamma_i}{\partial \alpha} \end{aligned} \tag{5.6}$$

For small displacements about some nominal value of $\alpha = \alpha_0$, the stiffness of the mechanism is given as:

$$\begin{aligned} k_{eq} &= \left.\frac{\partial F}{\partial \alpha}\right|_{\alpha=\alpha_0} \\ &= \sum_{i=1}^{N} k_i \left(\frac{\partial \gamma_i}{\partial \alpha}\right)^2 + k_i \gamma_i \frac{\partial^2 \gamma_i}{\partial \alpha^2} \end{aligned} \tag{5.7}$$

Note that it doesn't make sense to use a stiffness number for large motions. For the complete non-linear dynamics, we should directly use the value of the restoring force F according to (5.6).

5.3.1 Effect of flexure pre-stress

Note that in (5.7), γ_i represents the *total* displacement of the flexure from its strain-free state. This displacement depends not just on the kinematics of the mechanism but also on the fabrication method, which might impart a pre-stress to some of the flexures without any driving actuation. In other words, γ_i in (5.7) can be thought of as:

$$\gamma_i = \gamma_i^{\text{kin}} + \gamma_i^{\text{fab}} \tag{5.8}$$

Here, $\gamma_i^{\text{kin}} = 0$ when the driving angle $\alpha = 0$ and γ_i^{fab} is the pre-stress in the joint which results from fabrication. Note that γ^ifab is a constant for a given fabricated part. Since

$$\frac{\partial \gamma_i}{\partial \alpha} = \frac{\gamma_i^{\text{kin}}}{\partial \alpha},$$

the first term in (5.7) depends purely on the kinematics and not on the initial pre-stress due to fabrication. Thus, we need to take the initial pre-stress of the flexure into consideration only for those flexures for which we have

$$\frac{\partial^2 \gamma_i}{\partial \alpha^2} \neq 0,$$

about the nominal operating point.

We can see the effect of pre-stressing on the differential stiffness in Fig. 5.7. There is almost a 100% increase in the differential stiffness when the θ_y flexure is pre-stressed by 90°. To minimize the effect of flexure pre-stress, we have found that its usually a good idea to “cure” the whole mechanism at a heightened temperature after the fabrication is complete.

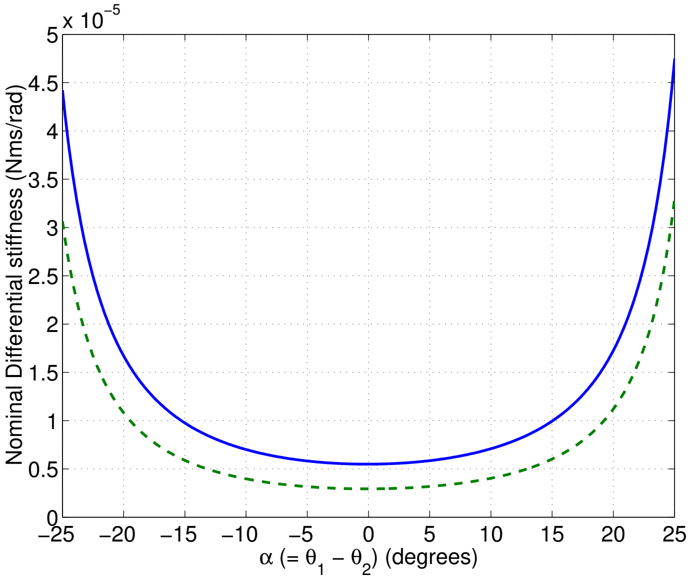

Figure 5.7: Effect of flexure pre-stress. The solid line represents the stiffness of the differential w.r.t α when $\theta_y^0 = 0°$ and the dotted line represents the stiffness with $\theta_y^0 = 90°$.

5.3.2 Effect of misalignment

Detailed geometric analysis turns out to be extremely important in mechanisms where certain geometric constraints need to be met for the mechanism to move.

Consider the wing differential mechanism of the MFI shown in Fig. 2.8. It consists of two links labeled 1 and 4 which are actuated independently via two fourbars. They are connected together by a series of 3 links which are interconnected by simple flexural elements. The basic idea is that when the links 1 and 4 are moved in phase, then the middle plate 2 rotates along with them about their common axis Z. However, when 1 and 4 move out of phase, the link 4 in addition to rotating about Z also rotates about the other axes X, Y and W.

The kinematics of the differential in the absence of any misalignments has already been derived in previous work [Avadhanula 02] as

$$\theta_x = \sin^{-1}(\lambda \sin \alpha) \tag{5.9}$$

$$\theta_y = \beta - \cos^{-1}(\lambda \sin \beta) \tag{5.10}$$

where $\beta = \tan^{-1}(\frac{1}{\lambda \cos \alpha})$

To emphasize the importance of alignment in the differential mechanism, it is appropriate to step back and start from one of the most simplistic concerns of kinematics, namely to find the available degrees of freedom in the mechanism. If we simply "count" the number of degrees of freedom in the mechanism using Gruebler's criterion:

$$\begin{aligned} N_{\text{diff}} &= 6 \times N_{\text{links}} - 5 \times N_{\text{flexures}} \\ &= 6 \times 4 - 5 \times 5 \\ N_{\text{diff}} &= -1 \end{aligned} \tag{5.11}$$

What this means is that an arbitrary closed 4 linked (5 with ground link included) spatial mechanism with flexures along arbitrary axes will be "jammed". In the MFI differential, the two extra degrees of freedom come from two of the flexural constraints becoming redundant in the presence of geometric constraints.

Consider the purely kinematic diagram of the differential shown in Fig. 2.8. From a kinematic perspective, the mechanism would jam completely if the flexural axes represented by the axes θ_1, θ_2, θ_x, θ_y and θ_w were to not intersect exactly at the single point shown in the figure as the origin. In reality, the flexural compliance allows some movement albeit at the expense of added unwanted stiffness.

To ensure the kind of alignments we need, we utilized a fabrication design in which

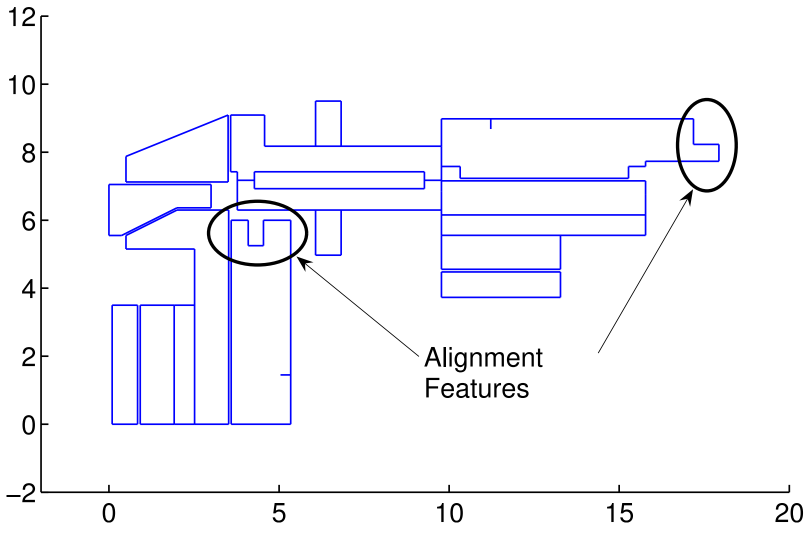

Figure 5.8: Cut pattern of differential on Carbon fiber. The dimensions are in mm.

the complete differential is cut out under the laser machine as a single part. Fig. 5.8 shows the final design of the differential cuts. The alignment is critical enough that we needed to account for the width of the laser beam which cuts out the pattern on the carbon fiber sheet. In addition to this, we also fabricated the output links of the fourbar links as part of the differential mechanism to ensure the alignment mentioned above. Features are added to the differential design which mate and thus ensure good alignment. The latest differential mechanism exhibits a parallel stiffness which is just 1.5-1.6 times the predicted stiffness with perfect alignment. This is quite a gain from previous designs which were almost 40-50 times the predicted stiffness.

5.4 Conclusions

To summarize, we need to account for the following factors while designing a flexural mechanism using the new carbon fiber fabrication techniques:

- Analyze the forces transmitted through the flexures in the fourbar and design the flexures to always point in the direction of the transmitted forces.
- For flexural mechanisms, it is very important to design the flexures to never buckle under typical operating conditions.
- It is important to account for flexure pre-stressing in the calculation of mechanism stiffnesses.
- For 3D mechanisms where mobility arises from geometric constraints, it is important to analyze for the effect of misalignment and design the structure in a manner which ensures proper alignment.

Fig. 5.9 shows a photo of the latest MFI thorax mechanism which utilizes these various design rules in construction. For clarity, we also show the 3D sketch of the mechanism in Fig. 5.10.

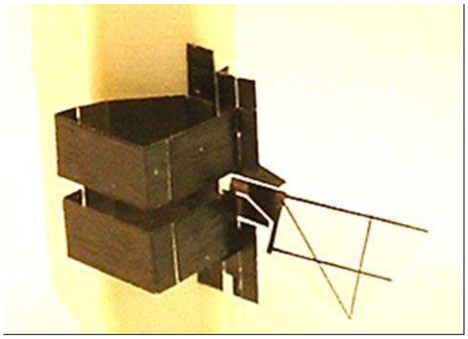

Figure 5.9: Photo of the latest MFI differential

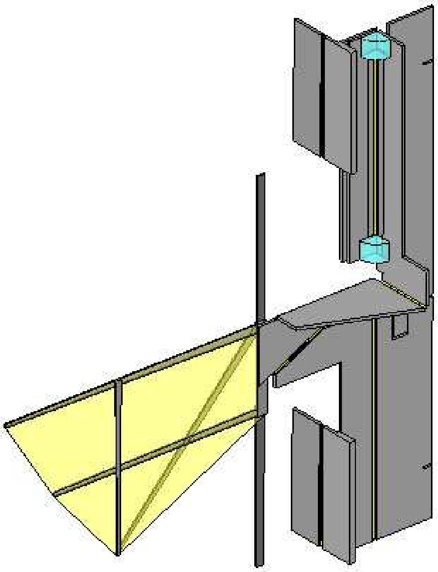

Figure 5.10: 3D sketch of the latest MFI differential. Apart from the matching spar and the wing, the entire part is made by folding up the planar cut file shown in Fig. 5.8.The quarter cylinders on the top spar represent cyano-acrylate glue to freeze the joint at 90°.

Chapter 6

Drive Strategy

This chapter describes the drive scheme used in the MFI. Since the primary aim of any drive strategy used in the MFI is a maximization of lift and other aerodynamic performance measures, we need to study in detail various periodic wing trajectories and their aerodynamic benefits. We study these issues in coordination with fundamental plant and actuator dynamic limits and motivate the reason for the choice of a simple sinusoidal drive scheme, which we then describe in detail. Finally, some very encouraging results from the latest single wing structure are presented which validate the claim made that simple sinusoidal inputs are more than adequate for good lift production.

6.1 Background and Motivation

Even before choosing a control strategy, we first need to examine closely the fundamental aspects of the plant dynamics and the underlying motivation for the control. In our case, the following facts about the plant and actuator dynamics and the final aim of the control endeavour will inform our efforts:

Actuator Force Saturation The most important aspect of our plant is the severe actuator saturation present in our plant as compared to typical feedback control problems. The PZT unimorph actuators which we use are typically limited to voltages of about 200V. For this input actuation, they typically produce forces of around 200mN (with no displacement). If left free to move, they typically move around 400-500 microns at this voltage. Beyond this voltage, the actuators saturate, i.e, they do not produce any additional force or displacement. Beyond about 300V or so, there is a risk of electrical breakdown across the PZT plate.

Actuator Dynamics The PZT unimorph actuators are used in a bending mode. Upto their first bending resonance modes, they behave well, but they rapidly begin to exhibit undesirable bending modes beyond their first bending resonance.

Poor behavior at high frequencies We also wish to avoid exciting high frequency oscillatory modes which arise if we actuate the complete system beyond about 1000Hz or so. Thus any allowable control system must restrict itself to producing actuations with frequency content below 1000Hz.

Periodic Motions For our control problem, we are only interested in tracking or following periodic trajectories in the range 200Hz-300Hz. Since the plant is not chaotic or naturally unstable, this implies that the input has to be periodic as well with the same base frequency as the output period we are trying to achieve.

Lift maximization Finally, we are interested more in the overall lift production rather than the exact trajectory used to generate this lift. In other words, if two different trajectories produce equal lifts, we do not differentiate between them. As a long term problem, we will need to analyze different trajectories for their efficiencies. However, for now, we restrict ourselves to only considering the overall lift production.

These considerations allow us to write the following "constraints" on the space of allowable inputs.

$$|u(t)| < u_{max} \quad \forall t \tag{6.1}$$

This ensures that we never saturate the actuators. The condition that the output and input are periodic implies that if we want to achieve an output period of ω, then the input has to contain only frequencies at ω, 2ω, 3ω etc[1]. In other words, $u(t)$ has to be of the form:

$$|u(t)| < u_{max} \quad \forall t \tag{6.2}$$

Since we are interested in base frequencies of up-to 250Hz, we need to additionally restrict the components of $u(t)$ to ≤ 750Hz in order not to excite undesirable structural resonances. This means that $u(t)$ in fact needs to be expressible as:

$$u(t) = u_1 \sin \omega t + u_2 \sin 2\omega t + u_3 \cos 2\omega t + u_4 \sin 3\omega t + u_5 \cos 3\omega t \tag{6.3}$$

---

[1] Note that the nonlinearity of the plant implies that we could generate an output at ω with an input of $\omega/2$ or $\omega/3$ etc. However, this is an *extremely* inefficient way to generate an output at ω and we will ignore this scenario for now.

We can thus represent the set of all allowable inputs by a vector $\mathbf{u} = \{u_1, \ldots u_5\}$ which satisfy (6.2). Let us define $g(\mathbf{u})$ as the $\mathcal{L}_\infty$ norm of $u(t)$ corresponding to $\mathbf{u}$.

$$g(\mathbf{u}) = \max_t u(t) \tag{6.4}$$

where $u(t)$ is formed using the components of $\mathbf{u}$.

Let us define the constrained 6-D space $\mathcal{P}_u$ as

$$\mathcal{P}_u = \{\mathbf{u} : g(\mathbf{u}) \leq u_{max} \quad \forall t\} \tag{6.5}$$

The problem which we desire to solve then is to search over $\mathcal{P}_u$ for the trajectory which maximizes lift production.

For the purposes of analysing the efficacy of various drives, we will for now also completely ignore the differential dynamics and assume that we have some sort of "perfect" differential which allows the two fourbar motions to be completely dynamically uncoupled and acts purely kinematically to produce flapping and rotation from the two fourbar outputs. In other words, we will use the method shown in Fig. 6.1 to calculate the lift force generated for a given input trajectory $u(t)$.

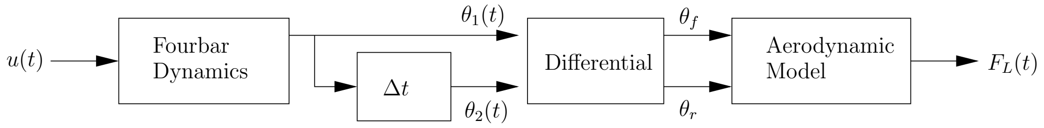

Figure 6.1: Simplified model for calculating mean lift. In this figure, $\theta_f(t)$ represents the flapping angle of the wing, or the angle made by the leading spar. θ_r represents the rotation angle of the wing. These are equivalent to angles θ_2 and θ_x in Fig. 2.8.

The fourbar dynamics are assumed to be those given by (4.4). The aerodynamic model is given by (3.34). Let us define $\bar{F}_L(\mathbf{u})$ as the mean lift over a cycle for the input formed from $\mathbf{u}$.

Problem Statement

The "problem statement" for choosing the drive strategy therefore, is

$$\max_{\mathbf{u} \in \mathcal{P}_u} \bar{F}_L(\mathbf{u}) \tag{6.6}$$

In other words, we wish to find the input $u(t)$ which gives the maximum mean lift over a cycle.

6.1.1 Cost / Benefit Analysis

Before doing any optimization on the input space $\mathcal{P}_u$, we first consider a number of trajectories which are of the form (6.3) without imposing the constraint (6.2). In other words, we consider the case of no actuator saturation. The aim here is to manually sample various "points" in $\mathcal{P}_u$ and evaluate them on the basis of the lift production and the cost in the needed actuation. Note that many of the trajectories shown here will not lie in $\mathcal{P}_u$ as we will see. In the descriptions below, $\theta_{t,i}$ and $\theta_{b,i}$ represent the motions of the top and bottom spars of the differential (equivalent to θ_2 and θ_1 respectively in Fig. 2.8) for the i^{th} trajectory. $\theta_{r,i}$ represents the rotation (θ_x in Fig. 2.8) of the wing. T_{diff} represents the relationship between $\alpha = \theta_1 - \theta_2$ and the wing rotation θ_x and is given by (2.29).

Case 1 First we consider the best case scenario (aerodynamically). The flapping is forced to be a smoothened triangular wave while the rotation is forced to be a smoothened square wave. In this case, the angles are given by:

$$\theta_{t,1}(t) = \theta_0\left(\cos\omega t + 1/9\cos 3\omega t\right) \tag{6.7}$$

$$\theta_{r,1}(t) = \theta_{r,0}\left(\sin\omega t + 1/9\sin 3\omega t\right) \tag{6.8}$$

$$\theta_{b,1}(t) = \theta_{t,1}(t) + T_{\text{diff}}^{-1}(\theta_{r,1}(t)) \tag{6.9}$$

Note that in this case, the torques required to drive the leading and lagging spars are unequal because $\theta_{t,1}(t) \neq \theta_{b,1}(t-\eta)\forall\eta$. In other words, the top and bottom spar trajectories are not just different phases of the same trajectory.

Case 2 Next we consider a slight variation of Case 1, where instead of directly forcing the rotation to be a certain trajectory, we assume that the top and bottom spars are the same trajectory, but offset in time. In other words, we use

$$\theta_{t,2}(t) = \theta_0\left(\cos\omega t + 1/9\cos 3\omega t\right) \tag{6.10}$$

$$\theta_{b,2}(t) = \theta_{t,2}(t - 2\frac{20}{180\omega}) \tag{6.11}$$

$$\theta_{r,2}(t) = T_{\text{diff}}(\theta_{b,2}(t) - \theta_{t,2}(t)) \tag{6.12}$$

In other words, $\theta_{b,2}(t)$ is $\theta_{t,2}(t)$ delayed by 20° phase.

Case 3 In this case, we force the flapping and rotations to be pure sinusoids.

$$\theta_{t,3}(t) = \theta_0\cos\omega t \tag{6.13}$$

$$\theta_{r,3}(t) = \theta_{r,0}\sin\omega t \tag{6.14}$$

$$\theta_{b,3}(t) = \theta_{t,3} + T_{\text{diff}}^{-1}(\theta_{r,3}(t)) \tag{6.15}$$

Like in Case 1, the torques for the top and bottom spars are unequal because the trajectories of the spars are not just different in phase.

Case 4 In this case, we use the same sinusoidal trajectory for both the top and bottom spars but delay them in phase to get rotation.

$$\theta_{t,4}(t) = \theta_0 \cos\omega t \tag{6.16}$$

$$\theta_{b,4}(t) = \theta_{t,4}(t - 2\frac{20}{180\omega}) \tag{6.17}$$

$$\theta_{r,4}(t) = T_{\text{diff}}(\theta_{b,4}(t) - \theta_{t,4}(t)) \tag{6.18}$$

In this case, we will have the same torques on both the top and bottom spars but delayed in phase.

Case 5 Lastly, instead of actively trying to achieve any specific trajectory, we just use simple sinusoidal drives on the two actuators and let the dynamics of the system take them into a periodic trajectory. We drive the two actuators out of phase and generate the rotation from the difference of the two fourbar outputs.

$$u_{t,5}(t) = u_0 \cos\omega t \tag{6.19}$$

$$u_{b,5}(t) = u_0 \cos\omega(t - t_u) \tag{6.20}$$

We then solve the dynamics of the fourbar to get the trajectories of the top and bottom spars of the fourbar. These trajectories will in general, have higher harmonic content due to the nonlinearities in the fourbar. We note that since we are assuming no coupling, the top and bottom spar trajectories will be related by

$$\theta_{b,5}(t) = \theta_{t,5}(t - t_u) \tag{6.21}$$

and the wing rotation follows as:

$$\theta_{r,5} = T_{\text{diff}}(\theta_{b,5}(t) - \theta_{t,5}(t)) \tag{6.22}$$

Parameter	**Value**	**Units**
J	$22{\times}10^{-12}$	kg-m^2
k_0	4.2×10^{-5}	N-m/rad
a	0.38	–
B_1	2.6×10^{-9}	Nms/rad
B_2	8.8×10^{-12}	Nms^2/rad^2
b	0.43	–
T_i	2×10^{-7}	Nm/V

Table 6.1: Parameters of system used to perform cost analysis

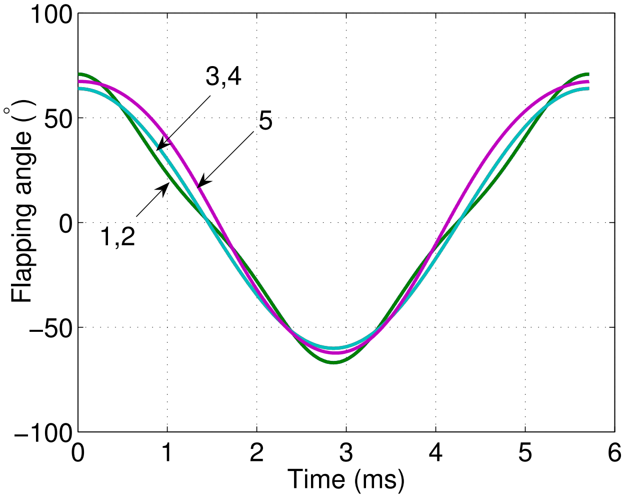

Figure 6.2: Comparison of flapping angle obtained in the five trajectories

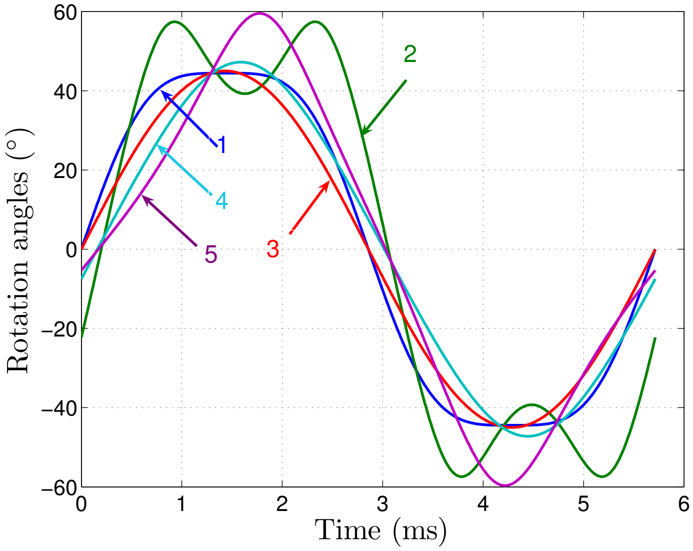

Figure 6.3: Comparison of rotations obtained with the four trajectories

Fig. 6.2 shows a comparison of the various flapping trajectories obtained in the various cases and Fig. 6.3 shows a comparison of the rotations obtained in the various cases. Fig. 6.4 shows a comparison of the lift forces obtained in the various cases. The mean lift in the various cases is also enumerated in Table 6.2. We see that in all these cases, the mean lift obtained does not vary too much. The highest lift which we obtain in the expected case of symmetric wing rotation with a smooth triangular flapping and a smooth square wave rotation is only 6% higher than in the case of just purely passively driving the fourbars.

Trajectory	1	2	3	4	5
Mean lift (μN)	919.4414	781.7782	829.9382	785.8688	866.5127
Required Actuator Voltage (V)	1110	1110	240	240	220

Table 6.2: Mean lift obtained by various trajectories

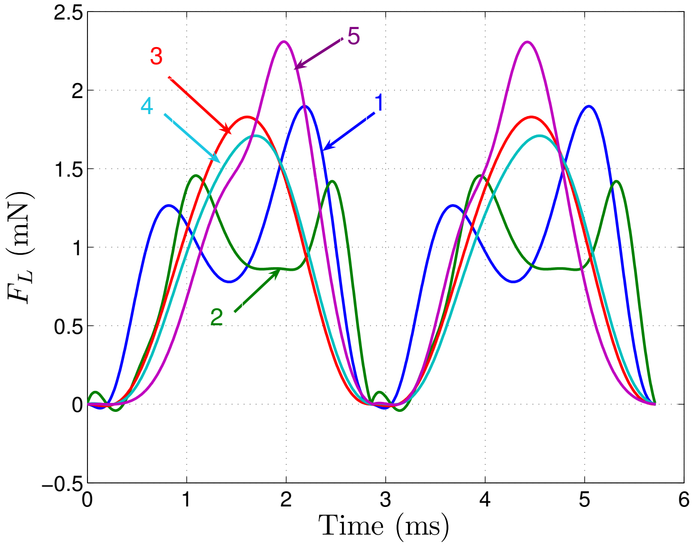

Figure 6.4: Comparison of lift forces obtained from various trajectories

Fig. 6.5 shows the voltage required to drive the actuators to generate the trajectory in each of these cases. These torques were computed by simply substituting $\theta(t)$ into (4.4) to calculate $u(t)$. Clearly, for trajectories 1 and 2 we are well above the available force limits of the actuator. The meagre 6% increase in lift comes at the cost of a five-fold increase in the required input actuation.

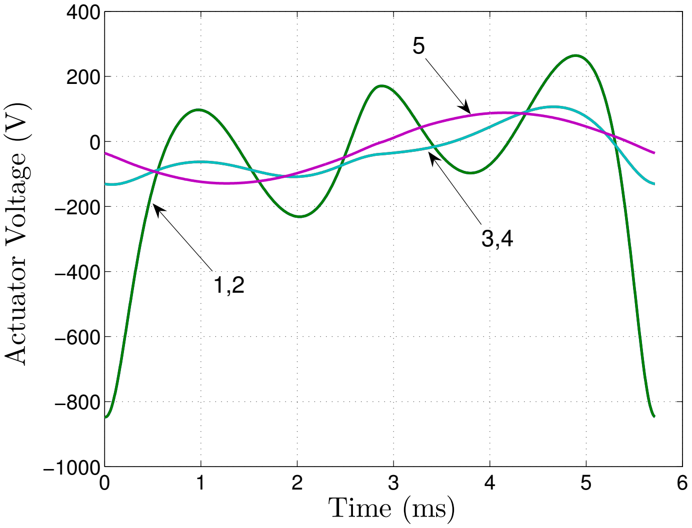

Figure 6.5: Comparison of input voltages required for various trajectories

This analysis presents a convincing case for higher harmonic content not being necessary in the output waveforms.

6.1.2 Local Perturbation Analysis

The previous section informs us that aggressively trying to control third harmonic output motion costs too much in terms of the needed actuator forces and that in fact the passive trajectory obtained from the passive fourbar dynamics is just as good. The insight gained from this is that sinusoidal output trajectories are at least from the lift production sense, quite adequate. Thus, if the actuator saturation dictates a given maximum input voltage u_{max}, we restrict ourselves to a simple sinusoidal input trajectory of the form:

$$u_s(t) = u_{max} \sin \omega t \tag{6.23}$$

This corresponds to $\mathbf{u}_s = \{u_{max}, 0, 0, 0, 0\} \in \mathcal{P}_u$. Note that $\mathbf{u}_s$ lies on the boundary of $\mathcal{P}_u$. In this section, we do a local perturbation analysis and try to find out if there are any locally better trajectories which yield better lift while still staying within $\mathcal{P}_u$. It is clear that locally, the best trajectory will still be on the boundary of $\mathcal{P}_u$. Thus to achieve better lift, we will need to move on the boundary of $\mathcal{P}_u$ in the direction of increasing lift till we achieve maximal lift. To be more precise, we want:

$$\max_{g(\mathbf{u})=u_{max}} \bar{F}_L(\mathbf{u}) \tag{6.24}$$

To get an estimate of how optimal $\mathbf{u}_s$ is for the above maximization, we need to see how collinear the local gradients of $g(\mathbf{u})$ and $\bar{F}_L(\mathbf{u})$ are at $\mathbf{u} = \mathbf{u}_s$, since we know that at the extremum the normals to the constraint function and the objective function are collinear.

Numerically estimating the local gradients for the system parameters given in Table 6.1 and $u_{max} = 80$ gives:

$$\mathbf{n}_F(\mathbf{u}_s) = \left.\frac{\partial F_L(\mathbf{u})}{\partial \mathbf{u}}\right|_{\mathbf{u}=\mathbf{u}_s} = \{0.93, 0.30, 0.05, -0.10, 0.04\}^T \tag{6.25}$$

$$\mathbf{n}_g(\mathbf{u}_s) = \left.\frac{\partial g(\mathbf{u})}{\partial \mathbf{u}}\right|_{\mathbf{u}=\mathbf{u}_s} = \{0.70, 0.09, 0.00, -0.69, 0.18\}^T \tag{6.26}$$

We can see immediately that $\mathbf{u}_s$ is not completely optimal since $\mathbf{n}_F$ and $\mathbf{n}_g$ are not collinear.

As a first attempt in finding a locally optimal trajectory, we first approximate the constraint function $g(\mathbf{u})$ and the objective function $\bar{F}_L(\mathbf{u})$ as quadratic functions and then use the Lagrange multiplier technique to do an analytical maximization. In other words, we can approximate

$$\bar{F}_L(\mathbf{u}_s + \Delta\mathbf{u}) = \bar{F}_L(\mathbf{u}_s) + \mathbf{n}_F^T \Delta\mathbf{u} + \Delta\mathbf{u}^T H_F \Delta\mathbf{u} \tag{6.27}$$

$$g(\mathbf{u}_s + \Delta\mathbf{u}) = g(\mathbf{u}_s) + \mathbf{n}_g^T \Delta\mathbf{u} + \Delta\mathbf{u}^T H_g \Delta\mathbf{u} \tag{6.28}$$

where $\mathbf{n}_F$ is the local gradient of $\bar{F}_L(\mathbf{u})$ at $\mathbf{u}_s$:

$$\mathbf{n}_F = \left.\frac{\partial F_L(\mathbf{u})}{\partial \mathbf{u}}\right|_{\mathbf{u}=\mathbf{u}_s} \tag{6.29}$$

and H_F is the hessian of $\bar{F}_L$ at $\mathbf{u}_s$:

$$H_F = \left.\frac{\partial^2 F_L(\mathbf{u})}{\partial \mathbf{u}^2}\right|_{\mathbf{u}=\mathbf{u}_s} \tag{6.30}$$

If these approximations were numerically stable, we could have obtained the local extremum by simply solving the Lagrange multiplier problem:

$$\mathbf{n}_F + H_F \Delta\mathbf{u} + \lambda \left(\mathbf{n}_g + H_g \Delta\mathbf{u}\right) = 0 \tag{6.31}$$

$$\mathbf{n}_g^T \Delta\mathbf{u} + \Delta\mathbf{u}^T H_g \Delta\mathbf{u} = 0 \tag{6.32}$$

Unfortunately, it turns out that the constraint function $g(\mathbf{u})$ is highly nonlinear in the neighborhood of $\mathbf{u}_s$. In fact, locally it turns out that $H_g(\mathbf{u}_s)$ is actually rank deficient although higher order derivatives of $g(\mathbf{u})$ in the neighborhood of $\mathbf{u}_s$ are quite large. This makes it impossible to use a local quadratic approximation.

A brute force approach of just sampling a grid of points in the neighborhood of $\mathbf{u}_s$ is also too expensive to be feasible since each call to $\bar{F}_L$ involves solving a nonlinear ODE. This forces us to consider a somewhat restricted subspace of $\mathbf{u}$ around $\mathbf{u}_s$ which will be more tractable. Looking at the values of $\mathbf{n}_F(\mathbf{u}_s)$ and $\mathbf{n}_g(\mathbf{u}_s)$ we see that varying the $\mathbf{u}_1$ and $\mathbf{u}_2$ components has the largest effect on $\bar{F}_L$. We therefore restrict ourselves to optimizing $\bar{F}_L$ purely with respect to $\mathbf{u}_1$ and $\mathbf{u}_2$. In other words, we restrict ourselves to a $\mathcal{P}_r \subset \mathcal{P}$ which is defined as:

$$\mathcal{P}_r = \{\mathbf{u} : \mathbf{u} = (u_1, u_2, 0, 0, 0) \wedge \mathbf{u} \in \mathcal{P}_u\} \tag{6.33}$$

Once again, we know that the optimal $\mathbf{u}_r \in \mathcal{P}_r$ which optimizes the lift will be on the boundary of $\mathcal{P}_r$. However, the boundary of $\mathcal{P}_r$ is a simple 1-D subspace and in this restricted space, the optimization can be done along a line. Performing this optimization numerically yields the optimal $u(t)$ as

$$u(t) = 78 \sin \omega t + 5 \sin 2\omega t \tag{6.34}$$

which gives $\bar{F}_L$ around 1% higher than just $\mathbf{u}_s$. Thus even in the optimal search direction, we get a mere one percent increase by allowing for higher harmonics.

6.1.3 Power considerations

A natural concern which arises in driving the fourbar passively instead of trying to actively "kill" higher harmonic content is that there is aerodynamic power being wasted in the higher harmonics. However, the harmonics at the higher frequencies have such little amplitude that they barely affect the power into the wing. To see this, we simulate the system given by (4.4) with the parameters given in Table. 6.1, and we get an output of the form:

$$\theta(t) = \sum_{k=0}^{k=3} \theta_{0,k} \sin(k\omega t + \phi_k) \tag{6.35}$$

The amplitudes of the output harmonics at the various harmonics ($\theta_{0,k}$) are given in Table. 6.3. If we assume somewhat simplistically that the power calculation remains constant across all frequencies and is given by:

$$P_{out} = \frac{1}{T}\int_0^T (B_1\dot{\theta} + B_2\dot{\theta}|\dot{\theta}|)\dot{\theta}dt \tag{6.36}$$

$$= \frac{1}{2}(B_1 + B_2\frac{8}{3\pi}\theta_0\omega)\theta_0^2\omega^2 \tag{6.37}$$

then the power in the various harmonics can be calculated to be as shown in Table 6.3.

Harmonic	$\theta_0(^\circ)$	$\frac{\omega}{2\pi}$ (Hz)	$\frac{1}{2}B_1(\theta_0\omega)^2$ (W)	$\frac{8}{6\pi}B_2(\theta_0\omega)^3$ (W)
1	67	175	2.15×10^{-3}	7.94×10^{-3}
2	5.21	350	5.24×10^{-5}	3.0×10^{-5}
3	1.15	525	5.69×10^{-6}	1.1×10^{-6}

Table 6.3: Power dissipated in higher harmonics

Thus we can effectively ignore the power going into the higher harmonic of the output. Thus although higher harmonics induced in the output do not buy us anything by way of increased lift, they also do not waste any of the available input power.

6.1.4 Experimental Validation

We also performed an experiment on a 1 DOF system to experimentally verify that it is indeed hard to to control higher harmonic content in the output. For this experiment, we aimed to simply remove the second harmonic content from the output of a 1 DOF fourbar, which should be an easier problem than controlling/removing third harmonic content. We generate input to the fourbar of the form:

$$u(t) = \text{Re}\left(u_0(e^{j\omega t} + \vec{r}e^{j2\omega t})\right) \tag{6.38}$$

where $\vec{r}$ is a complex vector which controls the relative phase and amplitude of the second harmonic of the input. For this input waveform, we will get an output of the form:

$$\theta(t) = \mathrm{Re}\left(\vec{\theta}_0(e^{j\omega t} + \vec{r}_{out}e^{j2\omega t})\right) \tag{6.39}$$

where $\vec{\theta}_0$ represents the relative amplitude and phase of the first harmonic of the output with respect to the input. $\vec{r}_{out}$ represents the relative magnitude and phase of the third harmonic of the output to the first harmonic of the input.

The problem statement is simply:

$$\min_{\vec{r}} |\vec{r}_{out}| \tag{6.40}$$

Since the complex number $\vec{r}$ can be considered a vector of length 2, this problem becomes a simple two dimensional optimization problem. The optimization was done by a simplified steepest descent algorithm[2]:

1. Begin with $\vec{r} = \vec{r}_0 = \vec{0}$.

2. Find the derivative of $|r_{out}|$ with respect to $\vec{r}$ by measuring the output second harmonic ratio for the following three input harmonics:

$$|\vec{r}_{out}|_1 \leftarrow \vec{r}_0 \tag{6.41}$$

$$|\vec{r}_{out}|_2 \leftarrow \vec{r}_0 + \delta r \tag{6.42}$$

$$|\vec{r}_{out}|_3 \leftarrow \vec{r}_0 + j\delta r \tag{6.43}$$

---

[2] Although in practice, it is not recommended to use the steepest descent algorithm to do optimization, it turns out to be the quickest optimization algorithm to prototype on this algorithm just to test the basic premise of how hard it is to remove/control higher harmonics.

Then the derivative is given by:

$$J \overset{\text{def}}{=} \frac{\partial|\vec{r}_{out}|}{\partial\vec{r}} = \frac{1}{\delta r}\begin{bmatrix}|\vec{r}_{out}|_2 - |\vec{r}_{out}|_1 \\ |\vec{r}_{out}|_3 - |\vec{r}_{out}|_1\end{bmatrix} \tag{6.44}$$

3. Perform a one dimensional optimization:

$$\min_{\lambda} \vec{r}_{out}(\vec{r}_0 + \lambda J) \tag{6.45}$$

In practice, we use the golden section search [Press 99] to find the optmimum, $\lambda^\star$.

4. Update $\vec{r} \leftarrow \vec{r} + \lambda^\star J$ and repeat from step 2.

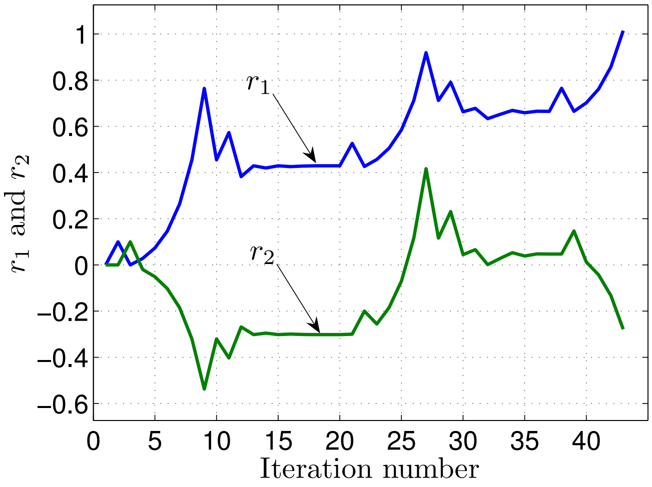

Figure 6.6: Evolution of r_1 and r_2. r_1 and r_2 are the real and imaginary parts respectively of $\vec{r}$.

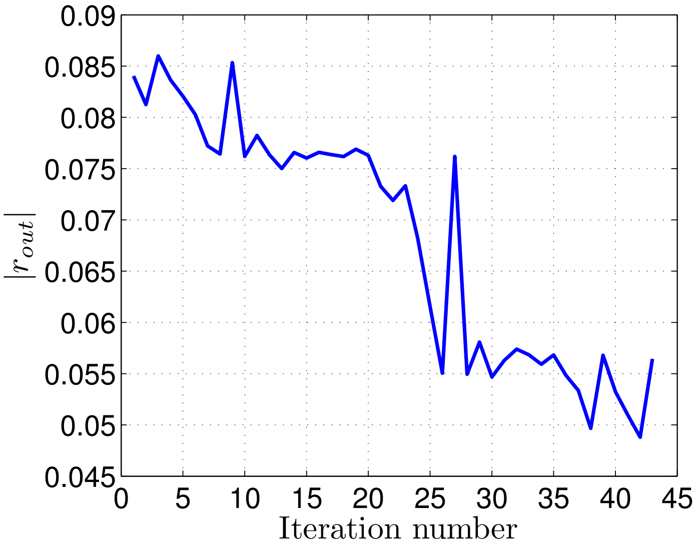

Figure 6.7: Evolution of $|\vec{r}_{out}|$.

Fig. 6.6 shows the evolution of $\vec{r} = r_1 + jr_2$ as the optimization progresses. The periodic spikes are from the one dimensional golden section search which keeps increasng the step size to quickly bound the minimum λ between two limits. Fig. 6.7 shows the evolution of $|\vec{r}_{out}|$. The experimental results indicate that to reduce the second harmonic content of the output from 8% of the base harmonic to 5%, we require a doubling of the input peak force. This indicates that it is hard in practice to control/eliminate the higher harmonics.

6.2 Description of Drive Scheme used

Now that we have shown that it is not particularly useful and even feasible to consider higher input harmonics, we need a drive scheme which has the simplifying constraint that the two inputs are simple sinusoidal inputs at the drive frequency.

This implies that the space of all possible drives to a 2 DOF wing structure can be described by the following parameters:

w	the drive frequency
$U_{dc,1}$, $U_{dc,2}$	the DC offset of the drive voltages of the two actuators
$U_{amp,1}$, $U_{amp,2}$	the amplitudes of the drive voltages of the two actuators at the drive frequency
φ_1, φ_2	the phases of the drive voltages at the drive frequency

This input space maps into an output space which can be described completely by the following parameters:

$\Theta_{dc,1}$, $\Theta_{dc,2}$	The mean position of the outputs of the fourbars (i.e, their DC positions).
$\Theta_{amp,1}$, $\Theta_{amp,2}$	The amplitudes of the harmonics of the output waveforms of the fourbars at the drive frequency.
γ_1, γ_2	The phases of the fourbar output harmonics at the drive frequency

We can think of this input output relationship as a complex two input two output map which takes the two complex numbers $(U_{dc,i} + U_{amp,i}e^{j\varphi_i})_{i=1,2}$ to the two complex numbers $(\Theta_{dc,i} + \Theta_{amp,i}e^{j\gamma_1})_{i=1,2}$. In order to simplify further analysis, let us define the complex numbers

$$\bar{U}_i \overset{\text{def}}{=} U_{dc,i} + U_{amp,i}e^{j\varphi_i}$$

$$\bar{\Theta}_i \overset{\text{def}}{=} \Theta_{dc,i} + \Theta_{amp,i}e^{j\gamma_i}$$

The 2 DOF plant dynamics can then be thought of as the following complex map:

$$F : \begin{bmatrix} \bar{U}_1 \\ \bar{U}_2 \end{bmatrix} \longrightarrow \begin{bmatrix} \bar{\Theta}_1 \\ \bar{\Theta}_2 \end{bmatrix} \tag{6.46}$$

The control problem is to find $(\bar{U}_1, \bar{U}_2)$ which maps to a desired $(\bar{\Theta}_1^d, \bar{\Theta}_2^d)$. This is a relatively simple function inversion problem. We first note the following properties about the desired $\bar{\Theta}_i^d$ and the mapping F:

- F is time invariant. In other words,

  $$F(\bar{U}_i e^{j\lambda}) = e^{j\lambda} F(\bar{U}_i) \tag{6.47}$$

  Since we are not interested in maintaining phase with respect to any external signal, we can therefore safely always drive with $\varphi_1 = 0$ and just vary φ_2.

- For the moment we are interested in wing trajectories which are symmetric in the upstroke and downstroke. For such trajectories, it is easy to see that we desire

  $$\Theta_{dc,1} = \Theta_{dc,2} \tag{6.48}$$

6.2.1 The Algorithm

Briefly, the control scheme works as follows:

1. We start with a guess of G_{fit} which maps $(\bar{U}_1, \bar{U}_2)$ to $(\bar{\Theta}_1, \bar{\Theta}_2)$. We find the inputs required to generate the desired shape of the output trajectory:

   $$\begin{bmatrix} \bar{U}_1 \\ \bar{U}_2 \end{bmatrix}_1 = G_{fit}^{-1} \begin{bmatrix} \bar{\Theta}_1^d \\ \bar{\Theta}_2^d \end{bmatrix} \tag{6.49}$$

   Since we are only interested in the "shape" of the input trajectory and we want to start with a small input amplitude, we scale the input in such a way that the maximum of the two inputs is U_{max}. Thus we transform the inputs to be applied as:

$$\begin{bmatrix} \bar{U}_1 \\ \bar{U}_2 \end{bmatrix} \leftarrow \begin{bmatrix} \bar{U}_1 \\ \bar{U}_2 \end{bmatrix} \frac{|\bar{U}_1|}{\bar{U}_1 \max\{|\bar{U}_1|, |\bar{U}_2|\}} U_{max} \tag{6.50}$$

In other words, we ensure that $\varphi_1 = 0$ and that $\max\{\bar{U}_1, \bar{U}_2\} = U_{max}$.

2. We apply the following three sets of input voltages to the plant:

$$\begin{bmatrix} \bar{U}_1 \\ \bar{U}_2 \end{bmatrix}_1 = \begin{bmatrix} \bar{U}_1 \\ \bar{U}_2 \end{bmatrix}$$
$$\begin{bmatrix} \bar{U}_1 \\ \bar{U}_2 \end{bmatrix}_2 = \begin{bmatrix} \bar{U}_1 \\ \bar{U}_2 e^{j\eta} \end{bmatrix}$$
$$\begin{bmatrix} \bar{U}_1 \\ \bar{U}_2 \end{bmatrix}_3 = \begin{bmatrix} \bar{U}_1 \\ \bar{U}_2 e^{-j\eta} \end{bmatrix}$$

and for each of these three inputs, we measure the output vectors

$$[\bar{\Theta}_1, \bar{\Theta}_2]_i, i = 1 \ldots 3$$

3. With these three sets of input, output measurement sets, we modify the estimate of G_{fit}. Since we assume that at every input "level", there is a transformation matrix G_{fit}, this means that we can write:

$$\begin{bmatrix} \bar{\Theta}_1 \\ \bar{\Theta}_2 \end{bmatrix}_i = \begin{bmatrix} G_{11} & G_{12} \\ G_{21} & G_{22} \end{bmatrix} \begin{bmatrix} \bar{U}_1 \\ \bar{U}_2 \end{bmatrix}_i \tag{6.51}$$

This can be re-written as:

$$\begin{bmatrix} \bar{\Theta}_1 \\ \bar{\Theta}_2 \end{bmatrix}_i = \begin{bmatrix} [\bar{U}_1 \quad \bar{U}_2]_i & 0 & 0 \\ 0 & 0 & [\bar{U}_1 \quad \bar{U}_2]_i \end{bmatrix} \begin{bmatrix} G_{11} \\ G_{12} \\ G_{21} \\ G_{22} \end{bmatrix} \tag{6.52}$$

We can stack these relationships for each of the three measurement sets and then find the elements of G_{fit} which "solve" the equation in a least square sense.

$$\begin{bmatrix} G_{11} \\ G_{12} \\ G_{21} \\ G_{22} \end{bmatrix} \approx \begin{bmatrix} [\bar{U}_1 \quad \bar{U}_2]_1 & 0 & 0 \\ [\bar{U}_1 \quad \bar{U}_2]_2 & 0 & 0 \\ [\bar{U}_1 \quad \bar{U}_2]_3 & 0 & 0 \\ 0 & 0 & [\bar{U}_1 \quad \bar{U}_2]_1 \\ 0 & 0 & [\bar{U}_1 \quad \bar{U}_2]_2 \\ 0 & 0 & [\bar{U}_1 \quad \bar{U}_2]_3 \end{bmatrix}^{\dagger} \begin{bmatrix} \begin{bmatrix} \bar{\Theta}_1 \\ \bar{\Theta}_2 \end{bmatrix}_1 \\ \begin{bmatrix} \bar{\Theta}_1 \\ \bar{\Theta}_2 \end{bmatrix}_2 \\ \begin{bmatrix} \bar{\Theta}_1 \\ \bar{\Theta}_2 \end{bmatrix}_3 \end{bmatrix} \tag{6.53}$$

where † represents the pseudo inverse[3].

4. We repeat steps 2 and 3 till the estimate of G_{fit} "settles" down sufficiently.

5. We then step up U_{max} and return to step 1.

6. We terminate when either $\max\{U_1, U_2\}$ becomes too high or we reach the desired $[\bar{\Theta}_1^d, \bar{\Theta}_2^d]$.

---

[3] In practice, we use the \ operator in MATLAB, i.e, x = A \ b.

6.3 Experimental Results

6.3.1 2 DOF structure 04-κ

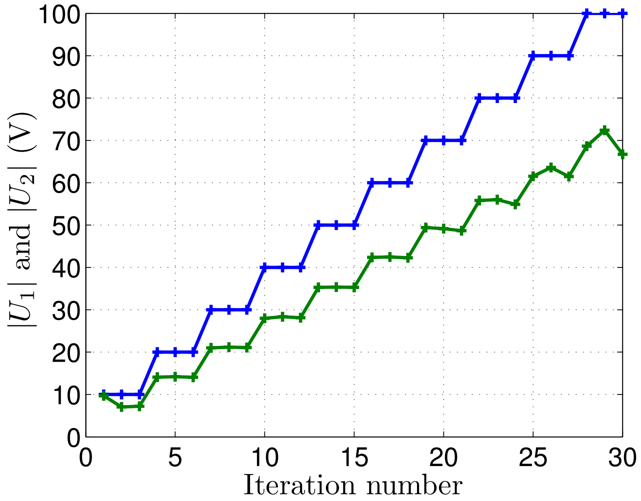

Figure 6.8: Evolution of $|U_1|$ and $|U_2|$

04-κ was a 2 DOF structure made in September 2004. The drive algorithm described in the previous section was used to calculate the drive voltages to be applied to the two actuators. Fig. 6.8 shows the "evolution" of $|\bar{U}_1|$ and $|\bar{U}_2|$ as the algorithm progresses. The flat regions are due to steps 2-4 of the drive scheme algorithm being repeated 3 times each. Fig. 6.9 shows the evolution of the output angles of the fourbar. As can be seen, we obtained nearly equal flapping angles for the two fourbar spars. The reason for $|\bar{U}_1| \neq |\bar{U}_2|$ is simply due to actuator mismatch. Fig. 6.10 shows a cartoon of how the wing trajectory would look like if we could view it along the direction of the leading spar of the wing. As can be seen, we get excellent flapping and rotation and rotational timing. However, this structure, due to actuator limitations was only able to do this at around 150Hz. This gives a calculated lift of around

$480\mu N$ and we in fact measured around $430\mu N$. Fig. 6.11 shows a snapshot video of the actual wing trajectory from the top view.

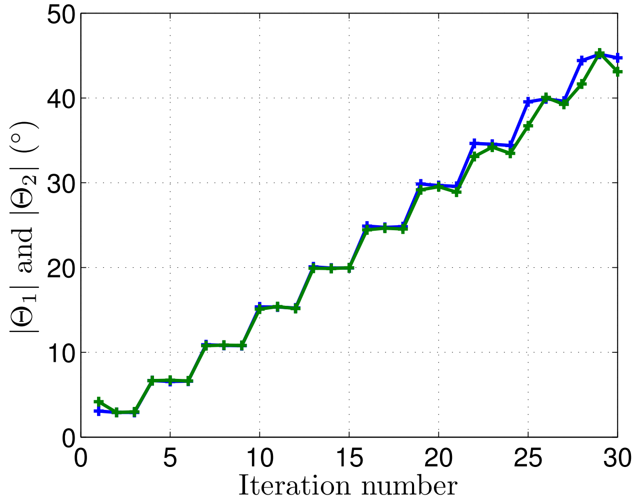

Figure 6.9: Evolution of $|\Theta_1|$ and $|\Theta_2|$

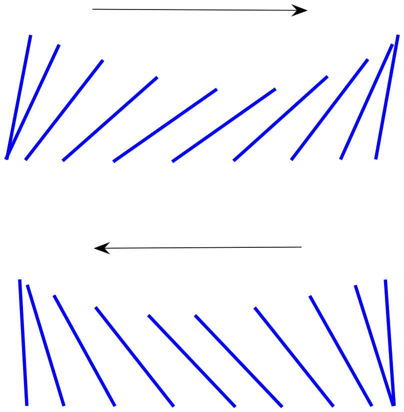

Figure 6.10: Final wing trajectory of 04-κ

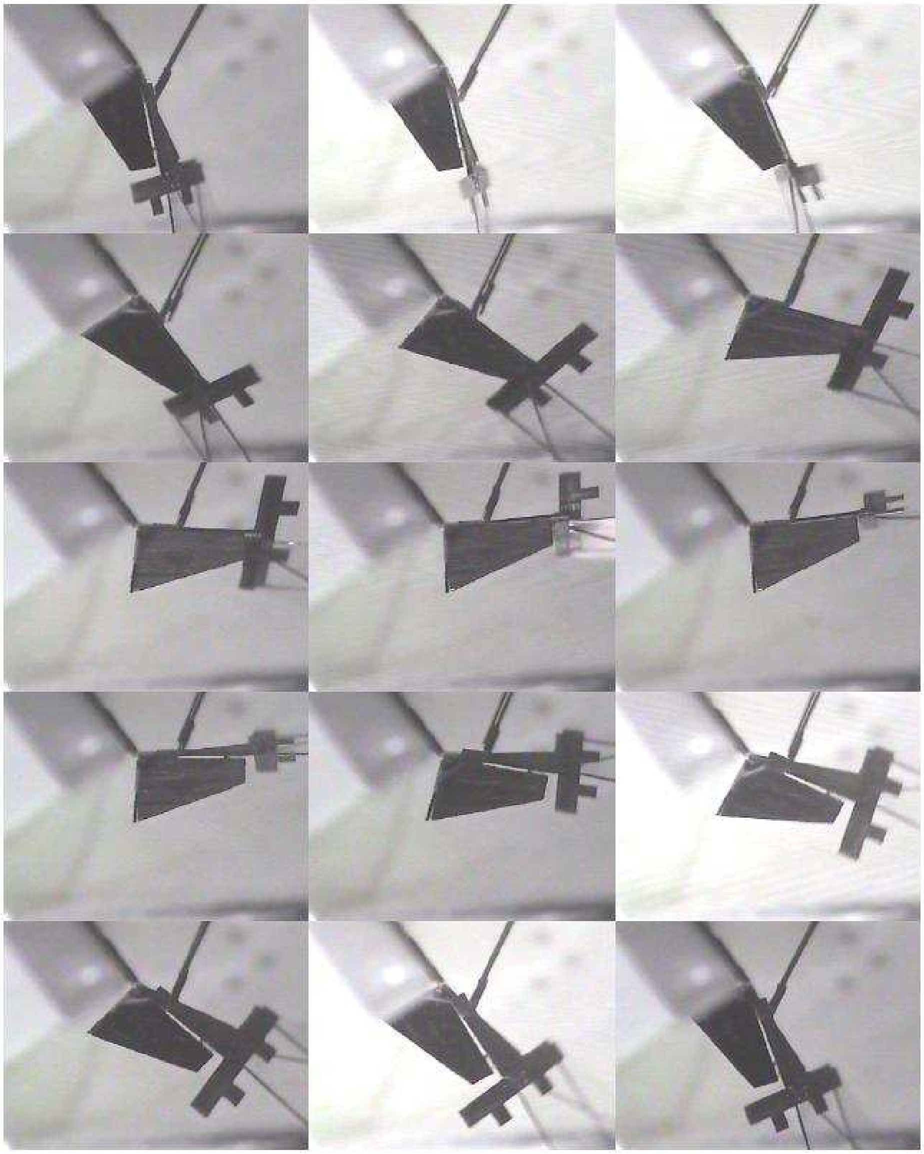

Figure 6.11: Wing trajectory of 04-κ

6.3.2 2 DOF structure 06-β

One of the most recent structures was 06-β, a single wing structure shown in Fig. 6.12. The figure shows a lift measurement setup using the AAA-250L weighing balance from Adam Equipment. The 2 DOF structure is placed on the weighing balance and the change in measured weight caused by lift is measured directly from the balance. In order to nullify the effect of the air pushed down from the wing hitting the balance and causing spurious readings, a paper "air sheild" was placed beneath the wing.

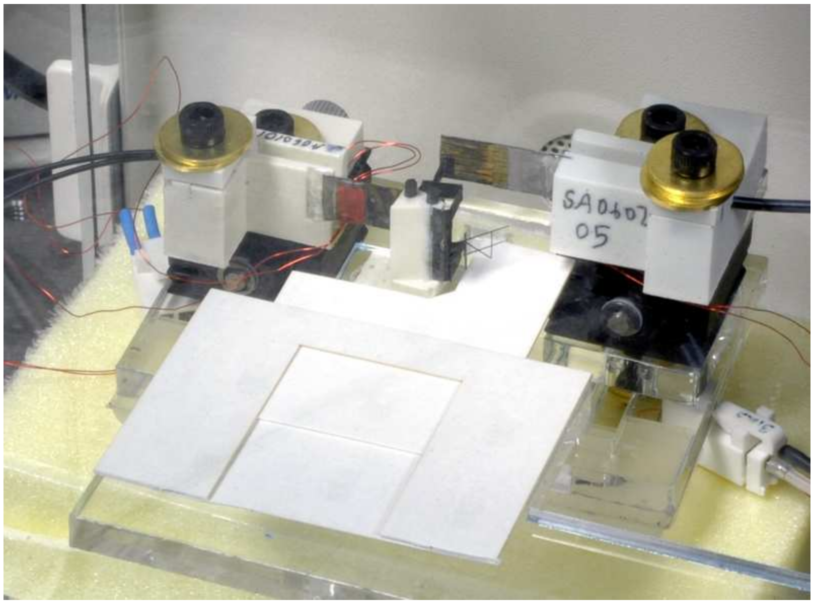

Figure 6.12: Closeup of lift measurement setup for 06-β.

A technique very similar to the one previously described for 04-κ was used on 06-β. After a "good" input trajectory was found, it was applied for 20 seconds to the structure while polling the AA-250L via RS-232 for its current weight reading. The raw measurement data taken from the balance is shown in Fig. 6.13. Note that the wing was not switched on exactly at the same time in each case which is why the point at which the weight reading begins to suddenly drop changes each time. However, the duration for which the wing was driven was kept constant at 20 seconds each time. As can be seen, we get a negative weight reading of around 1200-1600 μN for this duration, which corresponds to a positive lift measurement of the same magnitude.

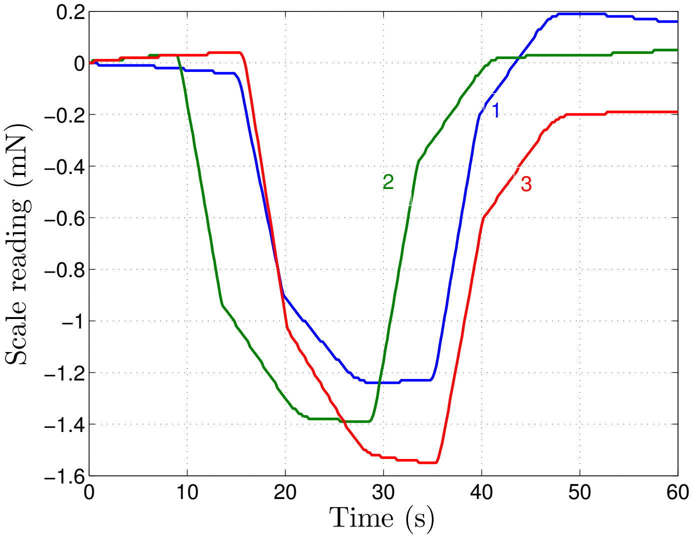

Figure 6.13: Lift measurement data for 06-β

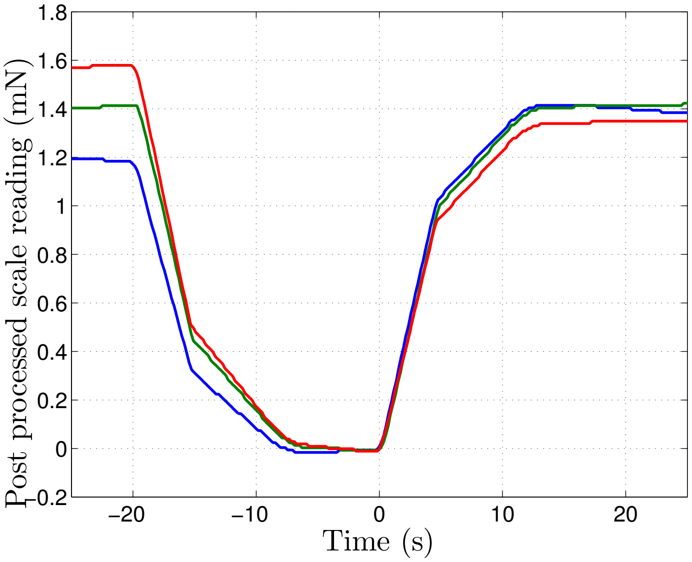

Figure 6.14: Post processed lift measurement for 06-β

It might look like there is a lot of variation in the lift produced by the wing. However, it is felt that the apparent variation might be caused more by all the wires which were going across to the structure. Although, these wires would not cause any measurable change in the steady state reading of the scale if they are completely stationary with respect to the weighing pan, slight shifts in the position of the wires can easily cause forces of the order of magnitude of the apparent variation in the lift force. Another hint that it might be the wires is is given by the fact that although the scale goes to different peak negative readings and recovers to differing peak positive readings, the difference between the peak negative readings and the final steady state value is the same. This is apparent after shifting the X and Y axis of Fig. 6.13 and is shown in Fig. 6.14.

6.4 Summary

In this chapter we described the drive scheme presently used in the MFI. We demonstrated that for the present MFI dynamics and the aerodynamic model described in [Dickinson 99], simple sinusoidal input trajectories are more than sufficient to generate good lift numbers from a wing. The efficacy of this drive scheme was demonstrated on 06-β, a 2 DOF structure which generated a measured 1400 μN of lift.

Chapter 7

Conclusions

This thesis describes the design, fabrication and control of the transmission mechanism of the Micromechanical Flying Insect (MFI). The kinematic mechanism for converting independent actuations into flapping and rotation was described in Chapter 2. A thorough dynamic analysis of the mechanical system including transmission non-linearities and the quasi steady aerodynamic model described in [Dickinson 99] was derived in Chapter 3. This dynamic analysis enabled a “dynamically tuned design” of the MFI thorax to achieve optimal symmetry and uncoupling of the nominal transfer function as described in Section 3.5. The non-linear model was explored using the Describing Function (DF) method and a systematic parameter identification was carried out as described in Section 4.4. Fabrication issues inherent in the design of flexural mechanisms were explored in Chapter 5 and several criteria for improving the performance of flexural mechanisms were derived. Finally, a simple and robust drive scheme, based on aerodynamic insight and a careful consideration of the non-linear aspects of the plant, was derived in Chapter 6.

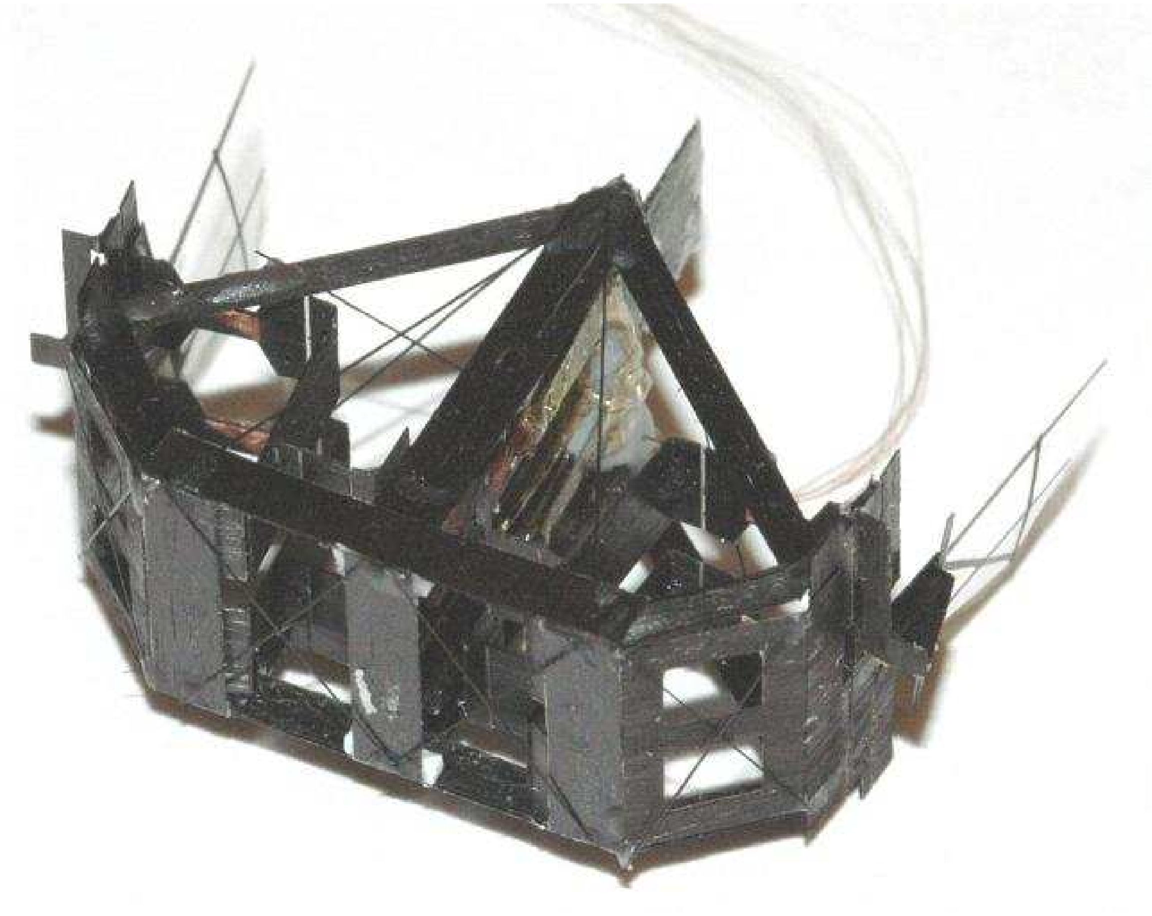

Figure 7.1: Latest airframe structure of the MFI

7.1 Future Research Directions

As was demonstrated, we have successfully realized a mechanical transmission for converting two independent actuations into a flapping and rotation capable of generating adequate lift. Since this is the first demonstrated mechanism for doing this, it is inevitable that there is room for a lot of improvement.

As briefly described in Chapter 1, the aerodynamic data derived from Robofly is not a direct fit for being used on the MFI because of the 10 times difference in

Reynolds numbers and the lack of kinematic similitude. A better understanding of the aerodynamics for trajectories and wing shapes more closely resembling the MFI wing shape and trajectories will be invaluable at further refining the dynamics. A more thorough understanding of the aerodynamics will also enable us to do a careful wing sizing to maximize the lift for a given input power. Towards this end, a custom Robofly mimicking the MFI might prove invaluable.

The transmission mechanism described here is at the target scale. Another future research direction is to create a "body" or "skeleton" around this air-frame. This problem has been addressed before in [Wood 03, Wood 04] and there are successful results already at integrating the transmission into a skeleton. Fig. 7.1 shows the latest integrated prototype of the MFI which contains at-scale fourbars, slider-cranks and actuators housed in a rigid tensegrity skeleton. Minor tweaking of this setup is required to account for some of the improvements made to the fourbar structure. Other more radical improvements could also be undertaken in designing the skeleton. For instance, the transmission could be modified to have both leading spars of the two wings be driven by a single bigger actuator. This should make it easier to tune the two wings to always be driven at resonance.

Finally, it is hoped that some of the research principles described in this work are also applicable to other mechanisms and systems. There are already some projects [Deng 05] and [Sahai 06] which utilize some of the fabrication and design methods described here to radically different robots as shown in Fig. 7.2.

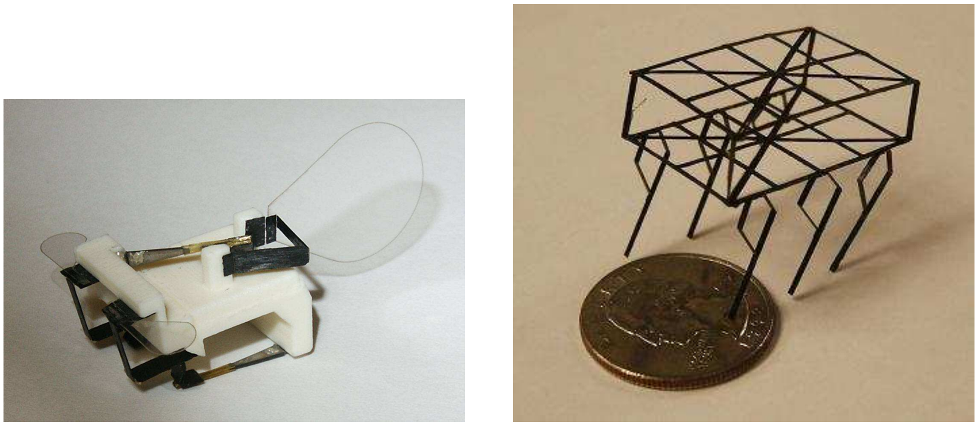

(b) Biomimetic Fishbot [Deng 05] (c) Microrobotic Crawler [Sahai 06].

Figure 7.2: Various mechanisms constructed using carbon fiber microfabrication techniques.

Bibliography

[Altshuler 05] D. L. Altshuler, W. B. Dicson, J. T. Vance, S. P. Roberts & M. H. Dickinson. *Short-amplitude high-frequency wing strokes determine the aerodynamics of honeybee flight.* Proceedings of the National Academy of Sciences, vol. 102, pages 18213–18218, 2005.

[Avadhanula 01] S. Avadhanula. The design and fabrication of a dynamically tuned MFI thorax. Master's thesis, University of California, Berkeley, December 2001.

[Avadhanula 02] S. Avadhanula, R. J. Wood, D. Campolo & R. S. Fearing. *Dynamically tuned design of the MFI thorax.* In Proc. IEEE Int. Conf. on Robotics and Automation, pages 52–9, Washington, DC, May 2002.

[Banala 05] S. K. Banala & S. K. Agrawal. *Design and Optimization of a Mechanism for Out-of-Plane Insect Winglike Motion With Twist.* Journal of Mechanical Design, vol. 127, no. 4, pages 841–844, 2005.

[Bergen 71] A. R. Bergen & R. L. Franks. *Justification of the Describing Function Method.* SIAM Journal of Control, vol. 9, no. 4, pages 568–89, November 1971.

[Birch 01] James M. Birch & Michael H. Dickinson. *Spanwise flow and the attachment of the leading-edge vortex on insect wings.* Nature, vol. 412, pages 729–733, 2001.

[Birch 03] J. M. Birch & M. H. Dickinson. *The influence of wing-wake interactions on the production of aerodynamic forces in flapping flight.* Journal of Experimental Bilogy, vol. 206, pages 2257–72, 2003.

[Birch 04] J. M. Birch, W. B. Dickson & M. H. Dickinson. *Force production and flow structure of the leading edge vortex on flapping wings at* *high and low Reynolds numbers.* Journal of Experimental Bilogy, vol. 207, pages 1063–1072, 2004.

[bla 06] *Aerovironment – Black Widow.* http://www.aerovironment.com/uav_lab_project_detail.php?id=38 (last accessed 2006.04.01), 2006.

[Buckingham 14] E. Buckingham. *On physically similar systems; illustrations of the use of dimensional equations.* Physical Review, vol. 4, pages 345–376, 1914.

[Campolo 03] D. Campolo, M. Sitti & R. S. Fearing. *Efficient Charge Recovery Method for Driving Piezoelectric Actuators in Low Power Applications.* IEEE Trans. on Ultrasonics, Ferroelectrics and Frequency Control, vol. 50, no. 3, pages 237–244, 2003.

[Carricato 01] M. Carricato, V. Parenti-Castelli & J. Duffy. *Inverse Static Analysis of a Planar System With FlexuralPivots.* Journal of Mechanical Design, vol. 123, pages 43–50, March 2001.

[Chen 02] B. Chen, X. Peng, W. Wang, J. Zhang & R. Zhang. *Research on the microstructure of insect cuticle and the strength of a biomimetic preformed hole composite.* Micron, vol. 33, pages 571–74, 2002.

[cia 06] *CIA exhibit shows off miniature spy gadgets.* url [2006] http://arstechnica.com/news.ars/post/20031029-3041.html, 2006.

[Clopeau 79] M. Clopeau, J. F. Devillers & D. Devezeaux. *Direct measurement of instantaneous lift in desert locust; comparison with Jensen's experiments on detached wings.* Journal of Experimental Bilogy, vol. 80, pages 1–15, 1979.

[Deng 05] X. Deng & S. Avadhanula. *Biomimetic Underwater Microbotic Boxfish with Oscillating Fin Propulsion: System Design and Force Measurement.* In (submitted to) Proc. IEEE Int. Conf. on Robotics and Automation, Barcelona, Spain, 2005.

[Dickinson 96] M. H. Dickinson & K. G. G otz. *The wake dynamics and flight forces of a fruit fly.* Journal of Experimental Bilogy, vol. 199, no. 9, pages 2085–2014, 1996.

[Dickinson 99] M. H. Dickinson, F-O. Lehman & S. P. Sane. *Wing rotation and aerodynamic basis of insect flight.* Science, vol. 284, pages 1954–1960, June 1999.

[did 06] *DIDEL - Microrobots and educational kits for technical schools and hobby roboticians.* http://www.didel.com/ (last accessed 2006.04.01), 2006.

[Dudley 00] R. Dudley. he biomechanics of insect flight: Form, function, evolution. Princeton University Press, 2000.

[Ellington 84a] C P Ellington. *The Aerodynamics of Hovering Insect Flight. II. Morphological Parameters.* Philosophical Transactions of the Royal Society of London. Series B, Biological Sciences, vol. 305, no. 1122, pages 17–40, 1984.

[Ellington 84b] C P Ellington. *The Aerodynamics of Hovering Insect Flight. III. Kinematics.* Philosophical Transactions of the Royal Society of London. Series B, Biological Sciences, vol. 305, no. 1122, pages 41–78, 1984.

[Ellington 84c] C P Ellington. *The Aerodynamics of Hovering Insect Flight. IV. Aerodynamic Mechanisms.* Philosophical Transactions of the Royal Society of London. Series B, Biological Sciences, vol. 305, no. 1122, pages 79–113, 1984.

[Ellington 84d] C. P. Ellington. *The Aerodynamics of Insect Flight: II. Morphological Parameters.* Philosophical Transactions of the Royal Society of London, Series B, Biological Sciences, vol. 305, no. 1122, pages 17–40, Feb 1984.

[Ellington 96] C. P. Ellington, C. van den Berg, A. P. Willmott & A. L. R. Thomas. *Leading edge vortices in insect flight.* Nature, vol. 384, pages 626–630, 1996.

[eps 06] *Epson Corporation Newsroom – Epson Develops World's Smallest Flying Microrobot.* http://www.epson.co.jp/e/newsroom/news_2003_11_18_2.htm (last accessed 2004.04.01), 2006.

[Fry 05] S. N. Fry, R. Sayaman & M. H. Dickinson. *The aerodynamics of hovering flight in Drosophila.* Journal of Experimental Bilogy, vol. 208, pages 2303–2318, 2005.

[Fung 69] Y. C. Fung. An introduction to the theory of aeroelasticity. Dover, 1969.

[Gelb 68] A. Gelb & W. E. V. Velde. Multiple input describing function methods and nonlinear system design. McGraw Hill, 1968.

[Goldfarb 99] M. Goldfarb & J. E. Speich. *A Well-behaved revolute flexure joint for compliant mechanism design*. Journal of Mechanical Design, vol. 121, no. 3, pages 424–429, September 1999.

[Howell 94] L. L. Howell & A. Midha. *A method for the Design of Compliant Mechanisms withSmall-Length Flexural Pivots*. Journal of Mechanical Design, vol. 116, pages 280–90, March 1994.

[Kang 04] B. H. Kang, J. T. Wen, N. G. Dagalakis & J. J. Gorman. *Analysis and Design of Parallel Mechanisms with Flexure Joints*. In Proc. IEEE Int. Conf. on Robotics and Automation, pages 4097–102, New Orleans, LA, April 2004.

[Kota 99] S. Kota. *Design of Compliant Mechanisms, Application to MEMS*. In SPIE Conference on Smart Electronics and MEMS, Newport Beach, CA, Mar 1999.

[Madangopal 05] R. Madangopal, Z. A. Khan & S. K. Agrawal. *Biologically Inspired Design Of Small Flapping Wing Air Vehicles Using Four-Bar Mechanisms And Quasi-steady Aerodynamics*. Journal of Mechanical Design, vol. 127, no. 4, pages 809–816, 2005.

[Magnan 34] A. Magnan. La locomotion chez les animaux. Hermann, Paris, 1934.

[mes 06] *The Mesicopter: A Meso-scale Flight Vechicle*. http://aero.stanford.edu/mesicopter/ (last accessed 2006.04.01), 2006.

[Murray 93] R. M. Murray, Z. Li & S. S. Sastry. A mathematical introduction to robotic manipulation. CRC Press, 1993.

[Nicoud 02] J.D. Nicoud & J.C. Zufferey. *Toward Indoor Flying Robots*. In Proceedings of the IEEE/RSJ International Conference on Intelligent Robots and Systems, pages 787–792, 2002.

[pix 06] *Pixelito*. http://pixelito.reference.be/ (last accessed 2006.04.01), 2006.

[Pornsin-Sirirak 00] T. N. Pornsin-Sirirak, S. W. Lee, H. Nassef, J. Grasmeyer, Y. C. Tai, C. M. Ho & M. Keennon. *MEMS wing technology for a battery powered ornithopter*. In IEEE 13th Annual International Conference on MEMS, 2000.

[Pornsin-Sirirak 01] T. N. Pornsin-Sirirak, Y. C. Tai, H. Nassef & C. M. Ho. *Titanium-alloy MEMS wing technology for a micro aerial vehicle*. Applications, Sensors and Actuators, A: Physical, vol. 89, no. 1-2, pages 95–103, March 2001.

[Press 99] W.H. Press, S.A. Teukolsky, W. T. Vetterling & B.P. Flannery. Numerical recipes in c, the art of scientific computing. Cambridge University Press, 1999.

[Releaux 76] F. Releaux. The kinematics of machinery: Outlines of a theory of machines. McMillan and Company, 1876.

[Sahai 03] R. Sahai, J. Lee & R. S. Fearing. *Semi-Automated Micro Assembly for Rapid Prototyping of a OneDOF Surgical Wrist*. In IEE Conf. on Intelligent Robots and Systems, Las Vegas, NV, Oct 2003.

[Sahai 05] R. Sahai, E. Steltz & R. S. Fearing. *Carbon Fiber Components with Integrated Wiring for Millirobot Prototyping*. In (submitted to) Proc. IEEE Int. Conf. on Robotics and Automation, Barcelona, Spain, April 2005.

[Sahai 06] R. Sahai, E. Steltz, S. Avadhanula & R. S. Fearing. *Towards a carbon fiber crawling robot*. In (submitted to) Proc. IEEE Int. Conf. on Robotics and Automation, 2006.

[Sanders 93] S. R. Sanders. *On limit cycles and the describing function method in periodically switched circuits*. IEEE Transactions on Circuits and Systems I: Fundamental Theory and Applications, vol. 9, no. 40, pages 564–72, 1993.

[Sane 02] S. P. Sane & M. H. Dickinson. *The aerodynaic effects of wing rotation and a revised quasi-steady model of flapping flight*. Journal of Experimental Biology, vol. 205, pages 1087–96, 2002.

[Sane 03] S. P. Sane. *The aerodynamics of insect flight*. The Journal of Experimental Biology, vol. 206, pages 4191–4208, 2003.

[Schenato 01] L. Schenato, X. Deng & S. Sastry. *Virtual insect flight simulator (VIFS)*. In Proc. IEEE Int. Conf. on Robotics and Automation, Seoul, Korea, May 2001.

[Schenato 03] L. Schenato. *Analysis and Control of Flapping Flight: from Biological to Robotic Insects*. PhD thesis, University of California, Berkeley, 2003.

[Shimada 00] E. Shimada, J. A. Thompson, J. Yan, R. J. Wood & R. S. Fearing. *Prototyping millirobots using dextrous microassembly and folding.* In Symp. on Microrobots ASME Int. Mech. Eng. Cong and Expo., Orlando, FL, November 2000.

[Shimoyama 93] I. Shimoyama, H. Miura, K. Suzuki & Y. Ezura. *Insect like microrobots with external skeletons.* In ICRA, February 1993.

[Steltz 05] E. Steltz, S. Avadhanula, R.J. Wood, & R.S. Fearing. *Characterization of the Micromechanical Flying Insect by Optical Position Sensing.* In Proc. IEEE Int. Conf. on Robotics and Automation, April 2005.

[Steltz 06] E. Steltz, M. Seeman, S. Avadhanula & R. S. Fearing. *Determination of Power Electronics Technology with Respect to the Design of Piezoelectric Microrobots.* In (submitted to) IEE Conf. on Intelligent Robots and Systems, 2006.

[Wang 04] Z. J. Wang, J. M. Birch & M.l H. Dickinson. *Unsteady forces and flows in low Reynolds number hovering flight: two-dimensional computations vs robotic wing experiments.* Journal of Experimental Bilogy, vol. 207, pages 449–460, 2004.

[Wood 03] R. J. Wood, S. Avadhanula & R. S. Fearing. *Microrobotics using composite materials.* In Proc. IEEE Int. Conf. on Robotics and Automation, Taipei, Taiwan, May 2003.

[Wood 04] R. J. Wood. *Composite Microstructures, Microactuators and Sensors for Biologically Inspired Micro Air Vehicles.* PhD thesis, University of California, Berkeley, 2004.

[Wood 05] R.J. Wood, S. Avadhanula, E. Steltz, M. Seeman, J. Entwistle, A. Bachrach, G. Barrows, S. Sanders & R.S. Fearing. *Design, Fabrication and Initial Results of a 2g Autonomous Glider.* In 31st Annual Conference, IEEE Industrial Electronics Society 2005 Meeting, 2005.

[Wu 03] W.C. Wu, L. Schenato, R.J. Wood & R.S. Fearing. *Biomimetic Sensor Suite for Flight Control of a Micromechanical Flight Insect:Design and Experimental Results.* In Proc. IEEE Int. Conf. on Robotics and Automation, 2003.

[Yan 02] J. Yan. *Fabrication and Wing Force Control for a Micromechanical Flying Insect.* PhD thesis, University of California, Berkeley, 2002.

[Yeh 94] R. Yeh, E. Kruglick & K. S. J Pister. *Towards an articulated silicon microrobot.* Proceedings of ASME Winter Annual Meeting, Dynamic Systems and Control, vol. 2, 1994.

[Yi 03] B. Yi, G. B. Chung, H. Y.Na & W. K. Kim. *Design and Experiment of a 3-DOF Parallel MicromechanismUtilizing Flexure Hinges.* IEEE Transactions on Robotics and Automation, vol. 19, no. 4, pages 604–12, Aug 2003.

Appendix A

G-Code utilities

The first step in any of the fabrication steps detailed so far is to lay out a 2-D design in a CAD program such as Solidworks. In order to cut a 2-D layout on the New-Wave laser machine, the 2-D layout needs to be converted into a format understandable by `microlaze`, the program which controls the New-Wave laser. This format is a slightly modified version of the standard CNC control language called `GCODE`.

This appendix describes a set of MATLAB utility functions which were created with the aim of making it easier to convert `DXF` files which are produced by Solidworks into `GCODE`. Before going into a description of the utilities, a brief description of the modified `GCODE` format is given.

A.1 `GCODE` format

A `GCODE` file consists of a sequence of lines each of which can be one of the following formats. Note that all dimensions are assumed to be in mm.

`G01 X<xc> Y<yc>` This tells the laser machine to cut from the current location to the location `(<xc>, <yc>)`.

`X<xc> Y<yc>` This is equivalent to `G01 X<xc> Y<yc>`.

`G00 X<xc> Y<yc>` This tells the laser machine to move to `(<xc>, <yc>)` without turning on the laser.

`G02 I<cx> J<cy> X<xc> Y<yc>` This tells the laser machine to cut a clockwise arc from the current location to the coordinates given about the center `(<cx>, <cy>)`.

`G03 I<cx> J<cy> X<xc> Y<yc>` This is identical to the `G02` command except that the arc is cut in an anticlockwise direction.

`MMC markersize X<xp> Y<yp>` This instructs the laser machine to change its aperture to `<xp>`% in the X direction and `<yp>`% in the Y direction.

`MMC focusoffset X<xo> Y<yo>` This instructs the laser machine to move off by `(<xo>, <yo>)` when it tries to refocus.

`MMC cutstepsize D<sz>` This instructs the laser machine to travel by `<sz>` to get to the next cut location.

`MMC pulserate R<rate>` This instructs the laser to change its laser pulse rate to `<rate>` Hz.

The `MMC` commands are specific to `microlaze`.

A.2 PREPGC: Creating G-Code files

`prepgc` is used for creating GCode files for laser micromachining. It is meant to be used to convert `.DXF` files created in a 2-D layout software such as Solidworks into 2-D G-Code files which can be fed into `microlaze`.

Usage

The simplest way of calling prepgc is without options in which case we simply call it with the list of file names as

```
>> prepgc file_1  file_2 ... file_N
```

You can either provide a single file name or you can provide 3 or more filenames. Providing exactly two file names is an error. You can either specify the exact file name or if its a `DXF` file, skip the extension.

If provided with a single file name, prepgc simply reads in the cuts in that file, does some post processing on them as described in **Post Processing** below and writes out the processed cuts in a new file whos file name is the original file name appended with `'.go'`.

If more than 2 files are supplied, then prepgc does the following:

1. Read in the contents of `file_1` through `file_(N-1)`. Call the lines therein `lines_1` ... `lines_(N-1)`.

2. Create `lines_N` by "subtracting" `lines_2` through `lines_(N-1)` from `lines_1`. In otherwords,

   ```
   >> lines_N = lines_1 - (lines_2 + ... + lines_(N-1))
   ```

See ”SubtractLines” for an explanation of what ”subtraction” means.

3. Process `lines_2` through `lines_N` as described in **Post Processing** below. Write these lines in new files of the form `file_2.go`, `file_3.go` etc.

Post Processing

`prepgc` performs the following post-processing on each file: (These actions can be optionally disabled based on the optional arguments supplied).

Optimize the order of cuts The order of the cuts within each file is optimized in a ”nearest-next” manner in order to minimize the traversal time.

Calculate the direction of auto-focussing for each line The direction in which to move while auto-focussing is adjusted for each line to minimize the probability of trying to focus on an already cut region.

Shift the bounding box The lines are shifted together so that the bounding box of the lines lies at (0,0). This makes the initial positioning of the shim easier.

Remove duplicate lines Duplicate lines are removed from the file to avoid the laser cutting over the same region.

Tweaking the behavior

If you wish to tweak the behavior of `prepgc`, you can supply optional arguments. These are supplied after all the file names followed by two dashes. Thus you can do

```
>> prepgc file1 file2 ... fileN -- option1 value1 ...
```

or

```
>> prepgc('file1', 'file2', ..., 'fileN', ...
        '--', 'option1', 'value1', ...);
```

Both ways of calling prepgc are equivalent as long as all the options have string values. If you need to supply numeric option values, then you need to use the second form of invoking prepgc.

The following optional arguments are recognized.

'shift' (Default value: `[0, 0]'`) whether or not to shift the original bounding box. This optional argument is specified as either a 0, 2 or 3 element vector.

- When specified to be an empty vector, the bounding box is not shifted at all.
- When specified as a 2 element vector, the bounding box of the resulting files are shifted *to* the specified coordinate, i.e, the lower left corner of the resulting file(s) will be at the specified coordinate.
- When specified as a 3 element vector, the bounding box is shifted *relative* to the original location by the amount specified. The relative displacement is specified by the first two elements of the 3 element vector. The third element is ignored.

This argument can also be specified as a string, either `'yes'` or `'no'`. Specifying `'yes'` is equivalent to specifying `[0, 0]'`, and specifying `'no'` is equivalent to specifying `[]`.

’optimize’ (Default value: `’yes’`) whether or not to optimize the cut order to minimize the traversal time.

’remdup’ (Default value: `’no’`) whether or not to remove duplicate lines. See `RemoveDuplicateLines.m` for what this means. This is a *lengthy* operation (grows quadratically with the number of lines). If you are reasonably sure that you have not created duplicates in your solidworks file, leave this out.

’autofocus’ (Default value: `’yes’`) whether or not to find the focus offsets for each line.

’insertwp’ (Default value: `’yes’`) whether to automatically insert way points to avoid traversing over already cut regions.

’config’ (Default value: `’’`) The default Microlaze configuration file to use. When reading a .go file or a `DXF` file which does not contain any embedded microlaze configuration information, then `prepgc` uses the configuration specified in this file. The embedded information in `.go` files will over-ride the configuration information provided in the config file.

’mmc’ (Default value: `’yes’`) Whether or not to embed microlaze commands within the generated GCode file. By default, `prepgc` embeds microlaze configuration commands within the GCode file which allow microlaze behavior to change on a per-line basis. These lines will cause traditional CNC machines to err. Setting `’mmc’` to `’no’` will generate a *clean* GCode file.

’showgui’ (Default value: `’yes’`) Whether to show the resulting post-processed files by bringing up the GCode editor.

'layer' (Default value: `''`) If a non-empty string is specified for the layer option, only those entities belonging to that layer are extracted. This is useful for drawings which contain multiple layers.

'outfile' (Default value: `''`) This option is used only when a single file is being specifed. If while processing a single file say `<file.DXF>`, this option is *not* specified, then prepgc automatically writes out the processed lines into a file called `<file.go>`. If a non-empty string is specified, then prepgc writes out to the specified file.

A.3 GCEDIT: Editing G-Code files

`gcedit` is a graphical front-end for editing features in G-code files created by `prepgc`.

Usage

```
>> gcedit file1 file2 ...
```

The filenames can either be complete file names of `.go` or `.DXF` files. If an extension has not been specified for the file name, then gcedit will attempt to see if there is a .DXF file of the same name and open that instead.

When `gcedit` is invoked, it opens up the GUI frontend as shown in Fig. A.1. This GUI shows all the lines found in the various files in the central view axis. Each group of lines which shares a common configuration are shown in a single color.

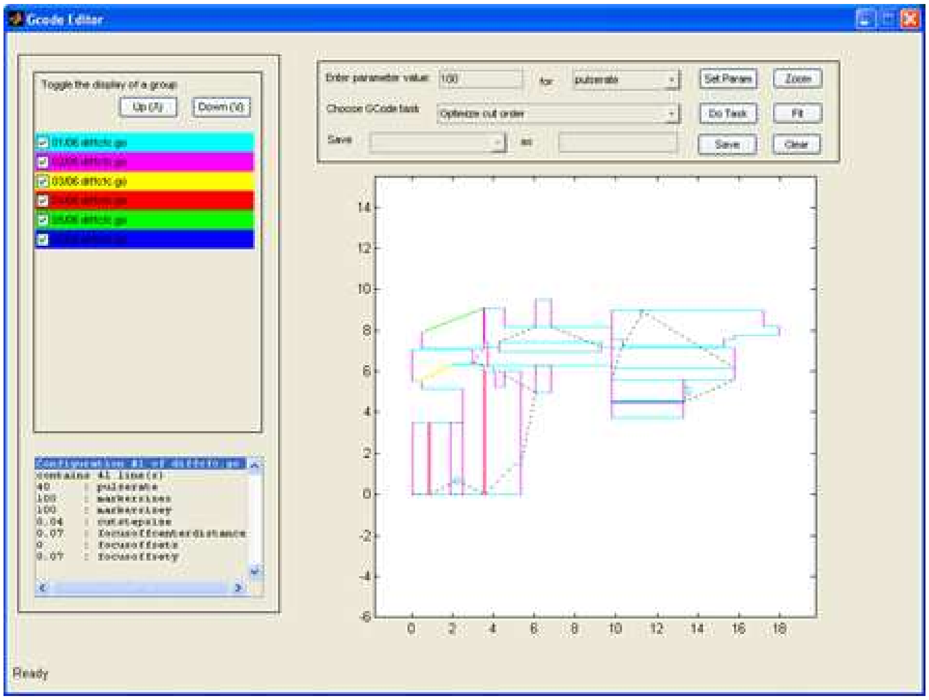

Enter parameter value: 100 for pulserate

Choose GCode task: Optimize cut order

```
contains 41 line(s)
40     : pulserate
100    : markersizex
100    : markersizey
0.04   : cutstepsize
0.07   : focusoffcenterdistance
0      : focusoffsetx
0.07   : focusoffsety
```

Figure A.1: GUI frontend of `gcedit`

With this GUI frontend you can do the following

Toggle visibility of groups You can view/hide all lines which share the same configuration by ticking/unticking the checkbox next to the group name.

Select a set of lines Clicking on a line toggles the selection of that line. You can also drag a rectangle and select all lines which lie completely within the rectangle. Note that selecting by dragging a rectangle is enabled when the `Select` button is showing. If you see `Zoom`, then dragging a rectangle will zoom into that rectangle. Hitting the `Clear` button will clear all lines from the selection.

Changing configuration parameters Once one or more lines are selected, you can change their `microlaze` configuration parameters by entering a parameter value in the edit box, choosing which parameter you wish to change in the drop down menu and then hitting the `Set Param` button.

Overall manipulation You can also do manipulations on the G-code file such as deleting lines, changing the order in which certain lines are cut, inserting way points in the middle of two cut lines etc. All these tasks are done by selecting the desired task from the drop down menu and then hitting the `Do Task` button.

A.4 COMBINEGCODE: Combining G-Code files

`combinegcode` is used to combine G-code files into a single job so that multiple copies of jobs can be cut at the same time.

Usage

Type `edit CombineGCode` on the matlab prompt and then edit the cell array `combineinfo` to run the program.

The i^{th} element of `combineinfo` is itself a cell array consisting of 3 elements:

`[x,y]` offset to move the corresponding job (x and y are added to every coordinate specified in the corresponding job).

`cutfilename` File name of the G-code file containing the cuts. Leave blank (`[]` or `''`) if there is no cut file. The `cutfilename` needs to be specified relative to MATLAB's current working directory.

`scorefilename` Filename of the G-code file containing the scores. Leave blank (`[]` or `''`) if there is no score file.

Example

```
combineinfo = {
    {[0, 0], 'cut1.go', 'score1.go' },
    {[10,0], 'cut2.go', 'score2.go'}
};
outputFileNames = {'totalcut.go', 'totalscore.go'}
```

combines lines from the jobs 1 and 2, by shifting job 2 by 10 mm along the X axis and then appending it to job 1. Note that the original files are left intact. i.e `cut2.go` and `score2.go` are not changed.

Appendix B

xPC utilities

B.1 RUN2DOF: drive a 2 DOF structure with arbitrary wave-forms

This function can be used to provide arbitrary sine/smoothed square wave inputs to the two actuators. There are three modes of operation for this function.

1. In the first mode, the function runs the structure for 2 seconds and returns a data structure containing measurements of the A/D readings in this time and the drive specifications. This is the default behavior.
2. In the second mode, the function begins driving the structure and waits for user input to interrupt it again. This is useful if you are driving something for long periods of time. To do this, specify the optional argument `'measure'` as 0 and `'timedCapture'` as 0.
3. In the third mode, the function runs the structure for a specified period of

time and simultaneously records video from the WinNov Videum video capture card. It then prompts the user to save the video and also saves a data structure which specifies the drive specifications. To do this, specify `'measure'` as 0 and `'timedCapture'` to some positive value.

Usage

```
>> [expdata] = run2dof(input, ...)
```

`input` is a mandatory input argument which specifies the drive parameters for the two inputs of a 2 DOF structure. A utility function `formGenSigStruct` is provided to enable the user to create this structure with the required fields, all values of which are initialized to zero. The user is then expected to give the actual values to each of the fields.

```
>> input = formGenSigStruct;
>> input.DC1 = 1;
>> ... etc ...
```

The fields in this data structure are meant to be:

`DC1, DC2` DC input applied to the 2 actuators. This is the value produced by the D/A port of the Q8 port. If you are feeding this through an amplifier etc., then the plant will be driven by this value times the amplifier gain.

`A11, A12` Drive amplitudes applied to the first actuator at ω and 3ω.

`A21, A22` Drive amplitudes applied to the second actuator at ω and 3ω.

`g11, g12, g21, g22` Phases of the inputs at the two frequencies (same notation as `Aij`).

`w` frequency of motion (rads/s).

Note that `g11` etc. need to specified in radians, but `DC*`, `A*` need to be specified in volts after including scaling factors for amplifiers/fourbar DC motions etc.

This way of specifying the motion is the most general with the restriction that the frequency content is restricted to DC, ω and 3ω.

NOTE: The input argument can also be another data structure of the form returned by square2gen.

```
>> help square2gen
```

for more information on specifying the input this way.

Optional Input arguments

For these options, the default values are specified in square brackets just after the name of the option. These optional arguments are specified in the following manner:

```
>> run2dof(indata, 'measure', 0, 'timedCapture', 20)
```

`'measure'` [1]

A boolean value either 1 or 0. If set to 1, then the function operates in the *measurement mode*, where the system runs for 3 seconds and measures the motion during this time. In this mode, the function returns a data structure with the following fields:

`indata` the input specification given to this function. You should be able to recover the experimental conditions from this structure.

`vin1` the voltage input to the first actuator `vin2` the voltage input to the second actuator

`vout1` the voltage output from the first sensor

`vout2` the voltage output from the second sensor

`time` the time signal corresponding to the measurements

When measure is 0, then the system operates in ”non measurement mode” and no output arguments are returned.

`’measurementTime’` [1]

In measurement mode, the number of seconds for which to capture data. Note that in measurement mode, there are initial and final ramps of 1 seconds each. This time is for the middle part.

`’timedCapture’` [0]

If set to a positive value, then MATLAB automatically invokes WINNOV Videum capture and records the video stream for however many seconds are specified by the timedCapture value.

NOTE: This optional argument does nothing when a value of 1 is specified for `’measure’`, i.e in measurement mode.

`’silent’` [0]

When set to 1, then the program does not display the input waveform and ask for confirmation. It directly proceeds to feed the input waveforms into the device.

`’calibFile’` [”]

A file name or structure which contains the output from a run of CalibSensor2DOFPause.

`'numdof'` [2]

Whether we are running a single or a two DOF system. Specify either 1 or 2.

Output

B.2 CALIBSENSOR: Calibrate sensors optically

This function is meant to aid in calibrating a displacement sensor by optically matching the measured sensor reading with visually measured displacement. This function is capable of measuring either angular displacements or linear displacements. Note that if it is measuring linear displacement, the edge which is being measured needs to be a horizontal edge which moves in the vertical direction.

Usage

```
>> cdata = calibSensor2DOFPause(vin, ...)
```

The mandatory input argument `vin` is a vector of nominal drive voltages to be applied to the two actuators. For best results speficy a vector of values which increases and then decreases again to 0V. For example, something like

```
[0.75 1.5 2.25 3.0 2.25 1.5 0.75 0]
```

Once started, the function performs the following steps:

1. It opens up two MATLAB figures. The first is an ActiveX control showing live video being captured by the WINNOV Videum capture card. The second figure will show captured frames in which the user is asked to draw rectangles around the measured eges.
2. It first measures the two sensor readings without any input actuation to the structure. A measurement is done by averaging the sensor reading for 0.1 seconds, sampled at 20KHz.
3. The script then commands the WINNOV driver to capture a frame and displays the captured frame in the second figure. It asks the user to draw a rectangle around the edge which corresponds to the body whose displacement is being measured by the sensors.
4. Once the user draws a rectangle around the measured edge, the function performs edge detection in the chosen portion and extracts an edge.
5. It then ramps up the voltages to the two inputs at 1V/s till both inputs attain the first value specified by the input parameter `vin`. If this is a 2 DOF structure, the function asks the user to hit the `j` and `k` keys to adjust the voltage supplied by the D/A port 5 of the Q8 board. This is typically connected to the second input port of the system being calibrated. Once the voltage adjustment is done, the user adjusts presses `<enter>`. This tells the function that the adjustment is done.
6. The function then reads in the sensor reading by averaging over 0.1 seconds at 20KHz.

7. It captures the frame currently displayed in the first figure and once again asks the user to draw a rectangle around the edge to be measured.
8. It repeats this procedure till all the specified input voltages are applied.

Optional input arguments

For these options, the default values are specified in square brackets just after the name of the option. These optional arguments are specified in the following manner:

```
>> cdata = calibSensor2DOFPause([1,2], 'detect', 'edge');
```

`'detect'` [`'angle'`]

By default `calibSensor2DOFPause` will measure the change in angle of the detected line. This is useful for calibrating angular outputs. For calibrating linear outputs such as actuator motion, specify this to be `'edge'`.

`'displ'` []

This option, if non-empty is assumed to be the values of the displacement at the given voltage signals. In this case, `calibSensor2DOFPause` will not invoke WINNOV to capture pictures. It will only measure the sensor signal. The length of this vector needs to be same as the length of the mandatory `vin` argument.

Output

The output is a structure which has the following fields:

`time` This is just an array going from 1 to the number of input points at which the measurement was taken.

`Vin` The vector of input voltages applied.

`Vout` The vector of measured output voltages. Note that the output voltage is measured by averaging the sensor output for 1 second.

`disp` The displacement which was measured by processing the images.

`images` An array of images taken for each of the specified input voltage (and also at 0 voltage).

Experimental Setup

The following experimental setup needs to be created in order to use this function (This is already setup in 319 Cory hall).

1. First set up the camera above the displacement source which is being measured. The camera needs to be focussed on a good clean edge which it will measure the displacement of.
2. The video feed from the camera needs to be fed into the computer running this function via the WINNOV Videum Video capture board. This function only understands how to control this particular video capture card.
3. Connect D/A ports 1 and 5 of the Quanser Q8 board to the two inputs of the system which will drive the displacement. Connect the output from the displacement sensors into A/D ports 1 and 5 of the Quanser Q8 board. Note

that port 5 of the Q8 board is connected to the second BNC plug of the pin-out board.

Recipe for calibrating 2 DOF fourbar structure

The following recipe is meant to be used to calibrate the sensor output to wing hinge motion of a 2 DOF fourbar structure with an attached differential. Since the bottom spar of a 2 DOF structure cannot typically be seen because it is completely obstructed by the differential, this script allows the user to adjust the voltages on the two actuators

B.3 MFIDSA: Experimental frequency response measurement

This tool was developed to measure frequency responses of two input two output systems. The tool consists of two Simulink models which gets compiled to run on the xPC target machine a GUI frontend to control and communicate with the xPC target.

Usage

Simply type:

```
>> mfidsa
```

This opens up the GUI frontend. After specifying all the drive parameters, press the “Go” button. The tool generates sinusoids of increasing frequency at the D/A ports

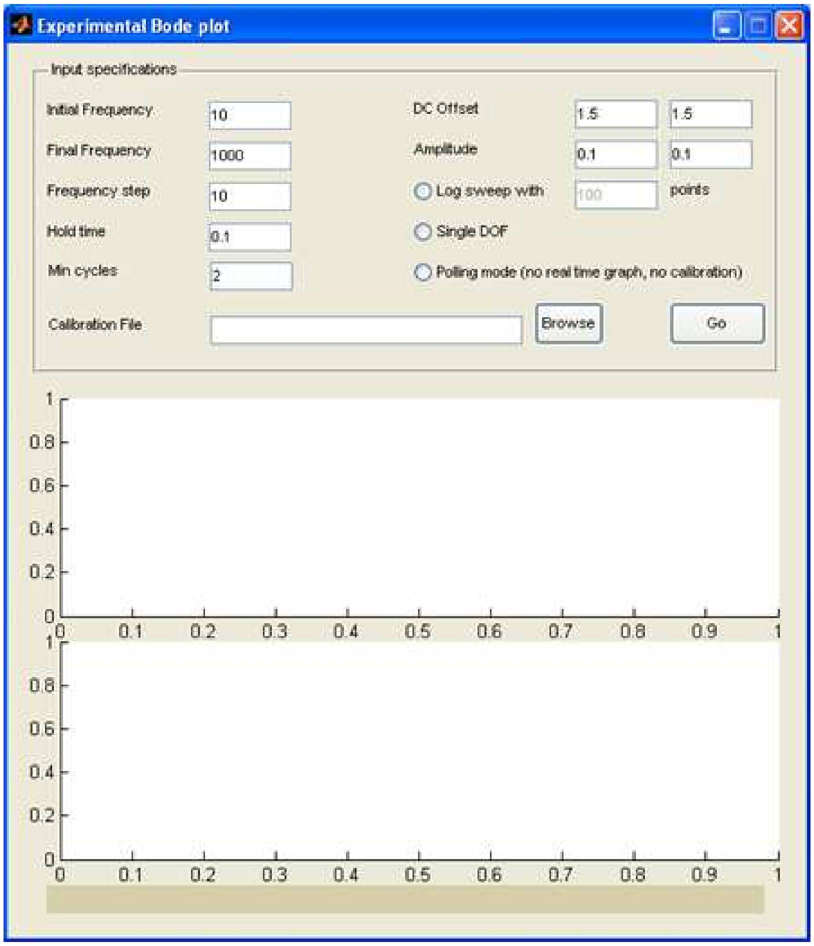

Experimental Bode plot

Input specifications

Initial Frequency: 10

Final Frequency: 1000

Frequency step: 10

Hold time: 0.1

Min cycles: 2

DC Offset: 1.5 | 1.5

Amplitude: 0.1 | 0.1

○ Log sweep with 100 points

○ Single DOF

○ Polling mode (no real time graph, no calibration)

Calibration File

Figure B.1: GUI frontend for experimental frequency response Measurement

of the Q8 board and does a real time fourier transform of the measured A/D signals. After the sweep is finished, a structure named `plantTFData` is created in MATLAB's base workspace which describes the drive conditions and also contains the recorded frequency response data.

The GUI allows you to set the following parameters of the frequency response experiment:

Frequency specification The frequency points at which the frequency response will be measured can be specified as either a linear scale by specifying the intial measurement frequency, the frequency step size and the final measurement frequency. In this case the frequency range becomes

```
>> freq_range = [init_freq:step_freq:final_freq];
```

Alternatively, by selecting the "Log Sweep" radio button, the frequency range can be specified on a logarithmic scale by specifying the number of points between the initial and final frequency points. In this case, the frequency range becomes

```
>> freq_range = logspace(log10(init_freq), ...
...                      log10(final_freq), ...
...                      npoints)
```

Voltage specification The voltage generated by this function is available on D/A ports 1 and 5 of the Q8 board. You can specify the DC levels and the amplitudes of the voltage signals. If you need to drive bimorphs, then the bias voltage has to be applied by some other external means.

Calibration file You can also use calibration data obtained using `calibsensor` so that the frequency response is in the units which are of interest instead of as sensor volts.

Measurement mode Whether to use the polling mode Simulink model or the interrupt driven Simulink model. The polling mode model runs at 80KHz and therefore is suitable for frequency ranges upto 40KHz, whereas the interrupt driven model runs at 20KHz and therefore can only be used upto 10KHz. Note that in polling mode, there will be no real time update of the frequency response